MODERN APPLIED SCIENCE

CCSE

Canadian Center of Science and Education

Editorial Board

Contents

Some Sufficient Conditions for Oscillation of Symmetric Cellular Neural Networks with Delay

Sarhan M. Musa

College of Engineering, Prairie View A&M University

Prairie View, TX 77447, USA

Tel: 936-261-9860   E-mail: smmusa@pvamu.edu

Abstract

In this paper, some sufficient conditions for oscillation of symmetric cellular neural networks with delay (DCNNs) are introduced. These conditions impose constrains on the system of dynamic state equations when the cells are working in linear region $\dot{x}(t) - Hx(t) - A_1 x(t - \tau) = 0$, where the coefficients H and A_1 are real 2×2 matrix $\mathbf{R}^{2 \times 2}$, $\tau \in \mathbf{R}^+$, and $x(t), \dot{x}(t) \in \mathbf{R}^{2 \times 1}$ are the state vector and its derivative at time t.

Keywords: Cellular neural networks with delay (DCNNs), Oscillation

1. Introduction

Cellular neural networks (CNNs) were introduced by (Chua, L O et al, 1988, p. 1257-1272; Chua, L O et al, 1988, 1273-1290); they found important applications in pattern recognition and signal processing, especially in statistic image treatment. The stability of CCNs has been investigated in (Chua, L O et al, 1990, p. 1520-1527; Zou, F et al, 1991, p. 38:675-677; Savaci, F A et al, 1992, p. 240 – 245).   Processing of moving images requires the introduction of a delay in the signal transmitted among the cells, which led to introducing delayed cellular neural networks (DCNNs) by (Chua, L O et al, 1990, p. 12-25; Chua, L O, 1992, p. 449-459) and the consideration of their dynamic behavior in (Roska, T et al, 1992, p. 487-490). The most important uses of DCNNs (signal and image processing, non-linear/transcendental equation solving and so on) rely on stability. The stability of DCCNs has been investigated in many papers (Liao, T L et al, 1999, p. 1347-1349; Arik, S et al, 2000, p. 571-574; Liao, T L et al; 2000, p. 1481-1484; Takahshi, N N, 2000, p. 793-799; Arik, S, 2002, p. 1211-1214; Arik, S, 2003, p. 156-160). However, this work presents some sufficient conditions for oscillation of symmetric cellular neural networks with delay (DCNNs) for the dynamic state equations.

2. Cellular neural networks with delay

A CNN is a massively parallel computing architecture made of simple processing elements (cells) which are locally connected. A cell is the basic circuit unit containing linear and nonlinear circuit elements, which are linear resistors, linear capacitors, linear and nonlinear controlled sources and independent sources. Any cell in a CNN is connected only to its neighbor cells. Due to the propagations effects on continuous time dynamics of CCNs, the cells that not directly connected to each other can affect each other indirectly (Chua, L O et al, 1988, p. 985- 988). These properties of the CCNs are similar to the cellular automata.

In this paper we refer to Civalleri and Gilli study on some stability properties of DCNNs with consideration to reciprocal and non-reciprocal of the networks. They showed that a symmetric DCNN can become unstable if the delay is suitably chosen and they present a sufficient condition to assure the complete stability (Civalleri, P P et al, 1992, p. 94 -99; Civalleri, P P, 1993, p. 157-165). This paper gives new sufficient conditions for oscillation of symmetric cellular neural networks with a delay τ. These conditions impose constrain on the system of dynamic state equations, $x(t)$, when the cells are working in linear region.

Now, suppose the cells of the DCNNs are working in linear region, i.e.: (in matrix notation)

$$\dot{x}(t) - Hx(t) - A_1 x(t - \tau) = 0, \tag{1}$$

for a symmetric DCNN with a delay τ, which can oscillate, where

$$x(t) = \begin{pmatrix} x_1(t) \\ x_2(t) \end{pmatrix} \quad , \quad H = \begin{pmatrix} h & a_{12}^0 \\ a_{12}^0 & h \end{pmatrix} \quad , \quad A_1 = \begin{pmatrix} a_{11}^1 & a_{12}^1 \\ a_{12}^1 & a_{11}^1 \end{pmatrix}, \text{ and } h = a_{11}^0 - 1 > 0 ,$$

where H and A_1 are coefficients of real 2×2 matrix $\mathbf{R}^{2 \times 2}$, τ is non-negative real number.

The dynamic equations of a (2×1)-DCNN (cells are arranged in 2rows and 1 column) for equation (1) are the following systems of equations:

$$\frac{dx_1(t)}{dt} = -x_1(t) + a_{11}^0 x_1(t) + a_{12}^0 x_2(t) + a_{11}^1 x_1(t-\tau) + a_{12}^1 x_2(t-\tau) ,$$

$$\frac{dx_2(t)}{dt} = -x_2(t) + a_{12}^0 x_1(t) + a_{11}^0 x_2(t) + a_{12}^1 x_1(t-\tau) + a_{11}^1 x_2(t-\tau) .$$

In this paper we will use two definitions for the systems of the differential equations $x_1(t)$ and $x_2(t)$ to define the theory of oscillation of solutions.

Definition 1: A solution $x(t) = \left[x_1(t), x_2(t), \ldots\ldots, x_m(t) \right]^T$ is said to oscillate if every component $x_j(t)$ of then solution has arbitrary large zeros. Otherwise the solution is called non-oscillatory.

Definition 2: A solution $x(t) = \left[x_1(t), x_2(t), \ldots\ldots, x_m(t) \right]^T$ is said to oscillate if it is eventually trivial or if at least one component does not have eventually constant signum. Otherwise the solution is called non-oscillatory.

We will use definition (2) to obtain the sufficient conditions for the oscillation of all solutions. However, as we will prove in theorem (2) for the system of differential equations, if all solutions of the system oscillate with respect to one of the two definitions (1) and (2), then they also oscillate with respect to the other.

We have found two explicit sufficient conditions for the oscillations of the linear autonomous delay symmetric DCNN. The results are based on the work of Ferreira and Györi in (Ferreira, José M et al, 1987, p. 332-346). We utilize the logarithmic norm of $\mu(A_1) = \max_{\|u\|=1}(Hu, u)$ and $\mu(H) = \max_{\|u\|=1}(A_1 u, u)$ of the matrices H and A_1 to obtain explicit conditions for the oscillation and for the non-oscillation of all solutions of equation (1).

Theorem 1: Assume that $H, A_1 \in \mathbf{R}^{2 \times 2}$ and $\tau \in \mathbf{R}^+$, then, the following statements are equivalent.

A). every solution of equation (1) oscillates componentwise.

B). the characteristic equation $\det(\lambda I - H - A_1 e^{-\lambda \tau}) = 0$ has no real roots, where I is 2×2 identity matrix.

Theorem 2: Assume that $H, A_1 \in \mathbf{R}^{2 \times 2}$, $\tau \in \mathbf{R}^+$ and $\mu(H) \leq 0$, $\mu(A_1) \leq 0$.

Then each of the following two conditions is sufficient for the oscillations of all solutions of equation (1):

A). $\quad -\mu(A_1)\tau > \dfrac{1}{e}$, $\hspace{8cm}$ (2)

B). $\quad \sqrt{\mu(H) \cdot \mu(A_1)} > \dfrac{1}{2e\tau}$. $\hspace{7cm}$ (3)

Lemma 1: Assume that $H, A_1 \in \mathbf{R}^{2 \times 2}$ and $\tau > 0$ are such that

$$\mu(H) + \mu(A_1)e^{-\gamma\tau} < 0, \text{ for } \gamma \in \mathbf{R}^+ , \hspace{5cm} (4)$$

and

$$\inf_{\gamma < 0}\left[\frac{1}{\gamma}\mu(H) + \frac{1}{\gamma}\mu(A_1)e^{-\gamma\tau} \right] > 1 . \hspace{5cm} (5)$$

Then every solution of equation (1) oscillates.

Proof: Assume, for the sake of contradiction, that equation (1) has a non-oscillatory solution. Then, by theorem (1), the characteristic equation $\det(\lambda I - H - A_1 e^{-\lambda\tau}) = 0$ has a real root λ_0. But, then there exists a vector $u \in \mathbf{R}^2$ with $\|u\| = 1$ such that $(\lambda_0 I - H - A_1 e^{-\lambda_0\tau})u = 0$, hence,

$$\lambda_0 = \left(Hu + A_1 e^{-\lambda_0 \tau} u, u\right) = \left(Hu + A_1 u, u\right) e^{-\lambda_0 \tau} \le \mu(H) + \mu(A_1) e^{-\lambda_0 \tau} \quad,$$ and so, by equation (4), $\lambda_0 < 0$, and

$$1 \ge \frac{1}{\lambda_0}\left(\mu(H) + \mu(A_1)e^{-\lambda_0 \tau}\right).$$ This contradicts equation (5) and completes the proof.

Proof of Theorem 1: We apply lemma (1). As $\mu(H) \le 0$ and $\mu(A_1) \le 0$, equation (4) is satisfied and so it suffices to establish equation (5). First, assume that equation (2) holds. Then, by using the inequality $e^x \ge ex$, we see that for all $\gamma < 0$,

$$\frac{1}{\gamma}\left[\mu(H) + \mu(A_1)e^{-\gamma\tau}\right] \ge \frac{1}{\gamma}\left[\mu(H) + \mu(A_1)e(-\gamma\tau)\right] = e\left[-\mu(H) + \mu(A_1)\tau\right].$$

From this and equation (2), it follows that equation (5) holds. Next, assume that equation (3) hold. Then, by using the arithmetic mean-geometric mean inequality, we see that for all $\gamma < 0$,

$$\frac{1}{\gamma}\left[\mu(H) + \mu(A_1)e^{-\gamma\tau}\right] = -\frac{1}{\gamma}\left[-\mu(H) - \mu(A_1)e^{-\gamma\tau}\right]$$

$$\ge -\frac{2}{\gamma}\sqrt{-\mu(H)\mu(A_1)e^{-\gamma\tau}}$$

$$= -\frac{2}{\gamma}\sqrt{-\mu(H)\mu(A_1)} \cdot e^{-\frac{\gamma\tau}{2}}$$

$$\ge -\frac{2}{\gamma}\sqrt{\left[-\mu(H)\mu(A_1)\right]} \cdot e(-\frac{\gamma\tau}{2})$$

$$= e\sqrt{-\mu(H)\mu(A_1)} \cdot \tau,$$

from this and equation (3), it follows that equation (5) holds. The proof is complete.

3. Conclusion

This paper successfully established some new sufficient conditions for oscillation of symmetric cellular neural networks with delay. These conditions impose constrains on the system of dynamic state equations when the cells are working in linear region $\dot{x}(t) - Hx(t) - A_1 x(t-\tau) = 0$.

References

Arik, S. (2002). An improvement global stability result for delayed cellular neural networks. *IEEE Trans. Circuits Syst. I, Fundam. Theory Appl.*. 49:1211-1214.

Arik, S. (2003). Global robust stability of delayed cellular neural networks. *IEEE Trans. Circuits Syst. I, Fundam. Theory Appl.*. 50:156-160.

Arik, S. and Tavsanoglu, V. (2000). On the global asymptotic stability of delayed cellular neural networks. *IEEE Trans. Circuits Syst. I, Fundam. Theory Appl.*. 47: 571-574.

Chua L. O. and Yang, L. (1988). Cellular neural networks. *Circuits and Systems, IEEE International Symposium*. 2: 985- 988.

Chua, L.O. (1992). Cellular neural networks with nonlinear and delay-type tepmlete elements and no-uniform grids. *Int. J. Circuit Theory and Applications*. 20:449-459.

Chua, L.O. and Roska, T. (1990). Cellular neural networks with nonlinear and delay-type template elements. Proc. CNN-90. 12-25.

Chua, L.O. and Yang, L. (1988). Cellular neural networks: Applications. *IEEE Transactions on Circuits and Systems*. 35: 1273-1290.

Chua, L.O. and Yang, L. (1988). Cellular neural networks: Theory. *IEEE Transactions on Circuits and Systems*. 35: 1257-1272.

Chua,L.O. and Roska. (1990). T. Stability of a class of nonreciprocal cellular neural networks. *IEEE Transactions on Circuits and Systems*.37:1520-1527.

Civalleri, P. P. and Gilli, M. (1992). Some stability properties of CNN's with delay. *Cellular Neural Networks and their Applications, CNNA-92 Proceedings*, Second International Workshop. 94 -99.

Civalleri, P.P., Gilli, M. and Pandolfi, L. (1993). On stability of cellular neural networks with delay. *IEEE Transactions on Circuits and Systems: Fundamental Theory and Applications.*40 [3]:157-165.

Ferreira, José M. and Györi, I. (1987). Oscillatory behavior in linear retarded functional differential equations. *Journal of Mathematical Analysis and Applications*. 128[2]: 332-346.

Liao, T. L. and Wang, F. C. (1999). Global stability condition for cellular neural networks with delay. *Elecron. Lett..* 35: 1347-1349.

Liao, T. L. and Wang, F. C. (2000). Global stability for cellular neural networks with time delay. *IEEE Trans. Neural Netw..*11:1481-1484.

Roska, T., Wu, C. W., Balsi, M. and Chua, L. O. (1992). Stability and dynamics of delay-type general cellular neural networks. *IEEE Trans. Circuits and Syst..* 39:487-490.

Savaci, F. A and Vandewalle, J. (1992). On the stability analysis of cellular neural networks. *Cellular Neural Networks and their Applications, CNNA-92 Proceedings*, Second International Workshop. 240 – 245.

Takahshi, N. N. (2000). A new sufficient condition for complete stability of cellular neural networks with delay. *IEEE Trans. Circuits Syst. I, Fundam. Theory Appl..* 47:793-799.

Zou, F. and Nossek, J. A. (1991). Stability of Cellular neural networks with opposite sign templets. *IEEE Trans. Circuit and Syst*. 38:675-677.

Study on Oxidation Effect of Ozone on Petroleum-Based Pollutants in Water

Mengfu Zhu, Haiyan Wang, Hongbo Su, Xiudong You & Wenli Jin

National Engineering Research Center for Biological Protective Equipment, Tianjin 300161, China

Tel: 86-22-8465-6831   E-mail: zmf323@163.com

Abstract

The removal of petroleum-based pollutants from water by ozone is studied. The results indicate that the oxidation effect of ozone on the petroleum-based pollutants is associated with water temperature, pH, dosage of ozone and reaction time. The removal efficiency of petroleum-based pollutants increases with the rise of temperature, pH, amount of ozone and reaction time, and reaches 83% under the conditions that the ratio of ozone to petroleum-based pollutants is 1:1 and the reaction time is 10 min. GC/MS analysis reveals that the amount of petroleum-based pollutants in water is reduced 39% from the previous 61 organics to 37 organics, the total peak area is reduced 36% after ozone oxidation treatment. Therefore, ozone has an excellent effect on the removal of petroleum-based pollutants and can be applied in the treatment of petroleum wastewaters.

Keywords: Ozone, Petroleum-based pollutants, Oxidation, Water treatment

Preface

Petroleum has become a major pollutant in sea, river and lake in China because of the excessive discharge of petroleum wastewaters, frequently occurred leakage accidents of petroleum, settlement of oil and hydrocarbon emitted in atmosphere, as well as oil spill from sea bottom (Chen, Guohua, 2002, p. 5-27), it resulted in severe harm to environment and human health. Ozone has so powerful oxidation that it is able to change the composition and structure of petroleum, and oxidize the high molecular organics into low molecular organics, or decompose some organics directly into CO_2 and H_2O. As a result, the nonbiodegradable organics in the raw water are converted into biodegradable organics (Lin C K et al, 2001, p. 699-704; Jiangning Wu et al, 2007, p. 1-5; Jin Anotai et al, 2007, p. 345-349). For finding an effective method to remove the petroleum-based pollutants from water, this paper investigates the oxidation effect of ozone on petroleum-based pollutants through GC/MS analysis and determination of petroleum content in water before and after ozone oxidation.

1. Experiment

1.1 Reagents and equipments

(1) Reagents

Designated grade of carbon tetrachloride and anhydrous sodium sulfate, from Tianjin Changmao Chemical Reagent Company; Analytically pure potassium permanganate, from Tianjin No. 1 Chemical Reagent Factory; Sodium oxalate (standard reagent), from Beijing Chemical Company.

(2) Equipments

JDS-105U infrared spectrophotometric oil analyzer, from Jilin Beiguang Analytical Instrument Company; 5890-5971 gas chromatography-mass spectrometry (GC/MS) analyzer, from Agilent Technologies of US.

1.2 Process flow

Figure 1 is a process flow diagram of the experiment. Ozone is prepared by passing oxygen or an oxygen-containing gas through an ozone generator. Output and concentration of ozone are controlled by regulating the electric current of ozone generator and the oxygen input. Ozone, flowing into the reactor from the bottom, reacts with the petroleum-based pollutants that flow from the top of the reactor. The ozone generator (Φ1600 mm×85 mm) is made from quartz glass.

2. Result and discussion

2.1 Effects of ozone oxidation on the removal of petroleum-based pollutants from water

Ozone oxidation includes direct reaction and indirect reaction. Its reaction rate is associated with the concentrations of pollutants, ozone and ·OH, as well as the direct reaction constant of ozone and indirect reaction constant of ·OH. Therefore, there are many factors that have effects on the ozone oxidation. This paper mainly discusses the effects of ozone dosage, reaction time, reaction temperature and pH on the oxidation of petroleum-based pollutants.

2.1.1 Ozone dosage

Ozone dosage refers to the amount of ozone that flows from the ozone generator into the oxidation reactor, which includes the consumed ozone, residual ozone in water and residual ozone in tail gas. Ozone dosage is an important parameter in the ozone treatment of water, and directly affects the processing efficiency and operation cost. Overlow dosage results in a poor oxidation efficiency; whereas overhigh dosage results in the formation of intermediate products which have adverse effects on the following treatment, and lead to the increase of investment and operation cost.

Table 1 indicates that the residual ozone in either water or tail gas is associated with the ozone dosage. When the ozone dosage is lower than the petroleum content, the residual ozone is low and utilization rate of ozone is high; however, when the ozone dosage is higher than the petroleum content, the residual ozone is high and utilization rate of ozone is low.

Figure 2 exhibits the effect of ozone dosage on the oxidation of petroleum when the reaction is 10min. The results indicate that the petroleum removal and oxidation efficiency increase with the rise of ozone dosage. The petroleum removal efficiency is higher than 80% when the ozone dosage is equal to the petroleum content, and declines in its growth rate with the further rise of ozone dosage. It is because the increase of ozone dosage results in the rise of ozone concentration in water and oxidation ability, in turn leads to an increased petroleum removal efficiency. However, the reaction between ozone and petroleum reaches an equilibrium when the ratio of ozone dosage to petroleum content is 1:1, and the petroleum removal efficiency cannot be increased significantly any more with the further increase of ozone dosage.

2.1.2 Reaction time

Figure 3 exhibits the effect of reaction time on the oxidation of petroleum under the condition that the ratio of ozone dose to petroleum content is 1:1. It indicates that the petroleum removal rate increases with the reaction going on, and levels off after 10 minutes.

2.1.3 Reaction temperature

Reaction rate constant of ozone with organics in water increases with the rise of temperature. Figure 4 exhibits the effect of reaction temperature on the oxidation of petroleum under the conditions that the ratio of ozone dose to petroleum content is 1:1 and the reaction time is 10 min. With the rise of water temperature, the oxidation ability of ozone increases, the petroleum removal rate in turn increases. However, the solubility of ozone in water decreases with the rise of reaction temperature, which leads to the decline of utilization ratio (Rischbieter E et al, 2000, p. 338-340).

2.1.4 pH

Reaction rate of ozone with organics in water is associated with the form of organics. That is to say, the reaction rate of ozone with dissociated organics is faster than that with associated organics under the same conditions. Figure 5 exhibits the effect of pH on the oxidation. It indicates that the oxidation effect of ozone on petroleum increases with the rise of pH. It is because the proportion of dissociated organics increases, in turn the reaction rate increases with the rise of pH. However, the turbidity and chroma of the studied petroleum-polluted water increase remarkably when pH is higher than 7, which has an adverse effect on the investigation of experimental results.

In fact, ozone directly reacts with petroleum at low pH; whereas, ·OH, a strong oxidant resulted from the reaction of OH^- with ozone at high pH, initiates the chain reaction of ozone oxidation which is nonselective and very rapid (Nemes A et al, 2000, p. 287-304).

2.2 Removal effect of petroleum-based pollutants by ozone

Ozone has an excellent effect on the removal of petroleum-based pollutants from water under the conditions of 23 ℃, pH of 7.2, 4.0 mg/L ozone dosage and 10 min reaction. Figure 6 reveals that the petroleum content decreases from 4.0 mg/L to 0.7 mg/L and the average removal rate is 82.50% after ozone treatment. Petroleum mainly consists of alkane, aromatic hydrocarbons, cycloalkane and etc. High molecular organics can be turned into low molecular organics by oxidation of ozone, and parts of them are directly decomposed into CO_2 and H_2O.

2.3 GC/MS analysis

2.3.1 Raw water

By combining GC boiling point separation with MS fragment pattern identification, organics in water can be identified on the basis of their boiling point differences resulting form the differences in inter-molecular force, namely, Van der Waals force, which is associated with polarity of molecular. Figure 7 shows GC/MS chromatograms of raw water containing 4.0 mg/L petroleum. There are in total 72 peaks arranged from low to high in order of boiling point, and each peak is correspond to a certain organic compound. The total peak area is 1.14×10^8.

The results of GC/MS analysis indicate that 61 organics have been detected from raw water, including 24 alkanes, 10 esters, 6 olefins, 5 acids, 3 alcohols, 2 ethers, 2 amines and 9 other compounds. Most of them have molecular weights of 100~300. Alkanes constitute 39.34% of the total organics, and their peak areas constitute 64.76% of the total peak area, which indicates petroleum is a mixture of alkanes.

2.3.2 Ozone-oxidized water

Figure 8 shows GC/MS chromatograms of ozone-oxidized water under the conditions of 23 ℃, pH of 7.2, 4.0 mg/L ozone and 10 min reaction. There are in all 53 peaks with the total area of 7.30×10^7 which declines 35.96% comparing with the raw water. From the ozone-oxidized water, we have detected 37 organics including 6 alkanes, 5 esters, 2 olefins, 7 acids, 3 alcohols, 2 aldehydes, 1 ethers, 5 amines and 6 other compounds which decline by 39.34% comparing with the raw water. 48 organics are removed from the raw water by ozone oxidation. As a result, there are 13 organics that can not be removed, together with 25 newly increased organics in the ozone-oxidized water. The removed organics mainly include alkanes, olefins, esters, ethers and etc. The newly increased organics mainly include acids, amines and aldehydes. It indicates that most organics in petroleum can be oxidized into low molecular intermediate products, and about 35% organics are directly decomposed into CO_2 and H_2O.

The column temperature in GC/MS analysis is commonly between 45~300 ℃, which makes the organics of high boiling point difficult to be separated, and the volatile organics easy to be evaporated. In addition, some polar organics of low molecular weight need deriving before they can be effectively separated. Therefore, there is a certain range for the organics detectable by GC/MS analysis: organics of either too high molecular weight or too low molecular weight can not be effectively detected.

3. Conclusion

Ozone has so powerful oxidation that it is able to change the composition and structure of petroleum, and oxidize the high molecular organics into low molecular organics, or decompose some organics directly into CO_2 and H_2O. As a result, the nonbiodegradable organics in the raw water are converted into biodegradable organics. In short, the petroleum-based pollutants can be effectively removed from water by ozone. Ozonation can be used separately or combined with biodegradation, membrane separation technique and etc. to process petroleum-contained water.

References

Chen, Guohua. (2002). *Treatment of Oil-Polluted Water.* Beijing: Chemical Industry Press, p. 5-27.

Jiangning Wu, Huu Doan & Simant Upreti. (2007). Decolorization of aqueous textile reactive dye by ozone. *Chemical Engineering Journal*, 11(5), 1-5.

Jin Anotai, Rosawan Wuttiponga & Chettiyappan Visvanathan. (2007). Oxidation and detoxification of pentachlorophenol in aqueous phase by ozonation. *Journal of Environmental Management*, 85, 345-349.

Lin C K, Liu J C, Chen M C & Tsai T Y. (2001). Enhanced biodegradation of petrochemical wastewater using ozonation and BAC advanced treatment system. *Water Research*, 35(3), 699-704.

Nemes A, Fabian I & Gordon G. (2000). Experimental aspects of mechanistic studies on aqueous ozone decomposition in alkaline solution. *Ozone Science and Engineering*, 22(3), 287-304.

Rischbieter E, Stein H & Schumpe A. (2000). Ozone solubilities in water and aqueous salt solutions. *Journal of Chemical Engineering Data*, 45, 338-340.

Table 1. The correlation between ozone dosage and residual ozone

Ozone dosage (mg/L)	Residual ozone in water (mg/L)	Residual ozone in tail gas (mg/L)
1.21	0.01	0.50
2.80	0.01	0.62
4.09	0.02	0.87
9.46	1.22	2.56
12.40	2.50	3.10

* Petroleum content is 4.5 mg/L; Flow rate of water is 1 L/min; Flow rate of tail gas is 2 L/min.
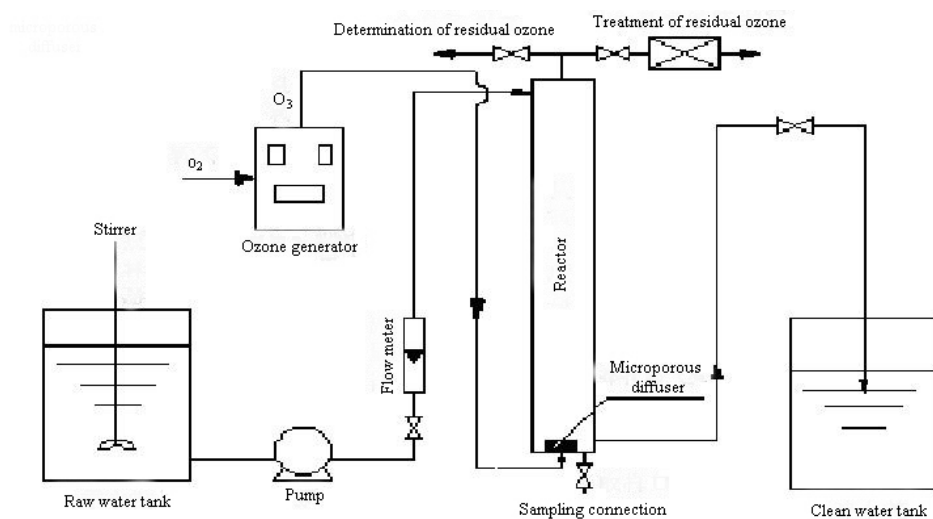
Figure 1. Process flow diagram of the experiment
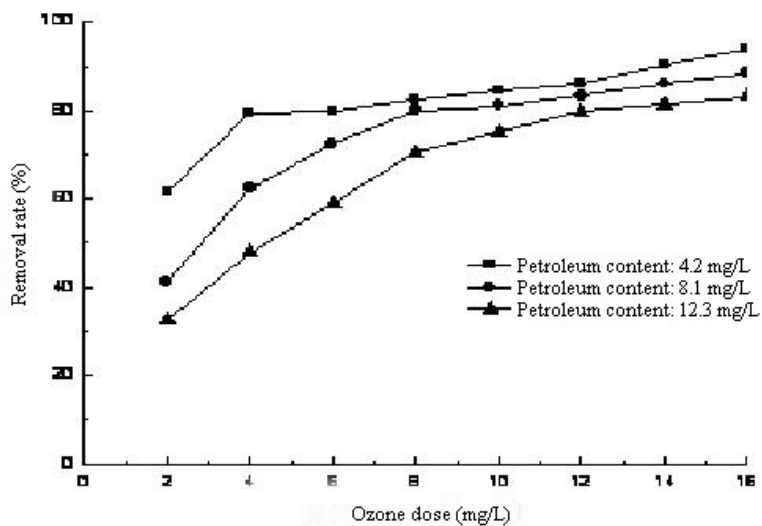
Figure 2. The effect of ozone dosage on the oxidation of petroleum
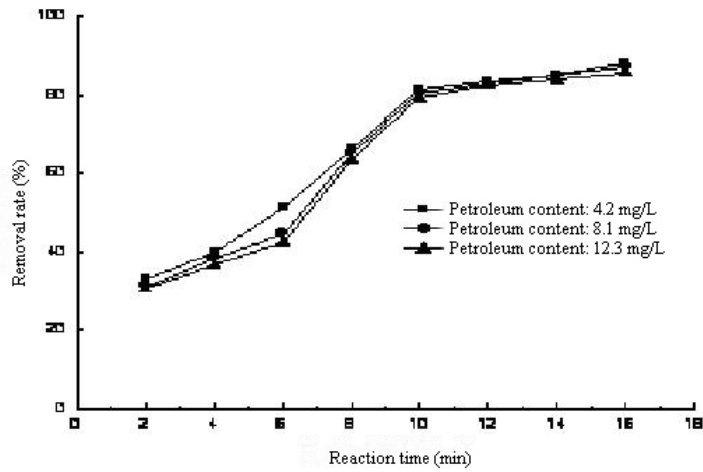
Figure 3. The effect of reaction time on the oxidation of petroleum
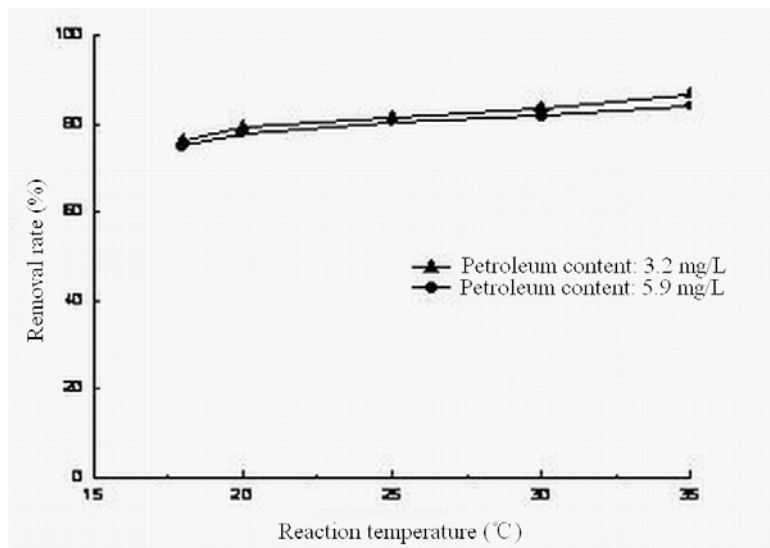

Figure 4. The effect of reaction temperature on the oxidation of petroleum
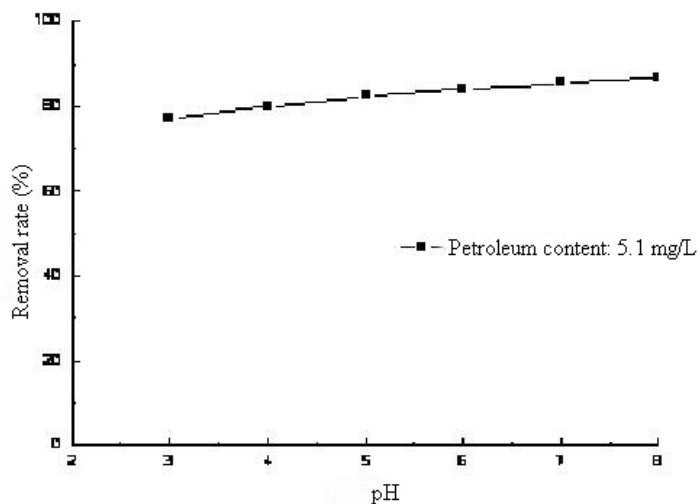
Figure 5. The effect of pH on the oxidation of petroleum
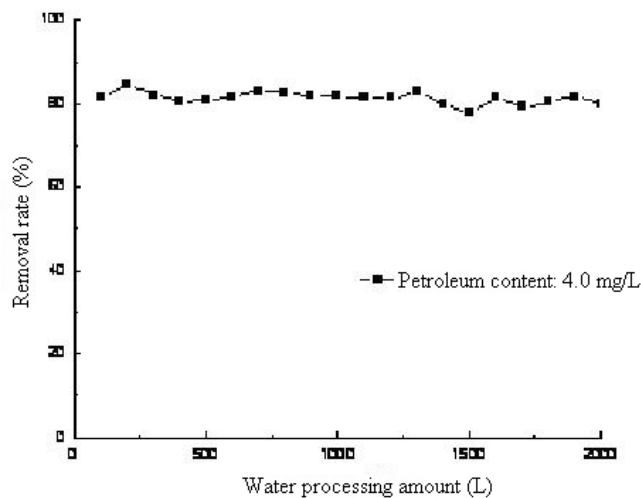
Figure 6. The removal effect of petroleum-based pollutants by ozone
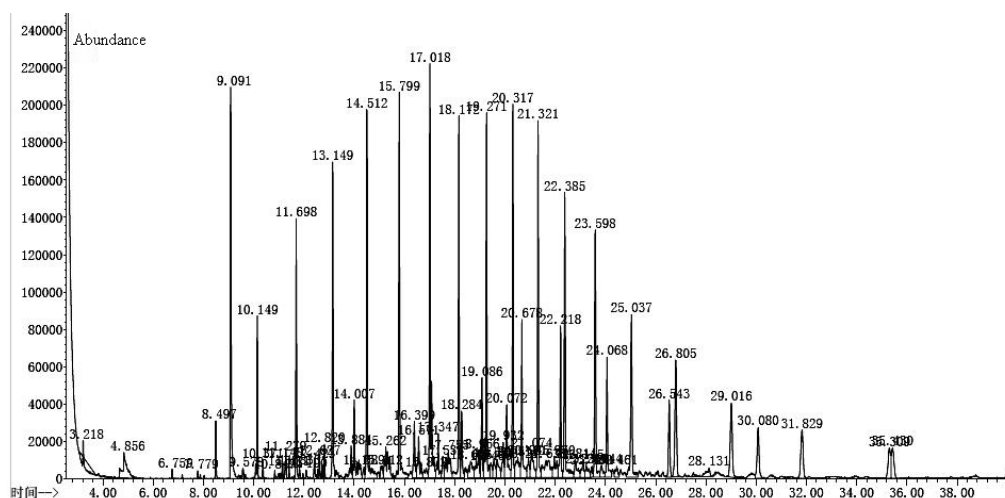
Figure 7. GC/MS chromatograms of raw water
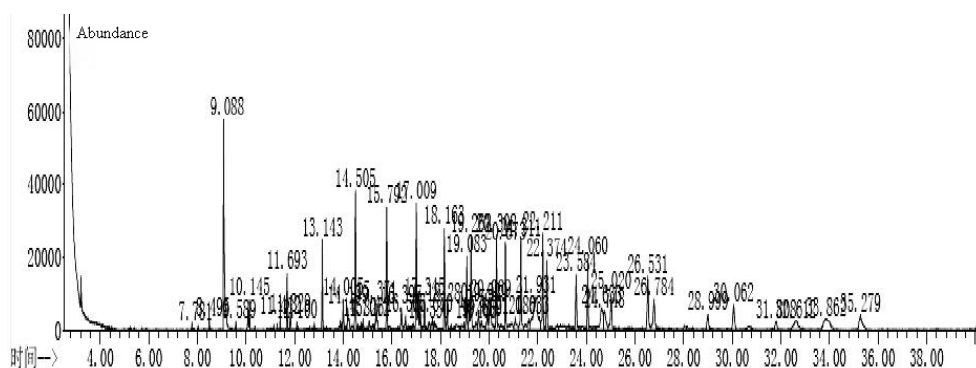
Figure 8. GC/MS chromatograms of ozone-oxidized water

Decontamination of Mercury Contaminated Steel (API 5L-X52)

Using Iodine and Iodide Lixiviant

Narongsak Chaiyasit

Interdisciplinary Environmental Science, Chulalongkorn University

Phayathai, Bangkok, 10300, Thailand

Tel: 66-89-204-8199   E-mail: thomas_2106@yahoo.com

Charnwit Kositanont (Corresponding author)

Interdisciplinary Environmental Science, Chulalongkorn University

Phayathai, Bangkok, 10300, Thailand

Tel: 66-2-218-7667   E-mail: charnwit@sc.chula.ac.th

Sheila Yeh, Darrell Gallup & Lyman Young

Chevron Energy Technology Company

100 Chevron Way, Richmond, CA, 94802, USA

Tel: 1-510-242-4037

E-mail: swyeh@chevron.com, Dgallup@chevron.com, layo@chevron.com

Abstract

Investigations assessed the surface chemistry, morphology and depth profile of Hg for gas processing pipe steel coupons of API 5L-X52 after adsorption with elemental Hg at 25 ^{0}C in the presence of air. We investigated the effect of Hg adsorption periods and surface Hg levels as well as characterizations of Hg depth profiles. We observed no reasonable correlation between surface Hg levels and Hg adsorption periods. Forms of Hg found on the top surface and in the depth profile were in oxide and elemental forms, respectively. However, most of the Hg present was superficial and did not penetrate below the surface significantly. The lowest concentration lixiviant, with 0.2 Molar iodine and 2.0 Molar potassium iodide, worked well with all ranges of Hg contamination observed, with the final surface Hg levels of less than 0.1 atom% by XPS analysis, for a relative percentage of Hg removal about 99%.

Keywords: Mercury, Adsorption, Depth profile, Decontamination

1. Introduction

Mercury is a naturally occurring element found in geologic hydrocarbons in the Gulf of Thailand. The first observations of mercury in Thai offshore oil and gas operations appeared in the late 1980s (McDaniel, et al., 1998). The mercury-laden hydrocarbons, upon contact with steel, for example, that of petroleum pipeline and separation processes, cause mercury deposition on the metal surfaces. A study conducted at a North German gas field located in the Rotliegend to assess mercury in steel equipment used for natural gas production revealed that mercury of less than 1 and more than 80 mg/kg was found in their tubing and pipe (Zettlizer and Kleinitz, 1997). As a result, the potential for mercury deposits on steel must be considered when classifying production and processing equipment for decommissioning and disposal.

A study, conducted to identify mercury decontamination techniques on porous surfaces, showed that chemical cleaning

methods involving iodine, as oxidizing, and iodide, as complexing agents (so called iodine/iodide lixiviant), could remove up to 90% of elemental mercury (Ebadian, 2001). However, the former study used relatively lower surface mercury concentrations, and further made no assessment regarding its effectiveness for mercury below the surface.

This study assesses mercury levels both on the surface and in the depth profile, and further identifies an optimum iodine concentration for use in the decontamination by the iodine/iodide lixiviant method. Reproducing in the laboratory a high pressure environment to match that of the subsea pipeline would be possible, but very difficult. However, because of the relatively high incompressibility of liquid mercury, the interaction between mercury and steel is not expected to be a strong function of pressure. Therefore, the study was performed at ambient pressure. Ambient temperature (25°C) is a reasonable match to the temperatures of the subsea pipeline.

2. Materials and Methods

2.1 Steel Coupons

The steel coupons used in the experiment measured 2 x 2 x 1.27 cm (width x length x depth), and we prepared them from virgin subsea petroleum pipe with an American Petroleum Institute (API) specification of 5L-X52. We protected five of the surfaces of the cubes with a coating of silicone, excluding the internal concave surface. Table 1 presents the chemical composition of the coupon steel (Hernandez-Rodriguez et al., 2007).

2.2 Mercury Adsorption

We cleaned the uncoated surface with a liquid detergent and placed the coupons in 250 ml sealed bottles, each containing 0.5 kg of elemental mercury with air in the headspace. For each coupon, we immersed the uncoated surface directly into the liquid elemental mercury, and mercury adsorption continued under a controlled temperature of 25^oC inside an incubator for one of six (6) different pre-determined adsorption periods (15, 30, 45, 60, 75 and 90 days).

2.3 Mercury Decontamination

Upon reaching the pre-determined mercury contamination periods, we retrieved the Hg contaminated steel coupons and removed the silicone coating. Then, we placed coupons into 100 ml tight lid laboratory bottles containing 30 ml of iodine and potassium iodide lixiviant with varied iodine concentrations of 0, 0.2, 0.4, 0.6, 0.8 and 1.0 Molar and constant potassium iodide concentration at 2.0 Molar, respectively. The decontamination proceeded in the dark, in a closed cabinet, to prevent loss of iodine due to the sunlight. Upon reaching 24 hours of decontamination we removed the steel coupons from the bottles, rinsed each thoroughly with doubly-distilled water, and placed each in a separate, tightly sealed wide-mouthed High Density Polyethylene (HDPE) bottle for subsequent analysis.

2.4 Metal Coupon Analysis

At the end of each mercury adsorption and decontamination experiment, we analyzed the steel coupons for surface morphology and chemistry using the JEOL JSM-5300 Scanning Electron Microscope with Energy Dispersive X-Ray (EDX) fluorescence spectrophotometer. We measured surface elements and compounds, including the compositional depth profiles, using the Phi Quantera Scanning X-ray Microprobe X-ray Photoelectron Spectrometer (XPS), within two weeks after completion of the adsorption and decontamination experiments. For the XPS analysis, sets of four coupons were mounted on a sample platen using standard high vacuum techniques. Detailed analyses consisted of scans of the Fe 2p, Si 2s/Si 2p/Hg 4f, C 1s, and O 1s spectral windows, with data acquisition time of 45 minutes and the instrument operating at a resolution of about 1.2 eV. For at least one of the several areas, we additionally obtained depth profiles. In the depth profiles, we acquired data for the same spectral regions, and etched the surface with a SiO_2-calibrated rastered Ar-ion beam operated with azimuthal sample rotation. We used standard XPS data handling techniques to obtain the surface compositional and chemical data, as well as the depth profile characterizations.

3. Results and Discussion

3.1 Surface Morphology and Chemistry after Adsorption of Elemental Mercury (Hg^0)

Illustrations from SEM, as shown in Fig. 1, revealed mercury as spherical droplets of various sizes on the coupon surface. The larger droplets could be greater than 10 µm in diameter, whereas the smaller ones could be less than 1 µm. Surface distribution of the Hg droplets was irregular with respect to both adsorption site and droplet size.

Fig. 2 presents the results of surface Hg analysis using EDX at the end of each Hg^0 adsorption period, and shows that the surface Hg levels range from less than 5 to 45 atom%. However, analysis of surface Hg levels using XPS analysis two weeks after the end of each Hg^0 adsorption period showed much lower surface Hg concentrations, ranging from less than 0.5 to about 3.0 atom%. We found no reasonable correlation between the surface Hg levels and the adsorption periods for either of the surface analysis techniques used. Fig. 3 shows surface Hg levels at the end of each Hg adsorption period by XPS analysis.

The XPS chemical state analysis, with Hg 4f7/2 at 100.7 eV and Hg 4f5/2 at 104.7 eV, revealed the presence of Hg oxide on the steel coupon surface (Motohiro et al., 2003, Kleiman et al., 1982 and Humbert, 1986). The results of the

above suggest that at the end of the Hg^0 adsorption period, Hg was predominantly found in its elemental form. After two weeks, however, significant levels of the surface Hg vaporized due to the high Hg^0 vapor pressure, and leaving behind the less volatile Hg oxide on the coupon surface.

3.2 Depth Profiling and Chemistry after Adsorption of Elemental Mercury (Hg^0)

The XPS spectra showed that after etching the steel to only 6 nm from the topmost surface, the binding energies of Hg 4f7/2 and Hg 4f5/2 were shifted to 99.6 and 104.0 eV, respectively, indicating subsurface Hg was in the zero valence state of elemental mercury in contrast to the oxide state found on the topmost surface (Motohiro et al., 2003, Kleiman et al., 1982 and Humbert, 1986). A control depth profile experiment on HgO showed no beam-induced reduction.

The Hg concentration depth profiles showed that most Hg was present within the short depth of only about 10 nm from the topmost surface. The levels of Hg in the depth profile were low, mostly below 0.1 atom%. Therefore, Hg is present on the surface only and does not penetrate significantly into the depth. A previous study of field samples of gas processing pipe collected in a gas field of Northern Germany also with naturally-occurring mercury reported a similar finding. This previous study indicated that mercury is only adsorbed on the steel surface and did not penetrate into the depth (Zettlitzer and Kleinitz, 1997). Figs. 4 through 6 show Hg levels in the depth profile at the end of 30, 75 and 90 day of Hg^0 adsorption, respectively. Note that Hg levels in these figures are multiplied by 50 to better match the scale of other elements' concentrations.

3.3 Surface Morphology of the Steel Coupons after Mercury Decontamination

Surface morphology of steel coupons after the mercury decontamination of 30, 75 and 90 days of Hg^0 adsorption is shown in Figs. 8 through 10, respectively. The post-decontamination surface morphology showed no droplets of elemental mercury. We also found that with higher iodine concentrations, more surface corrosion occurred. These observations are consistent with iodine as an oxidizing agent that not only oxidized Hg present on the top surface, but also corroded the steel surface allowing contact with any small amount of Hg below the surface. Therefore further investigation of Hg in the depth profile after the decontamination is deemed unnecessary.

3.4 Surface Chemistry of the Steel Coupon after Mercury Decontamination

The XPS analysis of the surface mercury after the mercury decontamination of 30, 75 and 90 day Hg^0 adsorption, respectively, using various concentrations of iodine (0-1.0 Molar) and at a constant concentration of potassium iodide (2.0 Molar) showed that there was no major difference in the resulting surface Hg level due to different iodine concentrations, including the control experiment without iodine (0 Molar). This finding can be due to the oxide form of mercury found on the surface which reportedly could be peeled off as a metal oxide scale leaving just a thin oxide film (Zalavutdinov, 2001). Therefore, removal of the oxide form of Hg could be potentially due to the peeling off process. However, since the peeled off mercury oxide scale might have been obscuring minute levels of Hg^0 present in the coupon's subsurface, iodine and potassium iodide are still required to stabilize all possible mercury for further handling and final disposal. Other surface cleaning techniques, such as surface brushing or polishing, could make toxic mercury oxide become airborne. Once airborne, the contaminant would pose higher potential exposure risks to both humans and the environment from any emissions. A previous investigation showed that the iodine and iodide lixiviant mobilized mercury in solid wastes whether in the form of oxides, sulfides, or elemental through the oxidation and complex-forming reactions (Ebadian et al, 2001).

The EDX analysis of the coupon surfaces after the decontamination of 30, 75 and 90 day Hg^0 adsorption showed no mercury present. Note that the detection limit of the employed EDX is less than 1 atom% Hg. However, the XPS analysis, with its lower surface detection limit, revealed the maximum levels of mercury on the coupon surfaces after the decontamination of 30, 75 and 90 day Hg^0 adsorption of 0.1, 0.19 and 0.14 % atom, respectively, at various iodine concentrations. We present these data in Figs. 10 through 12.

3.5 Mercury Removal and Iodine Concentrations

Fig. 13 plots the percentage of Hg removed by the decontamination of 30, 75 and 90 day Hg^0 adsorption coupons using various concentrations of iodine between 0 and 1.0 Molar with a constant concentration of potassium iodide (2.0 Molar). These data demonstrate that there was no significant difference, in terms of surface Hg removal, among the various concentrations of iodine used, including with no iodine. As mentioned earlier, iodine is required to oxidize elemental mercury present on or just below the surface. As a result, we find 0.2 Molar iodine is the lowest iodine concentration that should be used. Taking into account the surface Hg levels by the EDX analysis of about 40 atom% generally found in 30, 75 and 90 day Hg^0 adsorption samples and those of the same set after the decontamination with the maximum Hg levels of 0.1 atom% Hg by XPS, the relative percentage of Hg removal using iodine/iodide of 0.2/2.0 Molar is, therefore, more than 99%.

4. Conclusion

We observed mercury as spherical droplets of Hg^0 attached on the steel coupon surface at the end of each adsorption

period, and found the Hg concentration ranged from less than 5 to about 45 atom% by EDX analysis. Examination of the steel coupon surfaces using XPS analysis two weeks later found Hg in the oxide form with surface concentrations ranging from less than 0.5 to about 3.0 atom% of Hg. These differences suggest loss of Hg through vaporization due to high Hg^0 vapor pressure, leaving much lower Hg levels on the coupon surface, and only in the oxide form. This knowledge is critical in the planning process to prevent and control Hg vapor as well as HgO particulates during any decontamination activity. XPS depth profile analysis further showed that Hg was present predominantly on the topmost surface to only about 10 nm depth. Insignificant concentrations of less than 0.1 atom% Hg by XPS analysis were observed and persistent throughout the depth profile regardless of the Hg^0 adsorption periods investigated. These data indicate that Hg, under the applied conditions, was present only on the top surface and did not penetrate significantly into the depth. The decontamination of Hg using iodine and potassium iodide lixiviant showed that there was no significant difference in the surface Hg concentrations after the decontamination with various iodine concentrations applied, including even the treatment with no iodine. However, since iodine would be needed to oxidize elemental Hg, we recommend a minimum concentration of 0.2 Molar iodine to remove all mercury forms. Other means of surface cleaning such as surface polishing could make toxic mercury and mercury oxide airborne and would pose significantly greater environmental and health risks. With 0.2 Molar iodine, we observed substantial decontamination, with mercury removal rates of 99%.

References

Ebadian, M. A. (2001). *Mercury contaminated material decontamination methods: investigation and assessment.* Hemispheric Center for Environmental Technology, Florida International University, Miami, Final Report prepared for US Department of Energy, Office of Environmental Management, Office of Science and Technology.

Hernandez-Rodriguez, M. A. L., Martinez-Delgado, D., Gonzalez, R., Perez Unzueta, A., Mercado-Solis, R. D., Rodriguez, J. (2007). Corrosion wear failure analysis in a natural gas pipeline. *Wear*, 263, 567-571.

Humbert, P. (1986). An XPS and UPS photoemission study of HgO. *Solid State Communications*, 60, 21-24.

Kleiman, G. G., Castro, S. G. C., Rogers, J. D., Sundaram, V. S. (1982). Systematics of final state screening in 5d metals. *Solid State Communications*, 43, 257-260.

McDaniel, M. F., Kulachol, K., Siripatrachai, T., Lambert, C. E., Leuschner, K. J. (1998). Mercury in the gulf of Thailand: a risk communication success story. Paper SPE 46871 presented at the 1998 SPE International Conference on Health, Safety and Environment in Oil and Gas Exploration and Production, Caracas, Venezuela, 7-10 June 1998, Society of Petroleum Engineers, Inc..

Motohiro, U., Berglund, A., Cardenas, J., Pohl, L., Watari, F., Bergman, M., Sjöberg, S. (2003). Surface analysis of dental amalgams by x-ray photoelectron spectroscopy and x-ray diffraction. *Dental Materials* 19 639 – 644.

Zalavutdinov, R. Kh., Dai, Y., Gorodetsky, A. E., Bauer, G. S., Alimov, V. Kh., and Zakharov, A. P. (2001). A study on martensitic and austenitic steels after exposure in mercury at 573 K up to 5000 h. *Journal of Nuclear Materials*, 296, 219 – 224.

Zettlitzer, M., and Kleinitz, W. (1997). Mercury in steel equipment used for natural gas production-- amounts, speciation and penetration depth. *Oil Gas European Magazine,* 23, 25 – 30.

Table 1. Composition in weight- and atom-% (by EDX) of the surface of the API 5L-X52 steel coupons.

Element	Weight-%	Atom-%
Iron (Fe)	75.2±10.4	45.5±14.4
Manganese (Mn)	0.9± 0.1	0.5± 0.2
Carbon (C)	11.4± 4.2	29.9± 5.8
Oxygen (O)	12.6± 6.4	24.2± 9.1
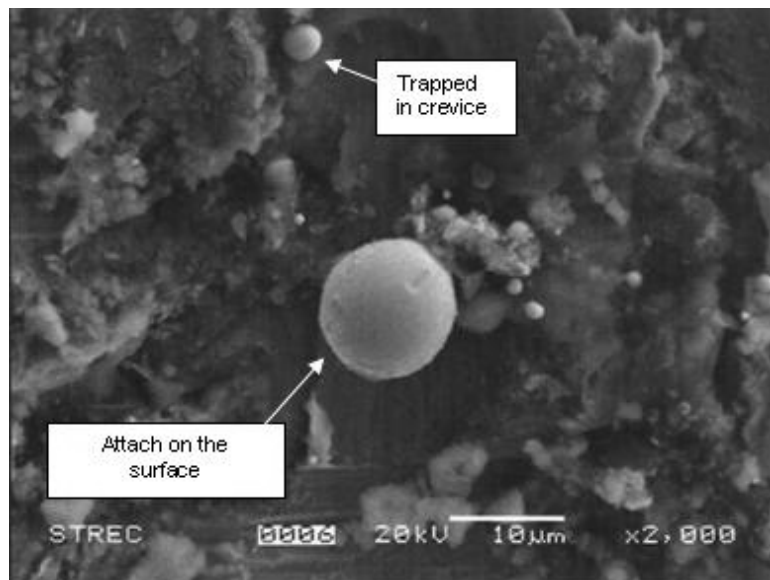
Figure 1. Spherical Hg^0 droplets are present on the metal coupon surface following adsorption
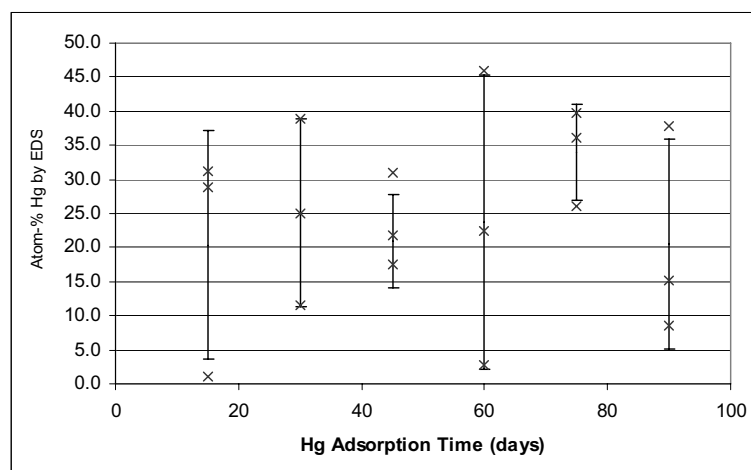
Figure 2. Surface Hg concentrations at the end of each Hg adsorption period using EDX analysis
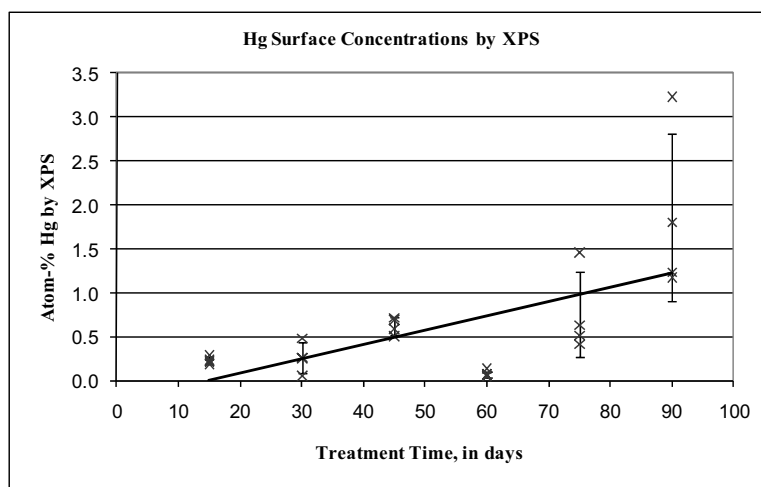
Figure 3. Surface Hg levels by XPS analysis at the end of each Hg^0 adsorption period
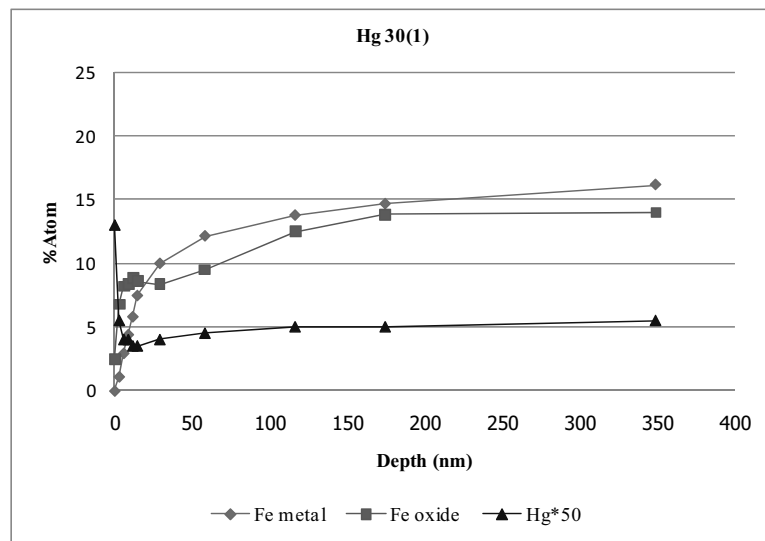
Figure 4. Hg in the depth profile of the 30 day Hg^0 adsorption coupon
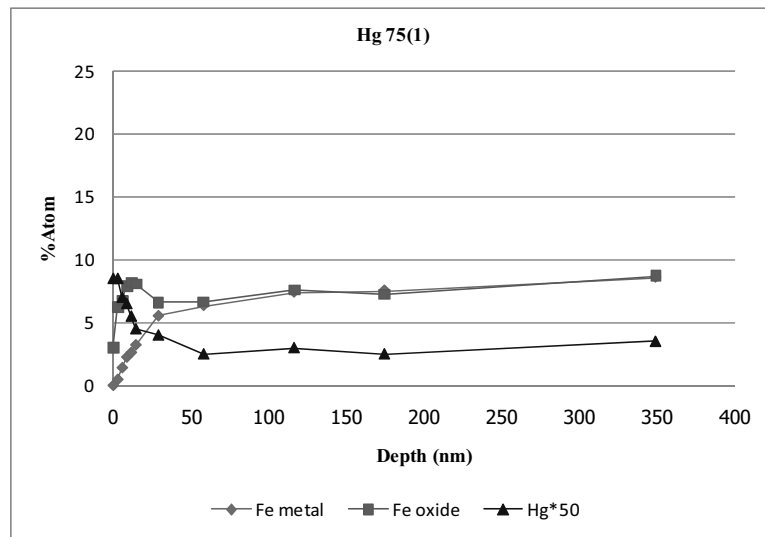
Figure 5. Hg in the depth profile of the 75 day Hg^0 adsorption coupon
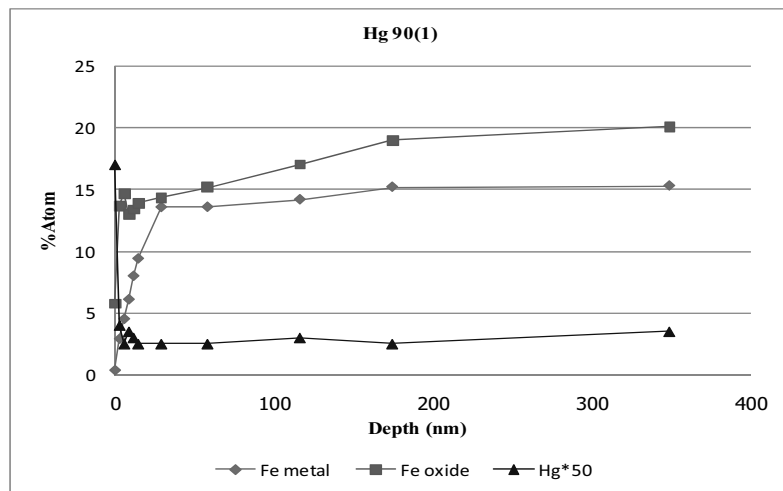
Figure 6. Hg in the depth profile of the 90 day Hg^0 adsorption coupon

I(0)   I(0.2)   I(0.4)

I(0.6)   I(0.8)   I(1.0)

(X5000)
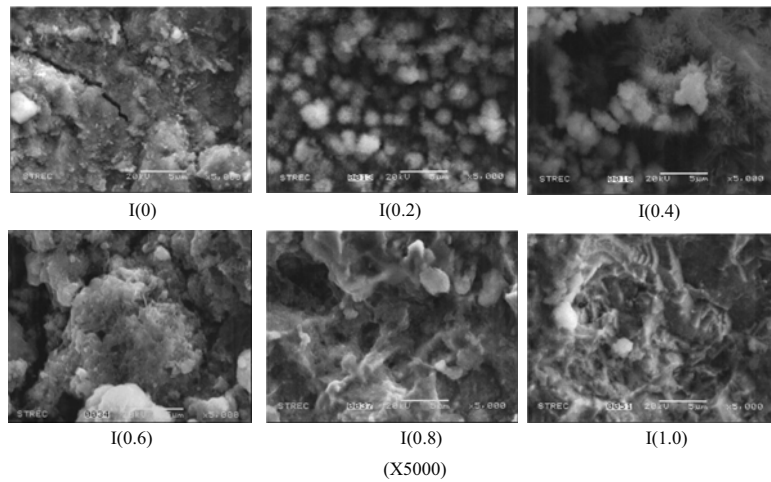
Figure 7. Surface morphology of the 30 day Hg^0 adsorption coupons after lixivient treatment
The concentration of iodine, ranging from 0 Molar to 1.0 Molar, is listed below the corresponding micrograph

I(0)   I(0.2)   I(0.4)

I(0.6)   I(0.8)   I(1.0)

(X5000)
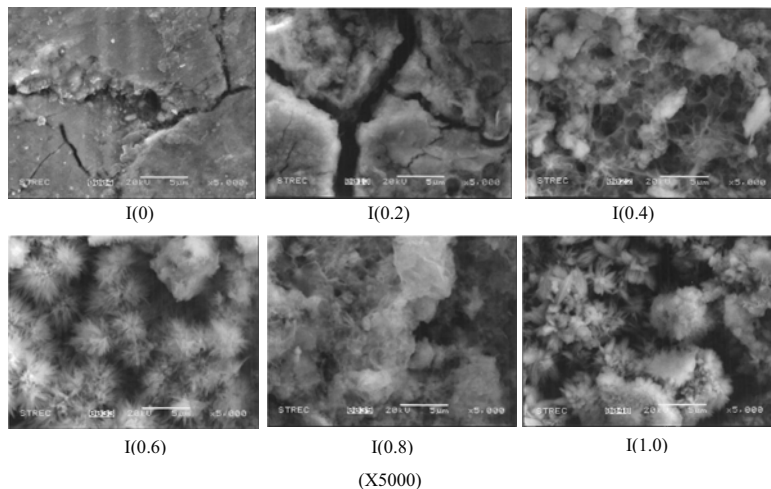
Figure 8. Surface morphology of the 75 day Hg^0 adsorption coupons after lixivient treatment
The concentration of iodine, ranging from 0 Molar to 1.0 Molar, is listed below the corresponding micrograph

I(0)   I(0.2)   I(0.4)

I(0.6)   I(0.8)   I(1.0)

(X5000)
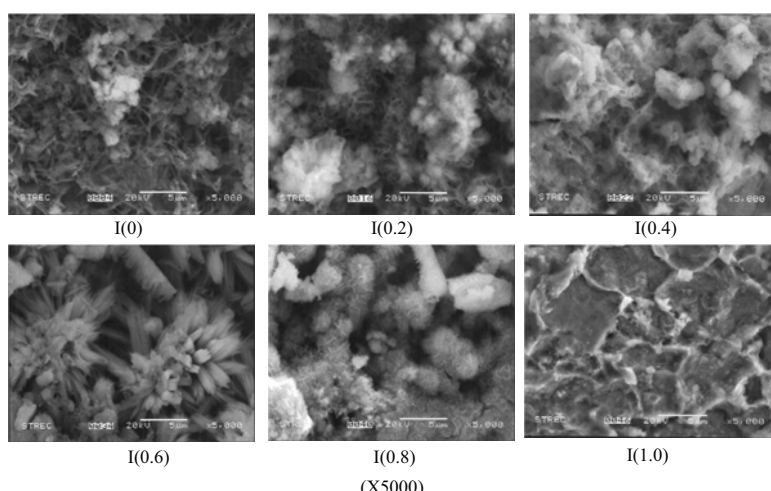
Figure 9. Surface morphology of the 90 day Hg^0 adsorption coupons after lixivient treatment
The concentration of iodine, ranging from 0 Molar to 1.0 Molar, is listed below the corresponding micrograph
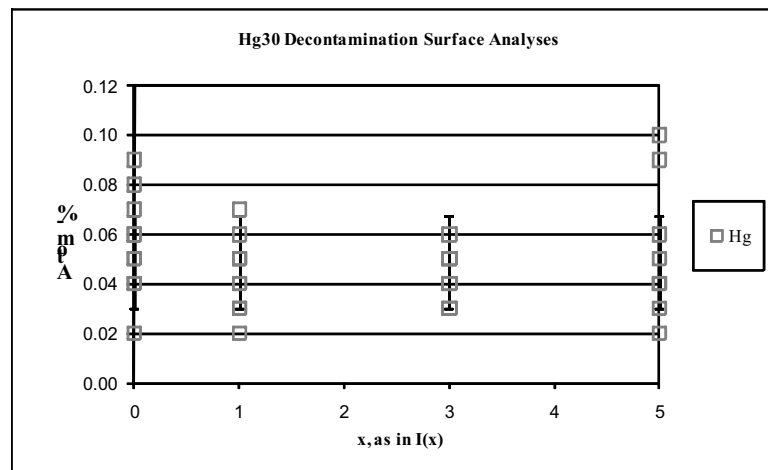
Note I(0) = no iodine, I(1) = 0.2 Molar, I(3) = 0.6 Molar and I(5) = 1.0 Molar

Figure 10. Hg surface concentration by XPS of 30 day Hg adsorption coupons following lixivient treatment with various concentrations of iodine and 2.0 Molar iodide
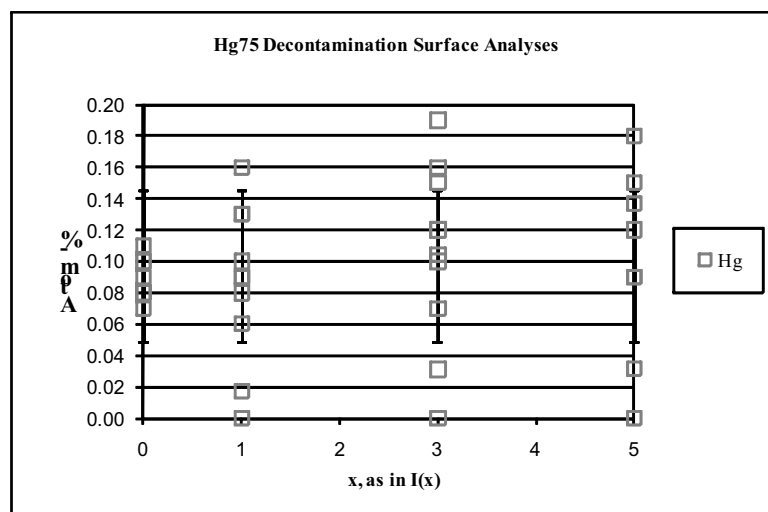
Note I(0) = no iodine, I(1) = 0.2 Molar, I(3) = 0.6 Molar and I(5) = 1.0 Molar

Figure 11. Hg surface concentration by XPS of 75 day Hg adsorption coupons following lixivient treatment with various concentrations of iodine and 2.0 Molar iodide
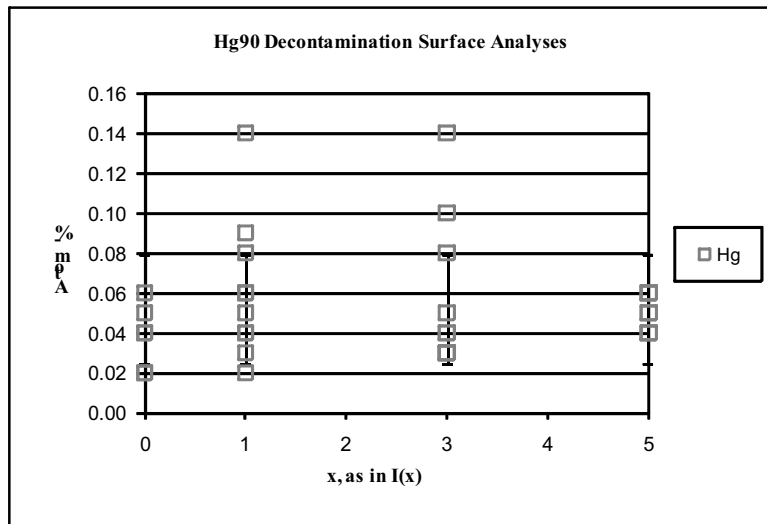
Note I(0) = no iodine, I(1) = 0.2 Molar, I(3) = 0.6 Molar and I(5) = 1.0 Molar

Figure 12. Hg surface concentration by XPS of 90 day Hg adsorption coupons following lixivient

treatment with various concentrations of iodine and 2.0 Molar iodide
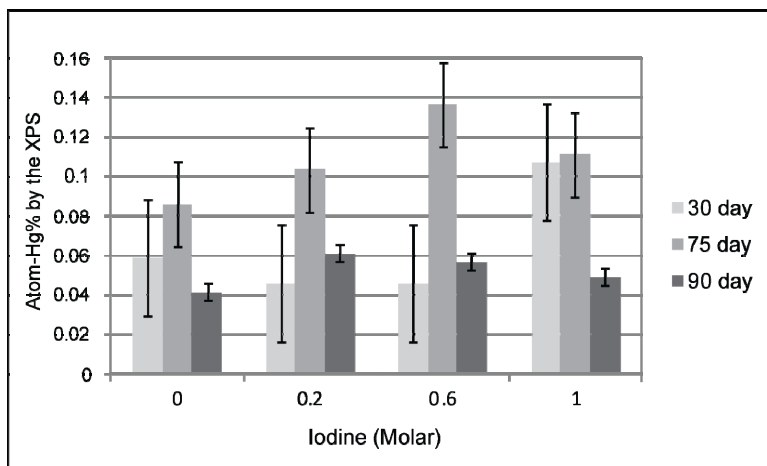
Figure 13. Surface Hg levels in atom% by XPS of steel coupons after the decontamination treatment

Establishment of the Deep-sea Soft Sediments Shearing Strength-Shearing Displacement Model

Hongyun Wu

College of Mechanical and Electrical Engineering

Central South University, Changsha 410083, China

&

Changsha Institute of Mining Research, Changsha 410012, China

Tel: 86-731-88671-485   E-mail: why@cimr.com.cn

Jiangsan He

College of Mechanical and Electrical Engineering, Central South University

Changsha 410083, China

Xinming Chen & Yuqing Gao

Changsha Institute of Mining Research, Changsha 410012, China

Shaojun Liu

College of Mechanical and Electrical Engineering, Central South University

Changsha 410083, China

Abstract

The shearing strength-shearing displacement model of deep-sea soft sediments is very important to predict the traction and slip ratio of nodule collector, and optimize the running mechanism of nodule collector. According to the physical mechanics characters of the deep-sea soft sediments, the 400 sodium molybdate swell soils are selected as the preparation materials of the deep-sea soft sediments, and the demixion preparation method is adopted to simulate the deep-sea soft sediments in the lab, and the shearing test of the rectangle board of 20×50 cm under different grounding pressures is completed in the soil slot. The test result shows that the simulated deep-sea soft sediments have the representative shearing strength-shearing displacement character of brittle soils. Three shearing strength-shearing displacement models of brittle soils are analyzed in the article, and the shearing strength-shearing displacement model being the same with the deep-sea soft sediments based on maximum shearing strength, residual shearing strength, and elastic modules is established, which can offer theoretical support for the structure optimization of running track and the enhancement of the running performance.

Keywords: Deep-sea soft sediments, Shearing strengthen-shearing displacement model, Nodule collector

1. Introduction

Wide deep-sea bed contains abundant mental mines which attract many scientists from various countries and regions to study and finally develop and utilize the sea bed mental mine resources. Based on former investigation and exploitation result, China Ocean Mineral Resources Research and Development Association applied the development region of 150

thousands square kilometers to the National Seabed Authority of China in March of 1991, and at March 5, 1999, completed the confirmation of the mental nodule diggings of 75 thousands kilometers, and established the exploitation technology research plan of multi-mental nodule region, and developed the exploitation technology research of multi-mental nodule region. As the stage research of the multi-mental nodule research plan, the nodule collector (Chen, 2000 & Li, 2001) (made by Changsha Institute of Mining Research) successfully implemented the comprehensive exploitation test on the soft lake bottom of 134m in 2001 (Wang, 2001). In the test, the nodule collector sunk and slid in the original place, which restrained the running performance and passing performance of the nodule collector on the soft lake bottom.

The predict the traction and the slip ratio of the nodule collector on the soft sediments, and enhance its passing performance and running performance, the relationship between the shearing strength and the shearing distortion of soft sediments needs to be known. The function of the rectangle shearing board to shear the soils flatly under normal load is similar with the function of the track vehicles shearing soils, so the level traction of the rectangle shearing board under appointed normal load can be used to establish corresponding shearing strength-shearing displacement model.

Therefore, according to the physical mechanics character of soft sediments in the multi-mental nodule diggings of China, the simulation research of lab deep-sea soft sediments is developed, and the shearing test of simulating deep-sea soft sediments is completed, and the shearing strength-shearing displacement model of soft sediments is established, which can offer theoretical references to predict the traction and the slip ratio of the nodule collector on the soft sediments, optimize the running equipment of the nodule collector and enhance the running performance and the passing performance of the nodule collector.

2. Rectangle board shearing test

2.1 Simulation of deep-sea soft sediments

The physical mechanics characters of deep-sea soft sediments can be describes as follows. The surface presents flow state, and the flow state, fluidal plastic state, and plastic state change with the increase of depth, and the grain class of over 50% surface sediments is 0.004 mm (Song, 1999, P.47-54), and the original position test result of average slip resistance (Gao, 2001, P.425-428) is 1~7.8 kPa in 0~30 cm. Therefore, the 400 sodium molybdate swell soils are adopted as the simulated materials of deep-sea soft sediments to prepare the simulated sediments layer lay layer. The physical mechanics characters of simulated deep-sea soft sediments are seen in Table 1, and their main physical mechanics characters are close to the main physical mechanics characters of deep-sea soft sediments, so they can be used to research the shearing strength-shearing displacement model of soft sediments.

2.2 Test method and equipments

As seen in Figure 1, under the function of balancing weight, the shearing board sinks to certain depth, and after it is stable, the hydraulic ram tows the pull rod and drives the shearing board to shear levelly and stimulate the sediments, and the shearing test of the shearing board is completed. The change of the grounding pressure is implemented by adjusting the amount of balancing weight.

The piston of the hydraulic ram is connected with the sensor by the whorl, and the sensor connects with flange, and the flange connected with the top end of the pull rod by the bolt to ensure that the pull rod keeps vertically in the traction. The down end of the pull rod connects with the suspension link on the former end of the shearing board by the bold to eliminate the level effect of the piston to the shearing board. The measurement data of sensor is the level traction on the shearing board.

The soil slot in the test has the length of 1.8m, the width of 0.8m and the height of 0.6m, and both sides adopt transparent toughened glasses, and in the test, the shearing of simulated sediments can be observed, and the height of the laid simulated sediments is 0.5m.

The rectangle shearing board has the length of 500 mm, the width of 200 mm, and the tooth height of 70 mm which are equidistantly arranged in 4 teeth.

The sensor is the draught-pressure sensor, and the scale is 10KN, and the measurement precision is 0.05%.

The level shearing speed of the rectangle board is the traction speed of the hydraulic ram, i.e. 1cm/s, and the speed keeps constant.

3. Test result and data analysis

After the balancing weight is loaded, the shearing board sinks naturally, and after it is stable, the sediments in front of the shearing board are removed to eliminate the influence of the soil resistance. The length and the width of the removed sediments are equal with the length and the width of the shearing board, and the depth is the sinking quantity after loading and stabilizing of the sharing board. The weights of loading balancing weight respectively are 0kg, 25kg and 40kg, and the grounding pressures respectively are 1.0kPa, 3.5kPa and 5.0kPa, and five times of shearing tests are

made respectively to obtain the average values of the measurement results.

The measurement data obtained in the shearing test indicates the relationship of the traction and the shearing displacement of simulated sediments, and to acquire the relationship between the shearing strength with the shearing displacement, the traction can be converted to the shearing strength of simulated sediments.

$$\tau = \frac{F}{A} = \frac{F}{L(b+2h)} \tag{1}$$

Where, F (N) is the traction, A (cm^2) is the shearing area, L (cm) is the grounding length, h (cm) is the track tooth height, and b (cm) is the grounding width.

To visually obtain the relationship between the change rule of shearing strength with the shearing displacement of sediments, the shearing displacement is the abscissa, and the test data of shearing strength is the longitudinal coordinates, and the relationship curve between the shearing strength and the shearing displacement of sediments under original testing condition is seen in Figure 4, which simulates the curve relationships between the shearing strength measurement average values and the shearing displacement under the grounding pressures of 1.0kPa, 3.5kPa and 5.0kPa.

From Figure 4, the change of the shearing strength of soft sediments is consistent with the change of shearing displacement, i.e. the shearing strength of soft sediments increases quickly with the increase of shearing displacement, and quickly descends when achieving the peak value, and slowly reduces to stable residual shearing strength.

According to Figure 4, under the grounding pressures of 1.1kPa, 3.5kPa and 5.0kPa, the shearing strengths of soft sediments all achieve the peak values (respectively 1.21kPa, 1.46kPa and 1.68kPa), and the corresponding shearing displacement is 3.6cm, and their residual shearing strengths respectively are   0.5kPa, 0.85kPa and 1.1kPa.

4. Shearing strength-shearing displacement model of soft sediments

4.1 Shearing strength-shearing displacement model of brittle soils

In the classic earth pressure theories, two usual representative soils are plastic soils and brittle soils, and both character curves of shearing strength-shearing displacement respectively are seen in the curve A and the curve B in Figure 5. In Figure 5, the curve A is a smooth shearing strength-shearing displacement curve, and the shearing strength slowly achieves to the maximum shearing strength τ_{max} and the change of shearing strength is small, and the whole curve has no obvious "hump". In the curve B, the "hump" of the maximum shearing strength τ_{max} occurs, and it possesses significant stable stage of residual shearing strength after yielding limitation.

In the measurement data curve of Figure 4, the relationship between shearing strength and shearing displacement of soft sediments has representative character of brittle soils.

Aiming at the mechanical character of brittle soils, Bekker (Bekker, 1956), Wong JY (Wong, 1989), Schwarz (E. Schulte, 200, P.121-131) and Sup Hong (Jong-su Choi, 2003, P.139-143) put forward different shearing strength-shearing displacement models.

Bekker's shearing strength-shearing displacement model can be denoted by an equation similar with damp librations.

$$\tau = \frac{(c+\sigma\tan\phi)}{y_{max}} \left\{ \exp\left(-K_2+\sqrt{K_2{}^2-1}\right)K_1 j - \exp\left(-K_2+\sqrt{K_2{}^2-1}\right)K_1 j \right\} \tag{2}$$

Where, j (cm) is the shearing displacement of soils, φ ($^\circ$) is the interior friction angle of soils, K_2 and K_1 are coefficients, y_{max} is the maximum value of the function in the brackets, c (kPa) is the cohesion of soils, and σ (kPa) is the grounding pressure.

Wong JY established the shearing strength-shearing displacement model of soft soils.

$$\tau = \frac{\tau_m}{E}\left[1+(\frac{E}{1-e^{-1}}-1)\,e^{1-j/k_w} \right](1-e^{1-j/k_w}) \tag{3}$$

Where, E is the sensitive coefficient of soils, k_w (cm) is the elastic module, i.e. the corresponding shearing displacement of the maximum shearing strength.

Schwarz et al established the shearing strength-shearing displacement model of swell soils.

$$\tau(s) = \left[\tau_{max}.e^{-b(s-\Delta s)} + \tau_{Re\,st} \right] \times \left[\frac{1}{1+fe^{-ds}} \right] \tag{4}$$

Where, τ_{max}(kPa) is the maximum shearing strength of soils, τ_{rest} (kPa) is the residual shearing strength of soils, b is the fading exponent, Δs (cm) is the displacement offset, f and d are Soil fracture parameters ,which are respectively the

fracture factor and the fracture exponent.

Sup Hong established the shearing strength-shearing displacement model of swell similar with Huang ZY's model.

4.2 Establishment of soft sediments shearing-strength-shearing displacement model

Bekker's model and Wong's model mainly aim at the soils of earth, and they may not suit for the soft sediments with flow surface and high water content. Bekker's model is complex and the computation is fussy. Wong's model defines the relationship between the maxim shearing strength and the residual shearing strength as the sensitive coefficient of soils, which is too qualitative. Schwar's model firstly introduces the residual shearing strength, and adopt the attenuation index, the destroying coefficient, and the destroying index to represent the influences of the track structure parameters, but the whole model with more parameters and influencing factors is too complex.

According to Figure 4, the shearing strength of soft sediments quickly increases with the increase of shearing displacement, and different peak values can not be achieved at same shearing displacement, and the shearing strength quickly descends to corresponding stable value of residual shearing strength. In this way, the shearing stress of soft sediments is related with the maximum shearing strength, the residual shearing strength and the shearing elastic module, but they are independent each other. Therefore, it is not difficult to establish the shearing strength-shearing displacement model of soft sediments which takes the maximum shearing stress, the residual shearing strength, and the shearing elastic module as the characters of inflexion, and takes e^{1-j/k_m} and e^{-j/k_m} as the change characters. The concrete relationship is seen in the formula as follows.

$$\tau(j) = \left[\tau_{\max}.e^{1-j/k_m}.e/(e-1) + \tau_{\mathrm{Re}\,st}.\left(1 - e^{1-j/k_m}\right)\right]\left(1 - e^{-j/k_m}\right) \tag{5}$$

Where, k_m (cm) is the corresponding shearing displacement of the maximum shearing strength.

The advantage of this model is that only the measurement values of parameters including the maximum shearing strength, the residual shearing strength, and the shearing elastic module of the shearing board in the shearing test with appointed grounding pressure are confirmed, the corresponding shearing strength-shearing displacement model can be established, and the shearing strength-shearing displacement model of soft sediments can be simplified largely.

According to the measurement data in Figure 4, under the grounding pressures of 1.1kPa, 3.5kPa and 5.0kPa, the relationships between the shearing strength and the shearing displacement of soft sediments respectively are

$$\tau(j) = \left[1.04 \times \left(1 - e^{1-j/3.6}\right) + 0.5\right]\left(1 - e^{-j/3.6}\right) \tag{6}$$

$$\tau(j) = \left[1.38 \times \left(1 - e^{1-j/3.6}\right) + 0.85\right]\left(1 - e^{-j/3.6}\right) \tag{7}$$

$$\tau(j) = \left[1.49 \times \left(1 - e^{1-j/3.6}\right) + 1.1\right]\left(1 - e^{-j/3.6}\right) \tag{8}$$

The formula (6), the formula (7) and the formula (8) are simplified largely comparing with the formula (5), which can help to predict, analyze and solve the tractions of vehicle.

4.3 Validation of model

To validate the correctness of the model, the measurement data of shearing strength-shearing displacement under the grounding pressures of 1.0kPa, 3.5kPa and 5.0kPa are fitted by the formula (5), and the fitting result is seen in Figure 6, and relative coefficients respectively are 0.76, 0.78 and 0.75, which indicates that the model accords with the change rule of shearing strength of soft sediments with the change of shearing displacement.

5. Conclusions

(1) The soft sediments have representative characters about shearing strength and shearing displacement of brittle soils, i.e. the shearing strength of soft sediments quickly increases with the increase of shearing displacement, and different peak values can not be achieved at same shearing displacement, and the shearing strength quickly descends to corresponding stable value of residual shearing strength.

(2) According to the measurement values of parameters including the maximum shearing strength, the residual shearing strength, and the shearing elastic module of the shearing board in the shearing test with appointed grounding pressure, the corresponding shearing strength-shearing displacement model can be established as follows.

$$\tau(j) = \left[\tau_{\max}.e^{1-j/k_m}.e/(e-1) + \tau_{\mathrm{Re}\,st}.\left(1 - e^{1-j/k_m}\right)\right]\left(1 - e^{-j/k_m}\right)$$

(3) The fitting result of the shearing strength-shearing displacement model indicates that this model can be applied for the prediction and solving of the traction of the nodule collector on deep-sea soft sediments.

References

Bekker, MG. (1956). *Theory of Land Locomotion.* The University of Michigan Press, Library of Congress Card Number 56-10101.

Chen, Xinming. (2000). *Technology design of the pilot mining seabed tracked vehicle.* Changsha: Changsha Institute of Mining Research.

E. Schulte, R. Handschuh, W. Schwarz. (2003). *Transferability of Soil Mechanical Parameters to Traction Potential Calculation of a Tracked Vehicle*. The Proceedings of the Fifth ISOPE Ocean Mining Symposium. Tsukuba, Japan. P.121-131.

Gao, Yuqing. (2001). *Research and development of in-situ test system of the characteristics of physical mechanics of seabed soft sediments*. Conference on China ocean Resource Research and Development Association. Beijing: COMRA. P.425-428.

Jong-su Choi, Sup Hong & Hyuang-Woo Kim. (2003). *An Experimental Study on Tractive Performance of Tracked Vehicle on Cohesive Soft Soil.* The Proceedings of the Fifth ISOPE Ocean Mining Symposium. Tsukuba, Japan. P.139-143.

Li, Li. (2001). *Development of self-propelled seabed tracked vehicle.* Changsha: Changsha Institute of Mining Research.

Song, Lianqing. (1999). *The physical properties of surface sediments in oceanic polymetallic nodule*. Acta Oceanologica Sinica. No.6(21). P.47-54.

Wang, MH. (2001). *Research Report of Lake Test of the Pilot-testing Mining System.* China ocean Resource Research and Development Association (COMR R&D). P.71-72.

Wong, JY. (1989). *Terramechanics and Off-Road Vehicles*, Elsevier Science Publishers B. V., Amsterdam.

Wu, Hongyun, Chen Xinming & Gao Yuqing. (2006). T*he New Principle of In-situ Testing Shearing Strength of Marine Sediment*. Mining and Processing Equipment. No.12. P.16-17.

Table 1. Physical mechanics characters of simulating deep-sea soft sediments

Depth (cm)	Water ratio W (%)	Soil particle density ρ_s (kN/m^2)	Natural density P (kN/m^2)	Slip resistance (kPa) (Wu, 2006, P.16-17)
0~10	101.8	12.6	10.9	1.3
10~20	98.1	12.1	10.9	4.2
20~30	81.3	11.4	10.9	7.6
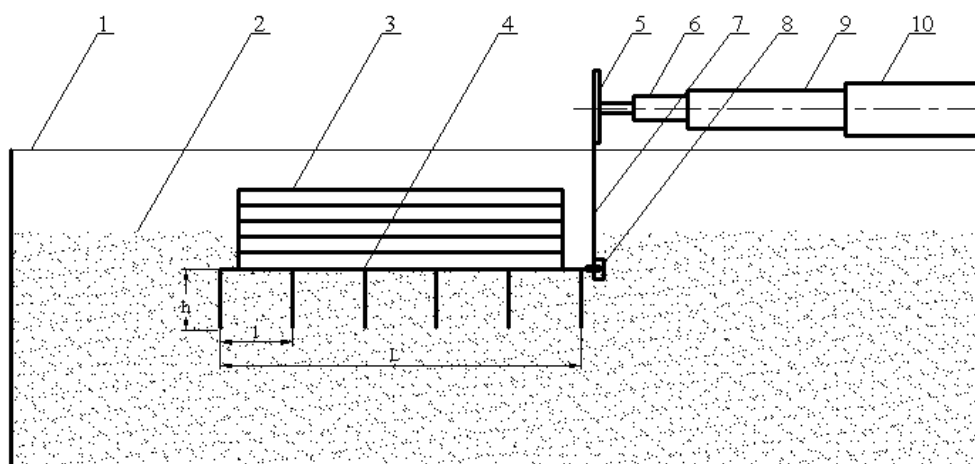
Figure 1. Principle Chart of Shearing Test (1-soil slot, 2-simulated sediments, 3-balancing weight, 4-shearing board, 5-flange, 6-sensor, 7-pull rod, 8-suspension link, 10-hydraulic ram)
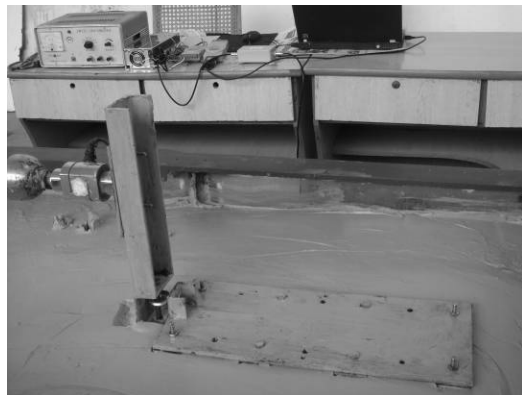
Figure 2. Practical Principle Chart of Shearing Test
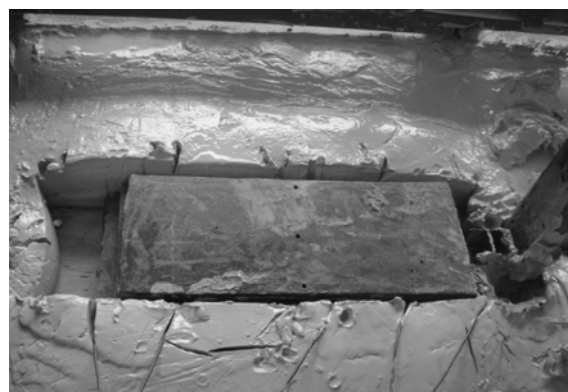
Figure 3. Loading Shearing Test
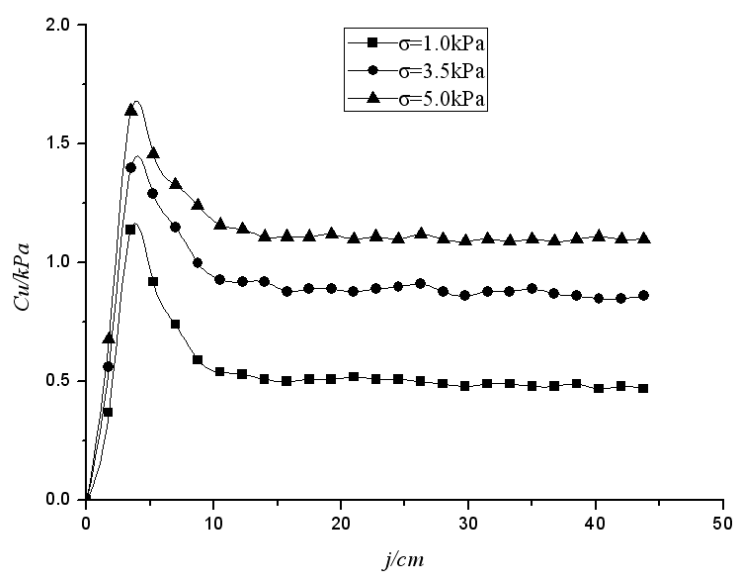
Figure 4. Shearing Test Curve of 50×20 cm Shearing Board
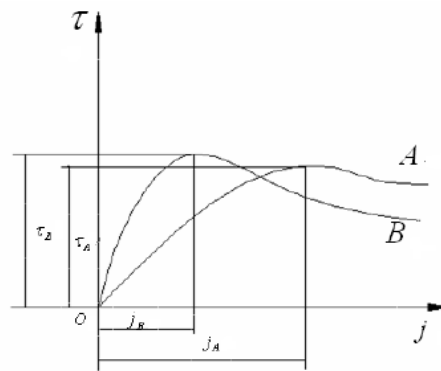
Figure 5. Shearing Strength-Shearing Displacement Curve of Representative Soils
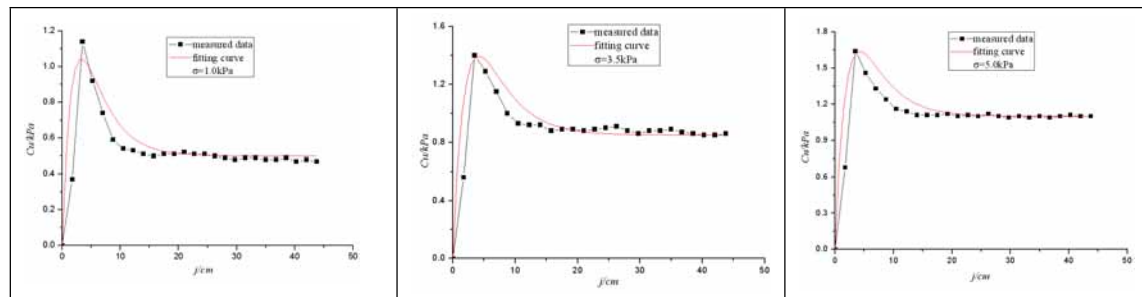
Figure 6. Curve Fitting Validation of Shearing Strength-Shearing Displacement Measurement Data

Analysis of Design Optimization of Bandwidth and Loss Performance of Reflectarray Antennas Based on Material Properties

M.Y. Ismail & M. Inam

Radio Communications and Antenna Design Laboratory

Department of Communication Engineering

Faculty of Electrical & Electronics Engineering

Universiti Tun Hussein Onn Malaysia

86400 Parit Raja, Johor, Malaysia

E-mail: yusofi@uthm.edu.my, muhammad_inamabbasi@yahoo.com

Abstract

An investigation for the enhancement strategy of bandwidth performance and analysis of different types of losses associated with reflectarray antennas is presented in this paper. Studies are carried out using different commercially available dielectric materials with dielectric permittivity (ε_r) values ranging from 2.08 to 13 and loss tangent (tanδ) ranging from 0.0003 to 0.025. The performance of different dielectric materials for the design of infinite reflectarray is analyzed in terms of bandwidth, reflection loss and Figure of Merit (FOM). Bandwidth of patch element unit cell at different levels are observed and it has been shown that 10% bandwidth varies from 84 MHz to 360MHz and 20% bandwidth varies from 126 MHz to 540MHz based on the selection of dielectric substrate for reflectarray antenna design. Moreover it has been demonstrated that the reflection loss of the reflectarray antenna can be factorized into dielectric loss and conductor loss which depends on the material properties employed for the design.

Keywords: Reflectarray, Bandwidth, Dielectric loss, Conductor loss, Figure of merit

1. Introduction

Antennas with high gain performance are the required for some of the applications in communication systems. The conventional high-gain antennas most often used are parabolic reflectors. Although they are efficient radiators, parabolic reflectors are too large and heavy, due to their curved reflecting surfaces. As a result, a planar reflector called a microstrip reflectarray was being proposed as a future candidate high-gain antenna (J.Huang, February 15, 1995). It consists of an array of microstrip patches on the grounded dielectric substrate and is illuminated by a primary feed horn which is placed at a particular distance from the array whose individual elements are designed to scatter the incident field with proper phase distribution required to form a planar phase surface in front of the aperture (David M. Pozar, D. Targoski and H.D. Syrigos, February 1997). The reflectarray antenna can achieve a very high efficiency for a very large aperture and it can also be designed to tilt a large angle (John Huang and Jose Encinar, 2007). Despite of the advantage of the size, cost and easy deployability, the major deficiency of the reflectarray that limits its usage is the low bandwidth performance (M.E.Biallowski and Jose Encinar, 2007). The main factors that limit the bandwidth of reflectarray antenna are the narrow bandwidth of patch elements which is caused by the extended path length between the feed horn and the reflectarray, and the phase errors related to the change in patch size (K.Y.SZE and L. Shafal, *1998*). The feed antenna bandwidth and array element spacing also limits the bandwidth of reflectarrays but these two are not serious concerns if the bandwidth requirement is les than 15% (J.Huang, February 15, 1995). Another important factor, that affects the bandwidth of the reflectarray antenna and has not been discussed in the past thoroughly, is the selection of suitable dielectric material. The effect of properties of dielectric material, used as a substrate for the reflectarray antenna, on the bandwidth and reflection loss performance is discussed in this work.

2. Distinction of different types of losses in reflectarray antennas

Generally the reflection loss of the reflectarray antennas is primarily limited to dielectric absorption in the dielectric layer and conductor loss (M.Y.Ismail and M.Inam, *2009*). The reflection loss of reflectarray antenna depends on the material properties of the dielectric material which includes the substrate thickness, and the conducting material used for the patch element and the ground plane as given in equation (1).

$$R_l = \alpha_d + \alpha_c \qquad (1)$$

Where, R_l is the reflection loss and α_d and α_c represent the attenuation factor due to dielectric and conductor loss and can be calculated using equation (2) and equation (3) respectively which are given in the numerical analysis section. The dielectric loss occurs due to the strong electric fields in the substrate region and copper loss occurs due to high current generated on the top surface of the patch element (Harish Rajagopalan and Yahya Rahmat Samii, *April 2008*). The electric field distribution and the surface currents are highest at resonance which is the reason of the highest loss at the resonant frequency. For further investigation of the loss mechanism in a reflectarray antenna, an infinite reflectarray with 0.035mm patch element thickness and 1mm substrate thickness using commercially available CST computer model is designed. Different dielectric materials are used and the dielectric loss is observed by reducing the conductor loss to minimum (or ideally zero by using PEC for patch element and ground plane). Copper with a conductivity of 59.6Ms/m is used for the design of patch element and the ground plane in order to introduce the conductor loss in the reflectarray antenna design. Copper loss or the conductor loss is observed separately by defining the loss tangent values of the dielectric substrate to be zero and hence making the factor due to dielectric loss to be zero. The losses calculated for different dielectric materials are shown in Table 1. It can be observed from the table that the materials with high loss tangent values, such as CEM and Gallium Arsenide have very high reflection loss and the main contributor for this high reflection loss is dielectric loss. This is because these materials exhibit high dielectric absorption in the dielectric layer of the reflectarray antennas. On the other hand materials with low loss tangent values such as Teflon and Alumina have relatively very low reflection loss. This is due to low dielectric loss properties and the dominant loss for this type of reflectarray antenna design is caused by conductor/copper loss. The factorization of the reflection loss for two materials is shown in Figure 1 and Figure 2 for comparison. As shown in Figure 1 and Figure 2, it can be observed that Teflon which has a low loss tangent value (tanδ=0.0004) has very low dielectric loss and Gallium Arsenide which has a high loss tangent value (tanδ=0.006) offers a very high dielectric loss as compared to the copper loss.

3. Bandwidth performance of reflectarrays using different materials

The materials listed in Table 1 are used to design infinite reflectarrays resonating at 10GHz and the 10% and 20% bandwidth is measured by moving 10% and 20% above the reflection loss at 10 GHz. The bandwidth calculated in this work for different materials are presented in Figure 3. As depicted in Figure 3, it can be seen that as the dielectric permittivity of the material used for the reflectarray design is increased, the bandwidth decreases. Gallium Arsenide, which has the highest dielectric permittivity (ε_r=13) has the minimum 10% and 20% bandwidths of 84 MHz and 126 MHz respectively while Teflon which has the lowest dielectric permittivity (ε_r =2.08) has the highest 10% and 20% bandwidths of 360 MHz and 540 MHz respectively. These results can be validated according to equation (4) and can be associated with the material properties of these dielectric materials.

4. Analysis of reflection phases of different materials

The reflection phases of all the designed reflectarrays are also analyzed and it is shown that the materials with low dielectric permittivity, when used for reflectarray antenna design, show gentler slope in reflection phase curve as compared to the high dielectric constant materials. This can also be validated using equation (4), which shows that as the dielectric permittivity of the material is increased, the bandwidth decreases and hence causes a steeper slope in the reflection phase curve. The reflection phase of the patch element unit cell with Teflon and CEM dielectric materials has been observed using different thicknesses of substrate. As shown in Figure 4 and Figure 5, the results demonstrate that a gentler phase curve is generated as the substrate thickness is increased from 1.0mm to 2.0mm. Figure of Merit (FOM) has been defined in order to predict the performance of the linear phase range within a particular frequency range based on reflection phase curves of different materials. The figure of merit (FOM) can be defined as the ratio of the change in reflection phase to the change in the frequency and it can be expressed as by (M.Y.Ismail and M.Inam, *2009*).

$$FOM = \frac{\Delta \phi}{\Delta f} \qquad °/ \text{MHz}$$

Where $\Delta\Phi$ is the change in the reflection phase in degrees and Δf is the change in the resonant frequency in MHz of the reflectarray antenna and FOM is calculated here in °/MHz. It has been observed that the FOM increases with the increase in dielectric permittivity. This is because increasing the permittivity causes the reflection phase to get steeper and hence causes $\Delta\Phi$ to increase over the same range of frequencies which increases FOM as shown in Figure 6.

5. Numerical analysis and bandwidth performance

Theoretical equations have been used to perform the numerical analysis of reflectarray and validate the results obtained from CST simulations. This section includes the discussion on the theoretical basis of quantification of different types of losses and provides numerical equations for the prediction of bandwidth performance in the reflectarray. As depicted in equation (1), the total reflection loss of a reflectarray is the sum of dielectric and conductor loss. The attenuation due to dielectric material can be given by the following formula (Balanis. Constantine A. 2005).

$$\alpha_d = \frac{\omega}{2} \sqrt{(\mu_0 \varepsilon_0 \varepsilon_r)} \tan \delta \tag{2}$$

Where

$$\omega = 2\pi f_r$$

$$\tan \delta = \frac{\varepsilon''_r}{\varepsilon'_r}$$

$$\varepsilon_r = \varepsilon'_r - i\varepsilon''_r$$

In order to improve the accuracy of the calculation of attenuation factor due to dielectric, relative permittivity can be used which is given by:

$$\varepsilon_{reff} = \frac{\varepsilon_r + 1}{2} + \frac{\varepsilon_r - 1}{2}\left[1 + 12\frac{H}{W}\right]^{-1/2}$$

Also the conductivity of the dielectric material can be defined in terms of tanδ as:

$$\sigma_d = \omega \varepsilon_r \tan \delta$$

So using ε_{reff} and σ_d, the equation for the attenuation constant becomes:

$$\alpha_d = 4.34 \frac{1}{\sqrt{\varepsilon_{reff}}}\left(\frac{\varepsilon_{reff} - 1}{\varepsilon_r - 1}\right)\sqrt{\frac{\mu_0}{\varepsilon_0}}\sigma_d \, (dB/cm)$$

The above equation is appropriate for the substrates with higher loss tangent values.

Similarly the attenuation due to the conductor can be simplified as:

$$\alpha_c = \frac{8.68 R_s}{W Z_m} (dB/cm)$$

Where R_s is the surface resistivity and is given by

$$R_s = \sqrt{\frac{\omega \mu_0}{2\sigma_c}}$$

$$\alpha_c = \frac{8.68}{W Z_m}\sqrt{\frac{\omega \mu_0}{2\sigma_c}} (dB/cm) \tag{3}$$

Using α_c and α_d, the reflection loss of reflectarray can be calculated using equation (1) and hence VSWR. The bandwidth of a microstrip antenna or the reflectarray is related to the VSWR and Quality factor by the following relation (Balanis. Constantine A. 2005):

$$\frac{\Delta f}{f_0} = \frac{VSWR - 1}{Q_t \sqrt{VSWR}} \tag{4}$$

Where Δf is the bandwidth of the antenna and f_o is the resonant frequency of design. Q_t, the total quality factor is given by the sum of the quality factor by various losses.

$$\frac{1}{Q_t} = \frac{1}{Q_d} + \frac{1}{Q_c} + \frac{1}{Q_r} + \frac{1}{Q_{sur}} \tag{5}$$

In equation (5), Q_d, Q_c, Q_r, Q_{sur} are the quality factors for dielectric, copper, radiation and surface loss respectively and Quality factor for each type of loss can be obtained using general relation as:

$$Q = \frac{\omega_r W_t}{P_L}$$

Where P_L is the power loss of different factors and W_t is the energy stored at the resonant which is the same independent of the mechanism of loss and is given by:

$$W_t = \frac{1}{4} \varepsilon_0 \varepsilon_r h L W$$

Q_{sur} can be neglected for thinner substrates and the quality factor for dielectric, conductor and radiation can be calculated by:

$$Q_d = \frac{1}{\tan \delta}$$

$$Q_c = h \sqrt{\pi f_r \mu_0 \sigma_c}$$

$$Q_{rad} = \frac{2 \omega \varepsilon_r k}{h G_{t/l}}$$

Where $G_{t/l}$ is the total conductance per unit length and for rectangular aperture:

$$G_{t/l} = \frac{G_{rad}}{W}$$

$$k = \frac{L}{4}$$

G_{rad} (radiation conductance) can be found out by:

$$G_{rad} = \frac{1}{90} \left(\frac{\omega}{\lambda} \right)^2 ; \omega \ll \lambda$$

$$G_{rad} = \frac{1}{120} \left(\frac{\omega}{\lambda} \right) ; \omega \gg \lambda$$

Using the relations for the different quality factors, we can find the total quality factor by equation (5) and hence bandwidth of reflectarray using equation (4).

6. Conclusion

Infinite rectangular microstrip reflectarray antennas with different dielectric materials are analyzed in terms of bandwidth and reflection loss performance and it has been shown that the bandwidth of the reflectarray antenna can be increased by using a suitable dielectric material. It has been shown that Teflon (ε_r=2.08 and tanδ=0.0004) has maximum bandwidth performance compared to Gallium Arsenide (ε_r=2.08 and tanδ=0.0004) which has minimum value of the bandwidth measured at different levels of the reflection loss curve.   Different factors of the reflection loss are shown separately which permits the optimization of loss performance of the reflectarrays. Further investigations are required to utilize the material properties in order to enhance the performance of the reflectarray antennas.

References

Balanis. Constantine A. (2005). *Antenna Theory: Analysis and Design*. USA: John Wiley & Sons, Inc.

David M. Pozar, D. Targoski and H.D. Syrigos. (February, 1997). Design of millimeter wave microstrip reflectarrays. *IEEE Transactions on Antennas propogation, vol. 45*.

Harish Rajagopalan and Yahya Rahmat Samii. (April, 2008). Dielectric and Conductor Loss Quantification for Micro Strip Reflectarrays: Simulation and Measurements. *IEEE Transactions on Antenna and Propogation, Vol56, no 4*.

J.Huang. (February 15, 1995). Analysis of microstrip reflectarray antenna for microspacecraft applications. *Spacecraft Telecommunications Equipment section, TDA Progress report 42-12*.

John Huang and Jose Encinar. (2007). *Reflectarray Antennas*. Wiley, interscience.

K.Y.SZE and L. Shafal. (1998). Analysis of phase variation due to varying patch length in a microstrip reflectarray. *IEEE*.

M.E.Biallowski and Jose Encinar. (2007). Reflectarray: Potential and challenges. *IEEE*.

M.Y.Ismail and M.Inam. (2009). Numerical analysis and equivalent circuit modeling for loss quantification of reflectarrays using different substrate materials. *IEEE International Conference on Antennas, Propagation and Systems (INAS 2009) Johor, Malaysia*.

Table 1. Combined, dielectric and conductor loss for different materials

| Dielectric Material	Dielectric Constant	Loss tangent	Conductivity of conductor (Copper)	Combined Loss R_l	Dielectric Loss α_d	Conductor Loss α_c
(ε_r)		(Tanδ)	σ (Ms/m)	(dB)	(dB)	(dB)
Alumina (95%)	9.75	0.0003	59.6 Ms/m	0.519 dB	0.148 dB	0.370 dB
Beryllia	6.5	0.0004	59.6 Ms/m	0.395 dB	0.138 dB	0.257 dB
CEM	4.5	0.025	59.6 Ms/m	6.875 dB	6.656 dB	0.187 dB
Gallium Arsenide	13	0.006	59.6 Ms/m	4.326 dB	3.831 dB	0.455 dB
Roger 5870	2.33	0.0012	59.6 Ms/m	0.313 dB	0.189 dB	0.122 dB
Roger 5880	2.2	0.0004	59.6 Ms/m	0.178 dB	0.060 dB	0.118 dB
Silicon	11.9	0.004	59.6 Ms/m	2.857 dB	2.406 dB	0.444 dB
Teflon	2.08	0.0004	59.6 Ms/m	0.183 dB	0.063 dB	0.119 dB
Vaseline	2.16	0.001	59.6 Ms/m	0.261 dB	0.146 dB	0.114 dB
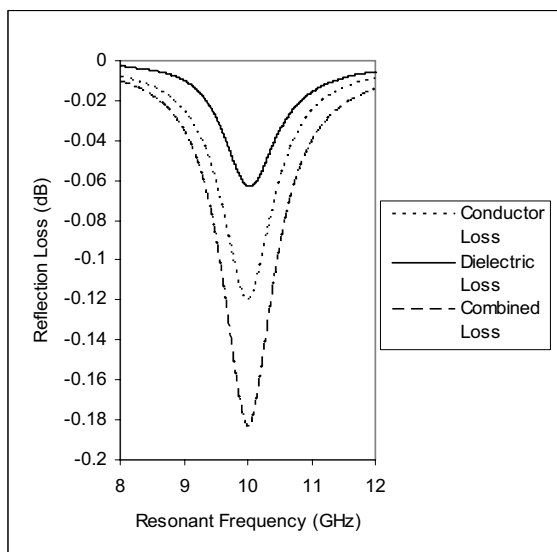
Figure 1. Individual and combined loss for Teflon
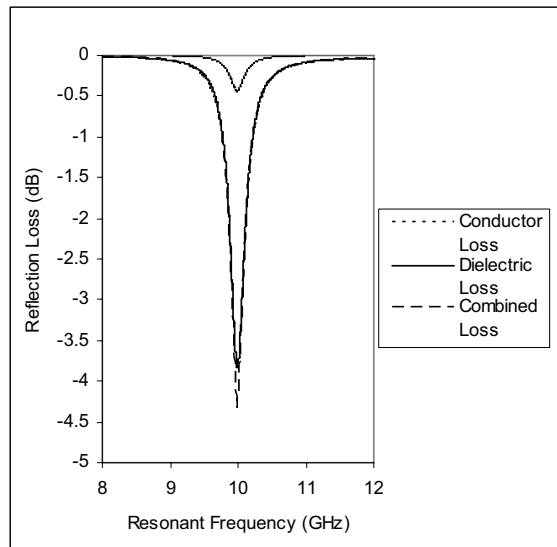
Figure 1. Individual and combined loss for Gallium Arsenide
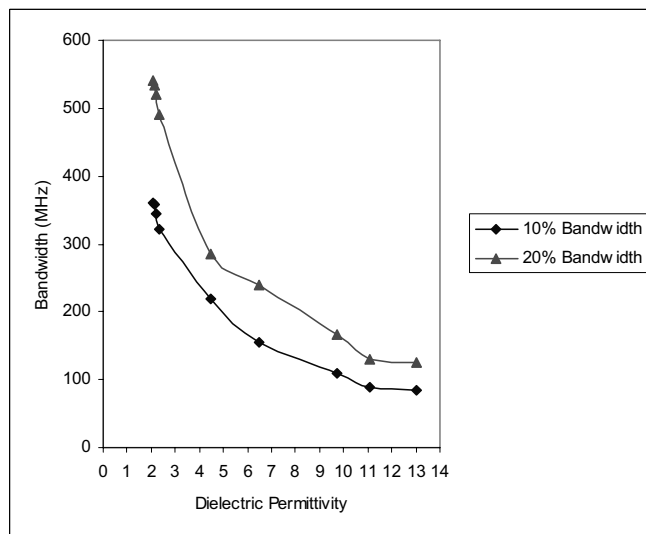
Figure 2. Trend of bandwidth performance
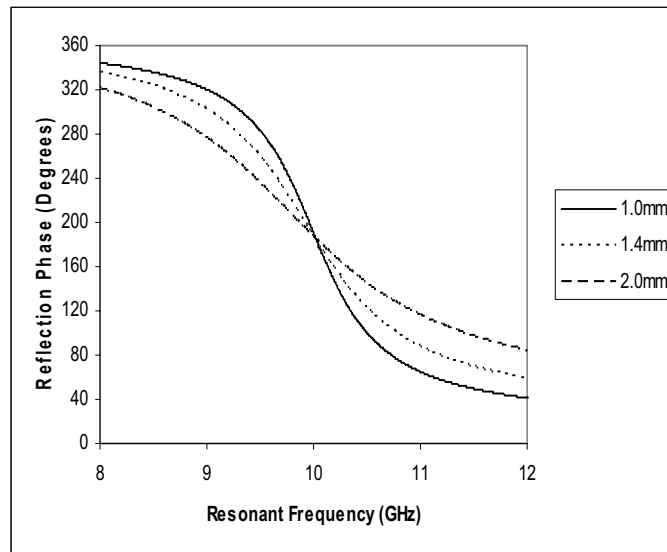
Figure 4. Reflection phase of Teflon with different substrate thicknesses
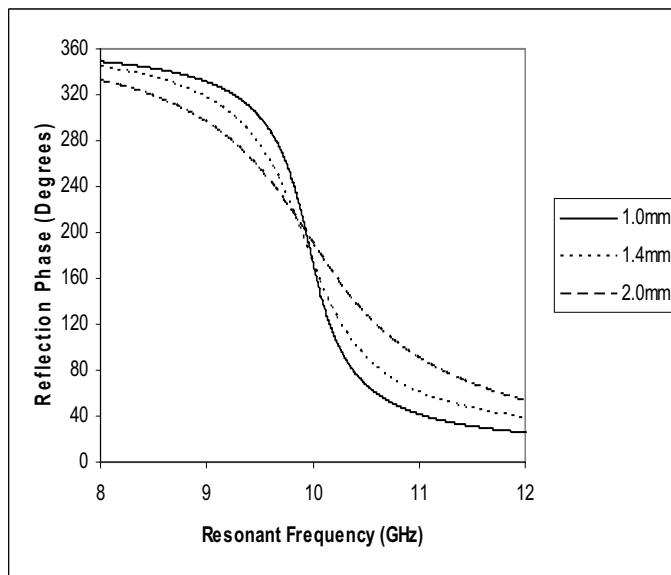
Figure 5. Reflection phase of CEM with different substrate thicknesses
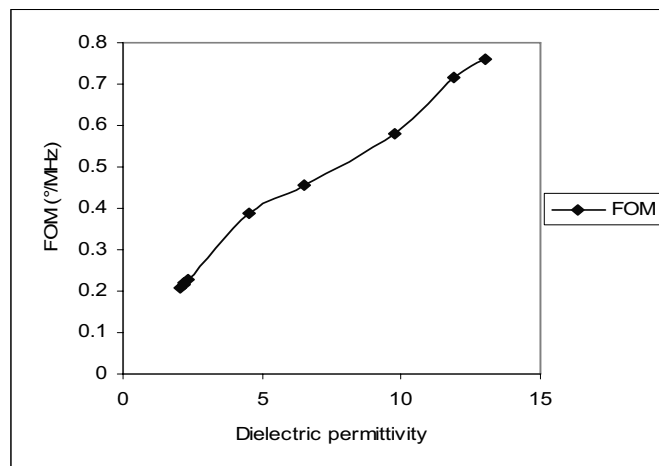
Figure 6. Trend of FOM with increasing Dielectric Permittivity

Chessboard Coverage Teaching Based on Divide-and-Conquer Algorithm

Zhijie Li

Institute of Nonlinear Information Technology, Dalian Nationalities University

Dalian 116600, China

E-mail: lizhijie@dlnu.edu.cn

Feixue Huang

Department of Economics, Dalian University of Technology

Dalian 116024, China

Xiangdong Liu & Xiaodong Duan

Institute of Nonlinear Information Technology, Dalian Nationalities University

Dalian 116600, China

Abstract

Though the divide-and-conquer algorithm is a powerful technology, but it is difficult to be used in practice, so the design of this algorithm should be regulated in the teaching. In this article, the teaching process and the characters of the divide-and-conquer algorithm are studied when solving the problem of chessboard coverage. Aiming at the deficiency that the existing teaching method uses skills in decomposing sub-problems and increases the teaching difficulty, the coverage sequence of L-type dominoes is improved. The improved algorithm can keep consistent with the divide-and-conquer strategy and standardize the iterative process, and increase the normative character and the consistence of the algorithm, and hence achieve ideal teaching result.

Keywords: Algorithm, Divide-and-conquer, Chessboard coverage

1. Introduction

Algorithm design and analysis (Cormen TH, 2001 & Wang, 2005, P.124-127 & Goodrich MT, 2007 & Wang, 2007) is the comprehensive lesson integrating the application, creation, and practice. To solve problem by the algorithm, the practice problem should be firstly abstracted as the mathematical model, and then the algorithm corresponding to this model is designed. These approaches are an organic integer, and the algorithm design is the core content in them, the key approach from proposing problem to solving problem. In the teaching process, proper method should be adopted to make students grasp the basic theory and technology of the algorithm. The standardization of the algorithm design is the important factor to influence students' understandings about the algorithm ideas. This article mainly studies the algorithm design of the divide-and-conquer algorithm solving the problem of chessboard coverage, and explores the standardization of the algorithm design.

The computation time needed by any one problem which can be solved by computer is related with the scale of the problem. The scale of the problem is smaller, the needed computation time is always less, and the computation is easier. The deign idea of the divide-and-conquer algorithm (Stephen RM, 2004, P. 420-425 & Shimojoa F, 2005, 151-164 & Min F, 2005, P. 1277-1286 & Huang, 2008, 1831-1839 & Wu YZ, 2008, P. 41-44) is to divide a complex big problem into many small problems and conquer them one by one. The concrete approaches are to divide the big problem which is difficult to be solved directly into two or more same or similar sub-problems, and divide the sub-problems into smaller sub-problems until these sub-problems can be directly solved simply, and the solution of the original problem is the combination of the solutions of all sub-problems. One main implementation mode of this approach in super language is the recursion. Therefore, the divide-and-conquer is a kind of important algorithm, and its approaches seem simply, but contain profound philosophical ideas, and this skill is the base of many high-efficiency algorithms.

One representative application of the divide-and-conquer is to solve the chessboard coverage problem (Ohio C, 2007, P.464-469). In the teaching process nowadays, the solving of the algorithm is excessively to pursue the skill, which induces that the algorithm flow is not consistent with the divide-and-conquer idea. Though the correctness of the algorithm is not influenced, but it brings negative influences for students to understand the problem and the divide-and-conquer algorithm. Therefore, the process of the divide-and-conquer algorithm to solving the chessboard coverage problem is mainly discussed in the article, and the standardization and consistence of the solving algorithm are improved for obtaining better teaching effect.

2. Divide-and-conquer algorithm

2.1 Basic ideas

For the problem with the scale of n, if n is small, the problem can be solved directly, or else, the problem can be divided into *k* sub-problems with small scale, and $1 < k \leq n$, and these sub-problems all can be solved, and are independent each other and have same form with the original problem. Solve the sub-problems recursively, and combine the solutions of various sub-problems, so the solution of the original problem is obtained. This strategy of algorithm design is called as the divide-and-conquer method. The sub-problem generated in the divide-and-conquer algorithm is always the smaller mode of the original problem, which offers the convenience to use the recursion technology. Under this situation, by repetitively using the measure of divide-and-conquer, the type of the sub-problems can be consistent with the original problem, but the scale continually reduced until the sub-problem can be easily and directly solved. So the recursion process is generated naturally. The application of the divide-and-conquer algorithm and the recursion in the algorithm design can generate higher efficiency. The problems which can be solved by the divide-and-conquer algorithm generally have following characters.

(1) When the scale of the problem is reduced to certain extent, it can be easily solved.

(2) The problem can be divided into many same problems with small scale, i.e. the problem has the character of the optimal sub-structure.

(3) The solutions of the sub-problems of the problem can be combined as the solution of the problem.

(4) Various sub-problems divided by this problem are independent each other, i.e. the public problem is not contained among sub-problems.

2.2 Solving approaches

On each level of recursion, the divide-and-conquer algorithm has three approaches. First, the original problem is divided into many sub-problems with small scale which are independent each other, and have same form with the original problem. Second, if these sub-problems have small scale and can be easily solved, directly solve them, or else, recursively solve various sub-problems. Finally, combine the solutions of various sub-problems as the solution of the original problem. The general algorithm design mode can be described as follows.

divide-and-conquer(P)

{

   if (|P|<=n0) adhoc(P);

   divide P into smaller subinstances P1 ,P2 ,...,Pk;

   for (i=1; i<=k; i++)

     yi = divide-and-conquer(Pi);

   return merge(y1,y2,...,yk)

}

Where, |P| denotes the scale of the problem P, n_0 is one threshold value which denotes that the problem can be solved easily and directly and the problem needs not be further divided when the scale of the problem P doesn't exceed n_0, adhoc (P) is the basic sub-algorithm in the divide-and-conquer algorithm which can be used to directly solve the problem P with small scale. So when the scale of P doesn't exceed n_0, it can be directly solved by the algorithm adhoc (P). The algorithm of merge $(y_1,y_2,...,y_k)$ is the combining sub-algorithm in the divide-and-conquer algorithm which is used to combine the corresponding solutions $y_1,y_2,...,y_k$ of the sub-problems $P_1 ,P_2 ,...,P_k$ into the solution of P. According to the division principle of the divide-and-conquer algorithm, when designing the algorithm by the divide-and-conquer algorithm, the scales of sub-problems should be approximately same. In another word, the processing method dividing one problem into *k* sub-problems with same scale is feasible. This method is based on the balance of sub-problems.

3. Divide-and-conquer strategy of the chessboard coverage problem

3.1 Problem denotation in teaching

In the chessboard composed by $2^k \times 2^k$ panes, if there is one pane which is different with other panes, this pane is called as the special pane, and this chessboard is called as the special chessboard. Obviously, the positions that the special pane occurs in the chessboard include 4^k sorts. For any $k \geq 0$, there are 4^k sorts of different special chessboard. The special chessboard in Figure 1 is one of 16 special chessboard when $k = 2$.

In the problem of chessboard coverage, 4 kinds of L-type dominos with different forms seen in Figure 2 should cover all panes except for special panes in the appointed special chessboard, and any two L-type dominos can not be covered repetitively. Obviously, in any one chessboard coverage of $2^k \times 2^k$, the amount of used L-type dominos is just $(4^k-1)/3$.

A simple algorithm about the chessboard coverage problem can be designed by the divide-and-conquer strategy. When $k > 0$, divide the chessboard of $2^k \times 2^k$ into 4 sub-chessboards of $2^{k-1} \times 2^{k-1}$ (seen in Figure 3(a)). The special pane must be located in the small one of four sub-chessboards, and other three sub-chessboards have no special panes. To convert these three sub-chessboards into the special chessboard, one L-type domino can be put on the junction of three smaller chessboards (seen in Figure 3(b)). The pane which is covered by the L-type domino on three sub-chessboards is the special pane on this chessboard, so the original problem is converted into four smaller chessboard coverage problems. Recursively use this division until the chessboard is simplified as the chessboard of 1×1.

Taking the special chessboard in Figure 1 as the example, the final chessboard coverage effect is seen in Figure 4. In generally teaching, to lively play the result of chessboard coverage, different colors are generally adopted to distinguish neighboring L-type dominos. However, as viewed from the actual teaching effect, the colorful pane will easily generate confusion of vision, and can not make students to clearly understand the coverage result. And the demonstration program of the colorful chessboard coverage is relatively complex. These factors show that the denotation of the chessboard coverage needs to be further studied to better adapt the teaching demands.

3.2 Problems existing in the algorithm

The total idea of chessboard coverage algorithm based on the divide-and-conquer strategy in the teaching materials is to divide the chessboard into four sub-chessboards first, and then respectively cover these four sub-chessboards. For each sub-chessboard, the program will first judge whether the special pane is in this sub-chessboard. If it is in the sub-chessboard, the program will recursively transfer the program to cover this sub-chessboard, or else, cover the neighboring panes with other three sub-chessboards, and then recursively transfer the program to cover this sub-chessboard. The concrete chessboard coverage algorithm ChessBoard can be described as follows.

```
void ChessBoard(int tr, int tc, int dr, int dc, int size)

{

if(size==1) return;

int t=tile++, s=size/2;

// cover the sub-chessboard of the top left corner

if(dr<tr+s && dc<tc+s)

ChessBoard(tr, tc, dr, dc, s);

else{Board[tr+s-1][tc+s-1]=t;

ChessBoard(tr, tc, tr+s-1, tc+s-1, s); }

// cover the sub-chessboard of the top right corner

if(dr<tr+s && dc>=tc+s)

ChessBoard(tr, tc+s, dr, dc, s);

else{Board[tr+s-1][tc+s]=t;

ChessBoard(tr, tc+s, tr+s-1, tc+s, s); }

// cover the sub-chessboard of the down left corner

if(dr>=tr+s && dc<tc+s)

ChessBoard(tr+s, tc, dr, dc, s);

else{Board[tr+s][tc+s-1]=t;

ChessBoard(tr+s, tc, tr+s, tc+s-1, s); }

// cover the sub-chessboard of the down right corner
```

if(dr>=tr+s && dc>=tc+s)

ChessBoard(tr+s, tc+s, dr, dc, s);

else{Board[tr+s][tc+s]=t;

ChessBoard(tr+s, tc+s, tr+s, tc+s, s); }

}

In above algorithm, a two-dimensional integer array Board is used to denote the chessboard. Board[0][0] is the pane of top left corner of the chessboard. Tile is a comprehensive integer variable in the algorithm and it is used to denote the number of the L-type domino, and its initial value is 0. And the input parameters of the algorithm include tr (the row number of the pane of top left corner of the chessboard), tc (the column number of the pane of top left corner of the chessboard), dr (the row number of the special pane), dc (the column number of the special pane), size (size=2^k, and it denotes that the specification of chessboard is $2^k \times 2^k$). Taking the special chessboard in Figure 1 as the example, according to the algorithm of ChessBoard, the sequence of chessboard coverage is seen in Figure 5, where, each three same numbers denotes the L-type domino of one type.

From the coverage sequence of Figure 5, though the ChessBoard algorithm uses the skill of algorithm design, but its implementation process is not completely consistent with the divide-and-conquer strategy. According to the divide-and-conquer strategy, after the algorithm judge the position of the special pane, it should use the L-type domino to cover the junction of three sub-chessboards. But the algorithm of ChessBoard splits this approach, i.e. the L-type domino at the junction of three sub-chessboards is divided into three parts which are implemented respectively in different program blocks. Because the algorithm adopts the recursive transfer, the coverage process of each sub-chessboard should follow this rule. Though the implementation process of the ChessBoard algorithm is correct, but it doesn't accord with the above divide-and-conquer strategy which uses one L-type domino to cover, so students will feel difficult to understand the problem and accept the idea of the divide-and-conquer algorithm. Because the divide-and-conquer is difficult, so if the design skill is added in the implementation of the algorithm, students will be afraid of difficult to study this algorithm and good teaching effect will not be realized.

4. Optimization of teaching contents

4.1 Optimization of problem denotation

First, aiming at the problem in the section of 3.1, optimize the problem denotation of chessboard coverage. Because in the teaching process, the colorful pane is easily confused in vision, and it makes against the understanding of the problem, so the denotation of the chessboard coverage is improved in the article, which can help students to totally grasp the problem as a whole, and clearly know the coverage result. Because the L-type domino is used to cover, so the polygonal lines with different directions can respectively denote four sorts of L-type dominos (seen in Figure 6). Comparing with the colorful coverage result in Figure 4, the result of Figure 6 is more simple and clear, and it is easy to be used in the teaching process.

4.2 Optimization of the solving algorithm

Next, optimize the solving algorithm. Though the ChessBoard algorithm is correct, but it makes against the teaching of the divide-and-conquer algorithm because it uses the skill of program design. To implement the standardization of the teaching content and reduce the difficulty of solving problem, the algorithm skill needs to be eliminated. The following algorithm ChessBoard 1 improves the ChessBoard algorithm, standardizes the flow of the algorithm, and makes it to be consistent with the divide-and-conquer strategy. Its total idea is to divide the chessboard into four sub-chessboards, and especially judge whether the special pane is in these four sub-chessboards. If it is in the sub-chessboard, use the L-type domino to cover the junction of other three sub-chessboards. When the judgment is over, transfer the program to cover these four sub-chessboards one by one. The concrete algorithm can be described as follows.

void ChessBoard1(int tr, int tc, int dr, int dc, int size)

{

if(size==1) return;

int t=tile++, s=size/2;

// Use (d) type domino to cover the junction of the chessboards

if(dr<tr+s && dc<tc+s)

{ Board[tr+s-1][tc+s]=t; Board[tr+s][tc+s-1]=t; Board[tr+s][tc+s]=t;

int dr1=dr, dc1=dc, dr2= tr+s-1, dc2= tc+s, dr3= tr+s, dc3= tc+s-1, dr4= tr+s, dc4= tc+s;}

// Use (c) type domino to cover the junction of the chessboards

if(dr<tr+s && dc>=tc+s)

{ Board[tr+s-1][tc+s-1]=t; Board[tr+s][tc+s-1]=t; Board[tr+s][tc+s]=t;

int dr1=tr+s-1, dc1=tc+s-1, dr2= dr, dc2= dc, dr3= tr+s, dc3= tc+s-1, dr4= tr+s, dc4= tc+s;}

// Use (b) type domino to cover the junction of the chessboards

if(dr>=tr+s && dc<tc+s)

{ Board[tr+s-1][tc+s-1]=t; Board[tr+s-1][tc+s]=t; Board[tr+s][tc+s]=t;

int dr1=tr+s-1, dc1=tc+s-1, dr2= tr+s-1, dc2=tc+s, dr3=dr, dc3=dc, dr4= tr+s, dc4= tc+s;}

// Use (a) type domino to cover the junction of the chessboards

if(dr>=tr+s && dc>=tc+s)

{ Board[tr+s-1][tc+s-1]=t; Board[tr+s-1][tc+s]=t; Board[tr+s][tc+s-1]=t;

int dr1=tr+s-1, dc1=tc+s-1, dr2=tr+s-1, dc2=tc+s, dr3=tr+s, dc3=tc+s-1, dr4=dr, dc4=dc;}

// Respectively cover four sub-chessboards

ChessBoard1(tr, tc, dr1, dc1, s);

ChessBoard1(tr, tc+s, dr2, dc2, s);

ChessBoard1(tr+s, tc, dr3, dc3, s);

ChessBoard1(tr+s, tc+s, dr4, dc4, s);

}

In above algorithm, the meanings of the two-dimensional array Board, the number tile of the L-type domino, and the input parameters tr, tc, dr, dc, and size are same with the algorithm of ChessBoard1. The difference is that after the L-type domino covers the junction of four sub-chessboards, the program redefines the row number and column number of four special panes for these four sub-chessboards, i.e. redefining 8 local integer variables: the row number dr1 and the column number dc1 of the special pane in the first sub-chessboard, the row number dr2 and the column number dc2 of the special pane in the second sub-chessboard, the row number dr3 and the column number dc3 of the special pane in the third sub-chessboard, the row number dr4 and the list number dc4 of the special pane in the fourth sub-chessboard. In another word, after L-type domino covers the junction of sub-chessboards, four sub-chessboards all change as the special sub-chessboards with their own special pane. Therefore, the special panes of various sub-chessboards must be redefined, and 8 local integer variables are used to transfer the row numbers and column numbers of the special panes in these four special sub-chessboards. To compare with the ChessBoard algorithm, taking the special chessboard in Figure 1 as the example, according to the algorithm of ChessBoard1, the sequence of the chessboard coverage is seen in Figure 7.

In the comparison, the chessboard coverage process of the ChessBoard1 algorithm is consistent with the solving approach with the divide-and-conquer strategy. Different with the ChessBoard algorithm which splits the L-type domino to cover, the ChessBoard1 algorithm is transferred recursively once, and generates a L-type domino, which simplifies the implementation of the divide-and-conquer in the algorithm teaching, and liberates students from complex concrete computation, so students' learning target will be more specific, and they will mainly understand the basic idea and solving approaches of the divide-and-conquer algorithm, and grasp the essential of the problem, and need not waste too much energy in the skill of program design.

5. Analysis of algorithm complexity

From the general design mode of the divide-and-conquer algorithm, the algorithm is a recursive process. Therefore, the computation efficiency of the divide-and-conquer algorithm can be analyzed by the recursion equation. For the convenience, suppose that the problem which division threshold value $n_0=1$ and the solution scale of the adhoc algorithm is 1 consumes 1 unit time. And suppose that the divide-and-conquer algorithm divides the problem with the scale of n into k sub-problems with the scale of n/m, and to divide the original problem into k sub-problems and combine the solutions of k sub-problems as the solution of the original problem by the algorithm merge needs f(n) units time. If T(n) denotes the computation time needing by the problem P with the solution scale of |P|=n by the divide-and-conquer algorithm, so

$$
\begin{cases}
T(1) = 1 \\
T(n) = kT(n/m) + f(n)
\end{cases}
\tag{1}
$$

By the iterative method of solving the recursion equation introduced in the asymptotic order solution in the complexity

of the algorithm, the solution of the equation (1) can be solved.

$$T(n) = n^{\log_m k} + \sum_{j=0}^{\log_m n - 1} k^j f(n/m^j) \qquad (2)$$

In the algorithm of ChessBoard of the chessboard coverage problem, suppose that T(k) is the time that the algorithm of ChessBoard1 covers one chessboard of $2^k \times 2^k$, so from the divide-and-conquer strategy equation (1) of the algorithm, T(k) satisfies following recursion equation.

$$T(k) = \begin{cases} O(1) & k = 0 \\ 4T(k-1) + O(1) & k > 0 \end{cases} \qquad (3)$$

According to the equation (2), solve this recursion equation, and obtain T(k) = O(4^k). Because the amount of L-type domino to cover one chessboard of $2^k \times 2^k$ is (4^k-1)/3, the algorithm of ChessBoard1 is the optimal algorithm on the asymptotic meaning.

6. Conclusions

In general algorithm strategy, the divide-and-conquer algorithm is one of the most important sorts, and its establishment principle is to divide and rule, so it is the base of many high-efficiency algorithms. The application of the divide-and-conquer algorithm in the solving of chessboard coverage problem is studied in the article. Three approaches of the divide-and-conquer algorithm to solve the chessboard coverage problem are an organic integer, and the division of the original problem into many sub-problems is the key content, and it is the key approach to solve problem by the divide-and-conquer algorithm. The present divide-and-conquer method uses program skill to solve the problem of chessboard coverage, and splits the L-type dominos and cover, which is not consistent with the former analysis, and adds difficulties for the divide-and-conquer algorithm which is not complex originally, and the teaching effect is not ideal. The divide-and-conquer method contains abundant mathematical ideas which should be dug and studied in the teaching to ensure the continuity and consistence of students' thinking development and enhance the learning effect. Therefore, aiming at the problem of chessboard coverage, the coverage sequence of L-type dominos in the flow of the divide-and-conquer algorithm is improved, and the improved algorithm can not only eliminate the algorithm skill, but add the standardization and consistence of the algorithm and achieve better teaching effect.

References

Cormen TH, Leiserson CE, Rivest RL, et al. (2001). *Introduction to Algorithms (Second Edition).* MIT Press. 2001.

Goodrich MT & Tamassia R. (2007). *Algorithm Analysis and Design.* Beijing: People's Posts & Telecom Press.

Huang, Jing, Liu, Dayou & Yang, Bo, et al. (2008). A Self-organization Based Divide and Conquer Algorithm for Distributed Constraint Optimization Problems. *Journal of Computer Research and Development.* No. 45(11). P. 1831-1839.

Min F, Xie LJ & Liu QH. (2005). A Divide-and-Conquer Discretization Algorithm. *Lecture Notes in Computer Science.* No. 3613. P. 1277-1286.

Ohio C. (2007). Learning: An Effective Approach in Endgame Chess Board Evaluation. *Proceedings of the Sixth International Conference on Machine Learning and Applications.* P.464-469.

Shimojoa F, Kalia RK & Nakano A, et al. (2005). Embedded divide-and-conquer algorithm on hierarchical real-space grids: parallel molecular dynamics simulation based on linear-scaling density functional theory. *Computer Physics Communications.* No. 167(3). P. 151-164.

Stephen RM, Brian JS & Karen W, et al. (2004). Divide and Conquer. *Psychological Science.* No. 15(6). P. 420-425.

Wang, Suli & Bai, Shouhua. (2005). Teaching Method of Algorithm Analysis and Design. *Journal of Xiangtan Normal University (Natural Science Edition).* No. 27(3). P.124-127.

Wang, Xiaodong. (2007). *Computer Algorithm Design and Analysis.* Beijing: Electronics Industry Publishing House.

Wu YZ, Jiang ZS & Ding JW, et al. (2008). Subdivision solving of multi-domain simulation models. *Journal of Huazhong University of Science and Technology.* No. 36(10). P. 41-44.
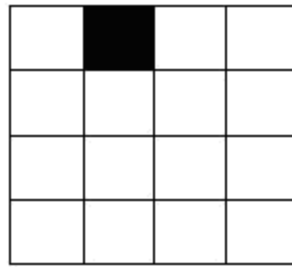
Figure 1. A Special Chessboard when *k*=2
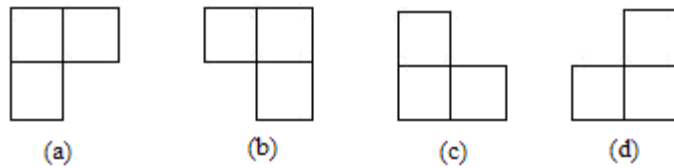
Figure 2. Four L-type Dominos with Different Forms
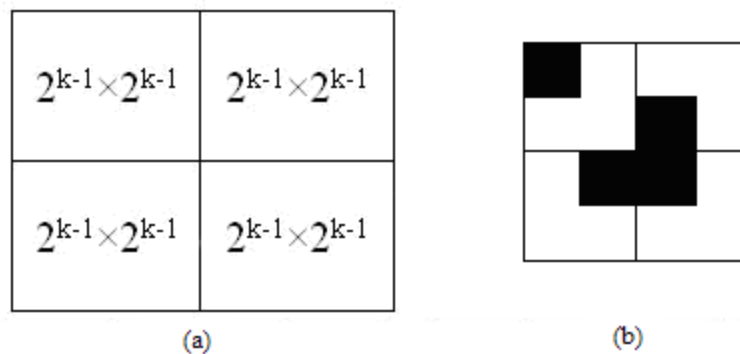


Figure 3. Division of Chessboard
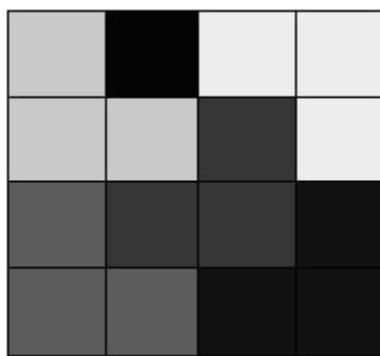

Figure 4. Result of Chessboard Coverage

Figure 5. Chessboard Coverage Sequence of the ChessBoard Algorithm
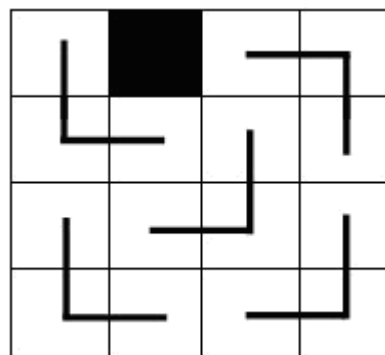

Figure 6. Simple Denotation of Chessboard Coverage Result

Figure 7. Chessboard Coverage Sequence of the ChessBoard1 Algorithm

Fly Ash-Based Geopolymer Mortar Incorporating Bottom Ash

Djwantoro HARDJITO (Corresponding author)

Dept. of Civil Engineering

Petra Christian University

Surabaya, Indonesia

E-mail: djwantoro.h@gmail.com

Shaw Shen, FUNG

Dept. of Civil and Construction Engineering

School of Engineering and Science

Curtin University of Technology

Miri, Sarawak, Malaysia

Abstract

This paper presents the results of study on effect of various parameters on mechanical properties of fly ash-based geopolymer mortar with bottom ash as partial or full replacement for sand. Compressive strength of samples with 10% bottom ash (BA) was comparable to those with only sand. Further increase in bottom ash content decreased the compressive strength. However, the reverse tendency occurred after exposing the samples to 1000°C for 24 hours.

Keywords: Fly ash, Bottom ash, Geopolymer mortar, Compressive strength, Thermal exposure, Workability

1. Introduction

Portland cement is widely used in concrete industry since many decades ago, however it releases green house gases, i.e. carbon dioxide (CO_2), into the atmosphere during its manufacture (Malhotra, 2002b). Geopolymer technology is one of the new technologies attempted to reduce the use of Portland cement in concrete. Fly ash reacts with alkaline solutions to form a cementitious material; fly ash based geopolymer; which does not emit carbon dioxide into the atmosphere. In this project, bottom ash is considered as partial- or full-replacement for sand as fine aggregate in the geopolymer mortar. To date, bottom ash from Sejingkat Coal Fired Power Station in Kuching, Sarawak, Malaysia, has not been utilised yet.

Fly ash and bottom ash are residues from the combustion of coal. Fly ash is captured in the chimney while bottom ash is collected from the bottom of the furnace from the coal fired power plant. Furthermore, the particles of fly ash are very fine whereas bottom ash has much larger particle size, which is about the size of sand but more porous. In Sejingkat Coal Fired Power Station, fly ash and bottom ash are disposed off into an 81,000 m^2 area, 2.4 m deep ash pond situated beside the power station (Tsen, 2008). In fact, currently there are two ash ponds with one of them has been fully utilized.

Fly ash based geopolymer with bottom ash gives emphasis in reducing carbon dioxide emission and in recycling fly ash and bottom ash. Since fly ash and bottom ash are the waste products of coal fired power plant, this research can lead to the awareness of sustainable development to the society. This is very advisable in sustainable developments to reduce CO_2 emission and to recycle the waste materials. At present time, there is limited information on the influence of parameters on geopolymer available, especially geopolymer with bottom ash as the fine aggregate. As a result, study on the effect of different parameters on the fly ash based geopolymer with bottom ash as sand replacement is needed. In addition, this research can provide additional information and to further introduce geopolymer to concrete industry.

2. Literature Review

Geopolymers are amorphous to semi-crystalline three-dimensional alumino-silicate polymers similar to zeolites. Geopolymers consist of polymeric silicon-oxygen-aluminium framework with silicon and aluminium tetrahedral alternately linked together in three direction by sharing all the oxygen atoms. The negative charge created by aluminium is balanced by the presence of positive ions such as Na^+, K^+, and Ca^+. The empirical formula of these mineral polymers is $M_n[-(SiO_2)_z-AlO_2]_n \cdot wH_2O$, where M is an alkali cation such as potassium or sodium, the symbol - indicates the presence of a bond, z is 1, 2 or 3, and n is the degree of polymerisation (Davidovits, 1994).

Geopolymers are environmental friendly materials which do not emit green house gases during polymerisation process. Besides, they need only moderate energy to produce. Geopolymers are made from source materials with silicon (Si) and Aluminium (Al) content, thus they can be made using fly ash, waste-product of coal-fired power station, as the source materials (Hardjito, Wallah, Sumajouw, & Rangan, 2004a). Furthermore, geopolymer possesses excellent mechanical properties which does not dissolve in acidic solution and does not generate any hazardous alkali-aggregate reaction even with alkali content as high as 9.2% (Davidovits, 1999).

Optimum curing temperature of 60 °C was suggested for the study of the geopolymer mortar with small 50 mm cube size. This suggestion is based on the fact that smaller cube is having higher surface area-to-volume ratio compared to larger cube. Which, as a result, the smaller cube is more vulnerable to the high curing temperature and would experience loss of moisture during curing compared with the larger samples (P. Chindaprasirt, Chareerat, & Sirivivatnanon, 2006).

Álvarez-Ayuso et al. (2007) suggested that the optimum curing time would be 48 hours. Curing time showed commonly a positive effect to the compressive strength of geopolymer mortar, and this effect is much more noticeable at the optimum curing temperature, 80 °C, suggested by them (Álvarez-Ayuso, et al., 2007). Besides, Swanepoel and Strydom (2002) also agreed that the optimum curing time for a geopolymer mortar would be 48 hours or 2 days.

On the other hand, Hardjito et al. (2005) mentioned that increase in the curing time would also assist the increase in compressive strength which also agreed by other researcher. But, a curing time further than 48 hours does not increase compressive strength significantly (Hardjito, Wallah, Sumajouw, & Rangan, 2004b; Hardjito, et al., 2005).

Increase of concentration of NaOH increases the compressive strength of geopolymer. This is mainly because of the concentration of NaOH solution is directly affecting the dissolution of the metakaolinite particulates, which affecting the formation of the geopolymer framework. To have strong inter-molecular bonding strength of the geopolymer, more reactive bond for the monomer is needed. This can be achieved by a better dissolving ability to metakaolinite particulates. To obtain a better dissolving ability to metakaolinite particulates, a higher concentration of NaOH solution is required (Wang, Li, & Yan, 2005). However, in Chindaprasirt, Chareerat, and Sirivivatnanon (2007) research, the effect of concentration of NaOH on compressive strength was not clear. The concentration of NaOH of 10, 15, 20 M were used, and the average compressive strengths were 48.4, 49.1 and 50.2 MPa respectively (P. Chindaprasirt, et al., 2006).

Geopolymer with fluidized bed combustion bottom ash (FBC-BA) experienced a decrease in compressive strength with the increase of the content of FBC-BA in the prepared specimens. Increasing the content of FBC-BA to about 50% caused the decrease of the compressive strength (Slavik, Bednarik, Vondruska, & Nemec, 2008).

For the case of normal fly ash concrete incorporating bottom ash as replacement for fly ash, the increase in bottom ash content decreased the compressive strength. Furthermore, most of the compressive strengths were gained after 28 days. The pozzolanic reactivity of bottom ash could be improved with adequate grinding and use it as sand replacement in concrete, where sand is more expensive than bottom ash (Kula, Olgun, Erdogan, & Sevinc, 2001).

Water retainability is defined as the amount of water absorbed into the pores and adsorbed on the rough surface of bottom ash. The usual collapsed-cone test method to determine the saturated surface dry condition was not achievable for bottom ash. Therefore an alternative method based on the gravitational removal of excess water from the bottom ash was introduced to determine the water retainability of bottom ash (Kasemchaisiri & Tangtermsirikul, 2007).

The compressive strength of fly ash-based geopolymer mortar exposed to 400 °C increased by about 100% compared to samples without any exposure to high thermal environment. Geopolymer possesses high thermal resistance up to 800 °C without showing any decrease in compressive strength (Tsen, 2008). However, after exposure to thermal exposure above 800 °C, compressive strength of geopolymer prepared using sodium based alkaline activator rapidly declined (Bakharev, 2006). In fact, geopolymer mortar does not experience release water in an explosive manner or dehydrate to a powder like OPC. In brief, geopolymer mortar is able to resist thermal exposure up to 1000 °C (Gourley & Johnson, 2005).

3. Materials and Experimental Details

3.1 Materials

Fly ash, Class F under ASTM C 618, used in this experiment was obtained from Sejingkat Coal-Fired Power Station. The coal used in the power station is mainly supplied from the coal mine in Merit Pila, Kapit, Sarawak, Malaysia. Specific surface area and particle density of the fly ash are 1.51 m^2/ml and 2370 kg/m^3 respectively. The chemical composition of the fly ash, as determined by X-Ray Fluorescence (XRF) analysis is shown in Table 1. According to the chemical composition as shown in Table 1, the mass ratio of SiO_2 to Al_2O_3 of the fly ash is 2.34.

Similarly, bottom ash used in this experiment was obtained from Sejingkat Coal-Fired Power Station. The specific gravity of the bottom ash is 2.23 and fineness modulus (FM) is 0.14. Suitable moisture content (22%) of bottom ash was prepared in advance and stored for prior use. Sand used in this experiment is in saturated surface-dry (SSD) condition. Fineness modulus (FM) and specific gravity are 1.44 and 2.67 respectively. These data reveal that the particle size of the sand is rather small with FM only 1.44, moreover the particle size of the bottom ash is even smaller than sand (FM of 0.14).

Mixture of Potassium Silicate (K_2SiO_3) solution and Potassium Hydroxide (KOH) solution were chosen as the alkaline activator. This was because the type of alkaline activator that contained only hydroxides revealed in a lower reaction rate than when soluble silicates were also used as the activators (Palomo, Grutzeck, & Blanco, 1999). Furthermore, potassium-based activator was chosen because it produced a better strength compared to sodium-based activator (Xu & Van Deventer, 2000).

3.2 Experimental Programme and Mixture Proportion

In order to analyse the effect of content of bottom ash on compressive strength, R1 was chosen as the reference sample. On the other hand, R2 was chosen as the reference sample in the experiment on the effect of different curing temperature, concentration of KOH solution and K_2SiO_3-to-KOH solution ratio by mass on compressive strength.

Furthermore, mixtures R1, R2, 1-7, 12, 13, 15 and 17 were subjected to thermal exposure of 400 °C, 700 °C and 1000 °C on the sixth day and compressive strength test was conducted on the next day. Seventh days compressive strength of samples with no thermal exposure was taken as the reference for the compressive strength of samples subjected to thermal exposure. The experimental programme is shown in Table 2.

Fine aggregate to fly ash ratio by mass of 2.75 was attempted to design the required quantity of all geopolymer mortars (2006). Besides that, K_2SiO_3 solution and KOH solution were weighted according to the required proportion. The mixture proportion is shown in Table 3.

3.3 Mixing, Casting, Curing and Thermal Exposure

The mixing and casting of the geopolymer mortar was referred to method implemented by Tsen (2008). Raw materials, i.e. fly ash and fine aggregate, were dry mixed in the mixer at the paddle speed of 140 ±5 r/min for 2 minutes. At the same time, alkaline activator with mixture of K_2SiO_3 solution and KOH solution were premixed in another flask. After that, the alkaline activator was mixed with the raw materials in the mixer for another 10 minutes.

Then, the fresh geopolymer mortar was placed in the 50 mm x 50 mm x 50 mm specimen moulds in two layers. Each layer was compacted by a tamper for 20 times. After the casting of the geopolymer mortars in the specimen moulds, the mixtures were vibrated using vibrating table for another 2 minutes to remove air voids. All the mixing and casting were done in an air-conditioned room of temperature approximately at 25 °C.

Next, all the mixtures were cured in an oven without delay time at the specific curing temperature for 24 hours. Samples were demoulded after the curing process in the oven and cured in room temperature until the testing age.

Samples that subjected to thermal exposure were exposed in a furnace on the sixth day at an incremental rate of 10 °C/min from room temperature. The desired temperature was maintained for 3 hours before the samples were allowed to cool naturally to room temperature in the furnace. Then the samples were tested on the next day.

3.4 Testing

Three 50 mm x 50 mm x 50 mm samples were tested for each data. Load rate 90 kN/min was applied on the sample. The maximum load shown by the testing machine was recorded and the compressive strength of the sample was calculated.

Workability was measured by the flow of the fresh geopolymer mortar on flow table for mortar. First, flow mould was placed in the middle of the flow table. A layer of fresh geopolymer mortar about 25 mm thick was placed in the mould and tamped with the tampers for 20 times. This was repeated for the second layer. Then the mould was lifted away and immediately the table was dropped from a height of 12.7 ± 0.13 mm for 25 times in 15 sec. Finally, the diameter of the geopolymer mortar along the four lines scribed in the table top was recorded. Then, the flow expressed as a percentage of the original base diameter was calculated as follow. First, 'A', the average of the four readings, in millimeters, minus

the original inside base diameter was calculated. Next, 'A' was divided by the original inside base diameter and multiplied by 100.

4. Results and Discussions

4.1 Compressive Strength

(1) Content of Bottom Ash

Mixture R1, R2, 12-17 were made to investigate the effect of content of bottom ash on compressive strength and Fig. 1 shows the results. The compressive strength of the bottom ash geopolymer mortar decreases with the increase of bottom ash content. This could, probably, be due to the water released into the mixture by the bottom ash (Andrade, Rocha, & Cheriaf, 2008). Water can be highly retained, in term of absorption and adsorption, into and onto the bottom ash due to the high porosity and irregular surface (Kasemchaisiri & Tangtermsirikul, 2007). With the amount of the water increased in the mortar, the compressive strength of the geopolymer mortar eventually decreases. On the other hand, the higher porosity of the bottom ash also caused the lower compressive strength to the geopolymer mortar (Prinya Chindaprasirt, Jaturapitakkul, Chalee, & Rattanasak, 2008). However, 10% of river sand can be replaced by bottom ash as fine aggregates in fly ash-based geopolymer mortar without any significant decrease in its compressive strength.

(2) Curing Temperature

Mixture R2 and 1-3 were made to analyse the effect of curing temperature on compressive strength and Fig. 2 shows the results. A higher curing temperature will increase the compressive strength of the geopolymer mortar. This is because energy required for dissolution of fly ash is an endothermic process (Álvarez-Ayuso, et al., 2007). However, the samples will normally experience the loss of moisture content with high curing temperature whereby geopolymerisation requires the presence of moisture to achieve a good compressive strength (P. Chindaprasirt, et al., 2006).

(3) Concentration of KOH Solution

Mixture R2 and 4-7 were made to study the effect of concentration of KOH solution on compressive strength and Fig. 3 shows the results. The higher the concentration of the KOH solution, the higher the compressive strength is. This is mainly because the concentration of KOH solution is directly affecting the dissolution of fly ash which affects the formation of the geopolymer framework (Wang, et al., 2005). However, the compressive strength resulted in this research is slightly lower than compressive strength in research conducted by Tsen (2008). This is most probably due to the incorporation of bottom ash in the sample.

(4) K2SiO3-to-KOH Solution Ratio by Mass

Mixture R2 and 8-11 were made to study the effect of K_2SiO_3-to-KOH solution ratio by mass on compressive strength and Fig. 4 shows the results. Compressive strength of samples with K_2SiO_3-to-KOH solution ratio by mass of 0.4 to 1.0 are noticeably higher than those with K_2SiO_3-to-KOH solution ratio by mass of 1.5 and 2.5 which is similar to research by Tsen (2008). Again, similar to this researcher's research, the optimum K_2SiO_3-to-KOH solution ratio by mass for compressive strength was 1.0. However, this was rather unexpected. In research conducted by Hardjito et al. (2004b) on the low calcium fly ash reacted by sodium based alkaline solution showed that the higher of silicate-to-hydroxide solution ratio by mass resulted in higher compressive strength.

4.2 Thermal Resistance

Mixture R1, R2, 12, 13, 15 and 17 were made to study the effect of content of bottom ash on compressive strength. From Fig. 5, the highest compressive strength is achieved by the samples exposed to 400 °C which also shown in Tsen (2008) report. Geopolymer possesses high thermal resistance up to 700 °C without any significant decrease in compressive strength. Furthermore, samples exposed to 1000 °C is experiencing decrease in compressive strength as reported also by other researcher (Bakharev, 2006). In fact, similar to other researcher, these samples do not experience release water in an explosive manner or dehydrate to a powder like OPC (Gourley & Johnson, 2005).

The compressive strength increases with the increase of bottom ash content in samples exposed to 1000 °C. Undeniable, this trend is different compared to the samples that are not exposed to any high thermal environment or exposed to temperature lower than 700 °C which can be observed from Fig. 5. In brief, samples with lower bottom ash content (0%-25%) decreases in compressive strength after exposure to elevated temperature of 400 °C to 1000 °C, meanwhile samples with higher bottom ash content (50%-100%) increases in compressive strength after exposure to elevated temperature of 400 °C to 1000 °C which can be observed from Fig. 6. This is probably due to higher temperature, especially at 1000 °C, activated the bottom ash, and indeed increased the compressive strength of the samples. Thus, further research on the characteristic of bottom ash in high temperature is needed.

4.3 Workability

Workability of fresh geopolymer mortar of mixture R1, R2 and 12-17 were studied in this section. Effect of bottom ash content on workability is shown in Fig. 7. First, workability measured by flow of fresh geopolymer mortar increases

with the increase of bottom ash content in the mixture. This is because water retained by the bottom ash will be released into the mixture during the mixing (Andrade, et al., 2008). This additional water will increase the workability of the fresh mortar. However, with the amount of bottom ash in fresh geopolymer mortar more than 75%, workability decreases. This is most probably due to the angular shape and rough texture causing high inter-particle friction of the bottom ash although the water content increased in the mixture (Kasemchaisiri & Tangtermsirikul, 2007). The more the content of bottom ash in fresh mortar, the higher the inter-particle friction is.

5. Conclusions

(1). Increase of bottom ash content decreases the compressive strength of geopolymer mortar. However, compressive strength of geopolymer mortar with 10% of bottom ash is comparable to geopolymer mortar without bottom ash.

(2). Increase of curing temperature increases the compressive strength of the geopolymer mortar.

(3). Increase in concentration of KOH solution also increases the compressive strength of geopolymer mortar.

(4). The optimum K_2SiO_3-to-KOH solution ratio by mass is about 1.0.

(5). Geopolymer mortar with lower bottom ash content (0%-25%) decreases in compressive strength after exposure to elevated temperature from 400 °C to 1000 °C, meanwhile geopolymer mortar with higher bottom ash content (50%-100%) increases in compressive strength after exposure to elevated temperature of 400 °C to 1000 °C.

(6). Increase of bottom ash content increases workability of fresh geopolymer mortar but it decreases with bottom ash content more than 75%.

References

Álvarez-Ayuso, E., Querol, X., Plana, F., Alastuey, A., Moreno, N., Izquierdo, M., et al. (2007). Environmental, physical and structural characterisation of geopolymer matrixes synthesised from coal (co-)combustion fly ashes. *Journal of Hazardous Materials,* 154(1-3), 175-183.

Andrade, L. B., Rocha, J. C., & Cheriaf, M. (2009). Influence of coal bottom ash as fine aggregate on fresh properties of concrete. *Construction and Building Materials,* 23(2), 609-614.

Bakharev, T. (2006). Thermal behaviour of geopolymers prepared using class F fly ash and elevated temperature curing. *Cement and Concrete Research, 36*(6), 1134-1147.

Chindaprasirt, P., Chareerat, T., & Sirivivatnanon, V. (2006). Workability and strength of coarse high calcium fly ash geopolymer. *Cement and Concrete Composites, 29*(3), 224-229.

Chindaprasirt, P., Jaturapitakkul, C., Chalee, W., & Rattanasak, U. (2008). Comparative study on the characteristics of fly ash and bottom ash geopolymers. *Waste Management,* 29(2), 539-543.

Davidovits, J. (1994). High-Alkali Cements for 21st Century Concretes. *Special Publication, 144*, 383-398.

Davidovits, J. (1999, June 30-July 2, 1999). *Chemistry of Geopolymeric Systems, Terminology.* Paper presented at the Geopolymer '99 International Conference, Saint-Quentin, France.

Gourley, J. T., & Johnson, G. B. (2005, June 29-July 1, 2005). *Develoments in geopolymer precast concrete.* Paper presented at the World Congress Geopolymer 2005, Saint-Quentin, France.

Hardjito, D., Wallah, S. E., Sumajouw, D. M. J., & Rangan, B. V. (2004a). *Properties of Geopolymer Concrete with Fly Ash as Source Material: Effect of Mixture Composition.* Paper presented at the Seventh CANMET/ACI International Conference on Recent Advances in Concrete Technology Las Vegas, Nevada, U.S.A.

Hardjito, D., Wallah, S. E., Sumajouw, D. M. J., & Rangan, B. V. (2004b). On the Development of Fly Ash-Based Geopolymer Concrete. *ACI Materials Journal, 101*(6), 467-472.

Hardjito, D., Wallah, S. E., Sumajouw, D. M. J., & Rangan, B. V. (2005). Fly ash-based geopolymer concrete. *Australian Journal of Structural Engineering, 6*(1), 77-84.

Kasemchaisiri, R., & Tangtermsirikul, S. (2007). A method to determine water retainability of porous fine aggregate for design and quality control of fresh concrete. *Construction and Building Materials, 21*(6), 1322-1334.

Kula, I., Olgun, A., Erdogan, Y., & Sevinc, V. (2001). Effects of colemanite waste, cool bottom ash, and fly ash on the properties of cement. *Cement and Concrete Research, 31*(3), 491-494.

Malhotra, V. M. (2002b). Introduction: Sustainable Development and Concrete Technology. *Concrete International, 24*(7), 22.

Palomo, A., Grutzeck, M. W., & Blanco, M. T. (1999). Alkali-activated fly ashes: A cement for the future. *Cement and Concrete Research, 29*(8), 1323-1329.

Slavik, R., Bednarik, V., Vondruska, M., & Nemec, A. (2008). Preparation of geopolymer from fluidized bed

combustion bottom ash. *Journal of Materials Processing Technology, 200*(1-3), 265-270.

Swanepoel, J. C., & Strydom, C. A. (2002). Utilisation of fly ash in a geopolymeric material. *Applied Geochemistry, 17*(8), 1143-1148.

Tsen, M. Z. (2008). *The properties of fly ash-based geopolymer mortar with potassium-based alkaline reactor.* Unpublished BEng diss., Curtin University of Technology

Wang, H., Li, H., & Yan, F. (2005). Synthesis and mechanical properties of metakaolinite-based geopolymer. *Colloids and Surfaces A: Physicochemical and Engineering Aspects, 268*(1-3), 1-6.

Xu, H., & Van Deventer, J. S. J. (2000). The geopolymerisation of alumino-silicate minerals. *International Journal of Mineral Processing, 59*(3), 247-266.

Table 1. Chemical Composition of Fly Ash as Determined by XRF

Oxides	% mass
SiO_2	58.0
Al_2O_3	24.8
Fe_2O_3	7.17
K_2O	3.14
CaO	2.40
MgO	1.95
TiO_2	1.05
P_2O_5	0.34
Na_2O	0.30
MnO	0.18
SO_3	0.08
LOI	0.32

Table 2. Experimental Programme

Mixture No.	Curing Temp (°C)	Conc. of KOH (M)	K_2SiO_3-to-KOH Ratio by Mass	Bottom Ash Content (%)	Sand Content (%)
R1	60	12	1.0	0	100
R2	60	12	1.0	10	90
1	50	12	1.0	10	90
2	70	12	1.0	10	90
3	80	12	1.0	10	90
4	60	6	1.0	10	90
5	60	8	1.0	10	90
6	60	10	1.0	10	90
7	60	14	1.0	10	90
8*	60	12	0.4	10	90
9*	60	12	0.8	10	90
10*	60	12	1.5	10	90
11*	60	12	2.5	10	90
12	60	12	1.0	25	75
13	60	12	1.0	50	50
14*	60	12	1.0	65	35
15	60	12	1.0	75	25
16*	60	12	1.0	90	10
17	60	12	1.0	100	0

*Mixtures do not subject to thermal exposure.

Table 3. Mixture Proportion

Mixture No.	Fine Aggregate		Fly Ash (kg/m³)	K₂SiO₃ (kg/m³)	KOH (kg/m³)
	Bottom Ash (kg/m³)	Sand (kg/m³)			
R1	0	1382	503	127.5	127.5
R2	138	1244	503	127.5	127.5
1	138	1244	503	127.5	127.5
2	138	1244	503	127.5	127.5
3	138	1244	503	127.5	127.5
4	138	1244	503	127.5	127.5
5	138	1244	503	127.5	127.5
6	138	1244	503	127.5	127.5
7	138	1244	503	127.5	127.5
8*	138	1244	503	72.9	182.1
9*	138	1244	503	113.3	141.7
10*	138	1244	503	153.0	102.0
11*	138	1244	503	182.1	72.9
12	346	1036	503	127.5	127.5
13	691	691	503	127.5	127.5
14*	898	484	503	127.5	127.5
15	1036	346	503	127.5	127.5
16*	1244	138	503	127.5	127.5
17	1382	0	503	127.5	127.5

*Mixtures do not subject to thermal exposure.
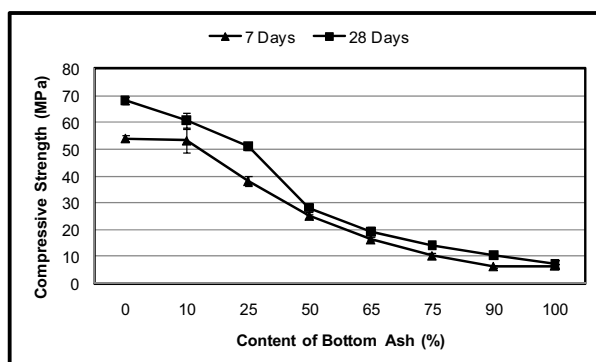
Figure 1. Effect of Content of Bottom Ash on Compressive Strength
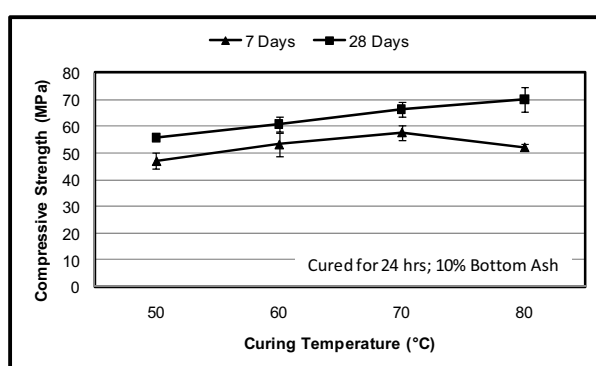
Figure 2. Effect of Curing Temperature on Compressive Strength
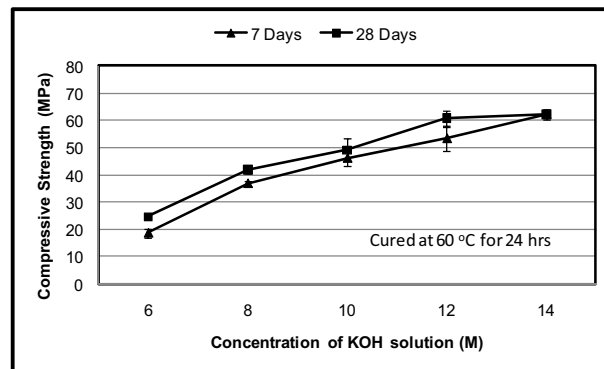
Figure 3. Effect of Concentration of KOH Solution on Compressive Strength
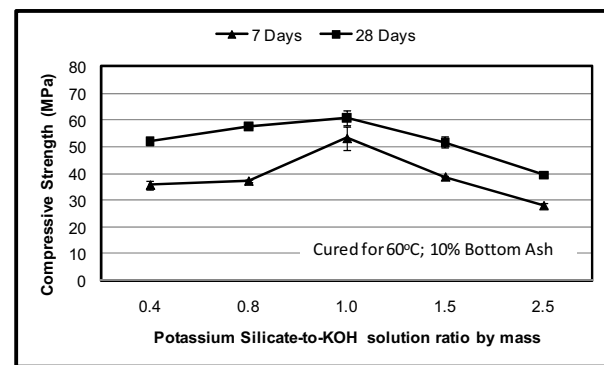
Figure 4. Effect of K_2SiO_3-to-KOH Solution Ratio by Mass on Compressive Strength
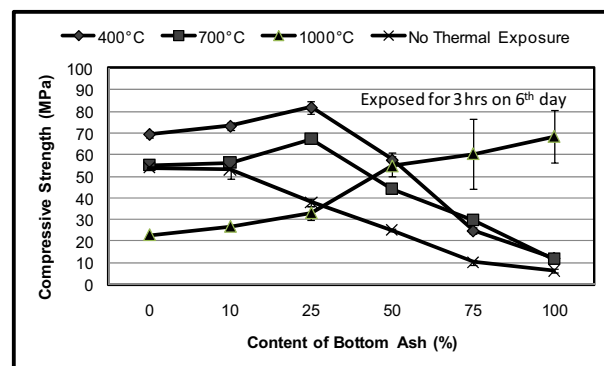

Figure 5. Effect of Content of Bottom Ash on Compressive Strength after Thermal Exposure
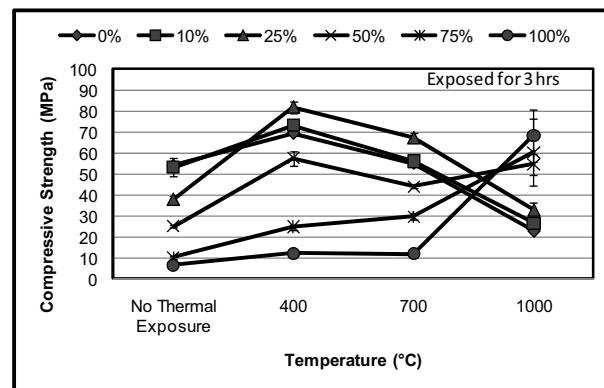

Figure 6. Effect of Thermal Exposure on Compressive Strength
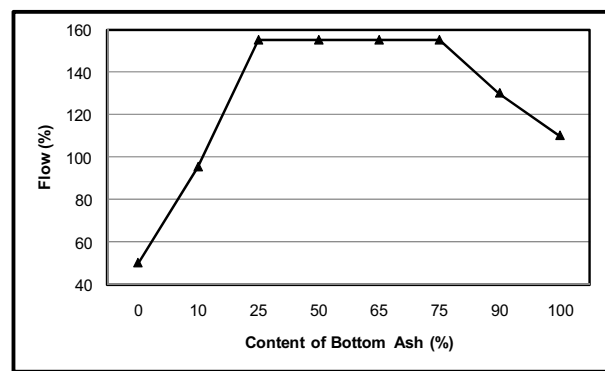
Figure 7. Effect of Content of Bottom Ash on Workability

Development of Environmentally Friendly Water-Based Synthetic Metal-Cutting Fluid

Yuzan Yu, Yugao Guo (Corresponding author), Lei Wang & Enqi Tang

College of Environment and Chemical Engineering

Tianjin Polytechnic University, Tianjin 300160, China

E-mail: york_guo@yahoo.com

Abstract

This paper introduces a method for preparation of environmentally friendly water-based synthetic metal-cutting fluid, which is formulated with the self-made triethanolamine ricinoleate as base oil and other additives. This cutting fluid exhibits good cooling, cleaning, anti-rust, anti-corrosive and lubricating properties, is totally free of mineral oil, animal oil, nitrite that is harmful to the human body, phosphate that causes water pollution and etc., and has stable and reliable quality, long service life, easily available raw materials and low production cost. It is quite a perfect "environmentally friendly cutting fluid".

Keywords: Metal-cutting fluid, Triethanolamine ricinoleate, Water-based cutting fluid, Biodegradation, Base oil

Preface

Metal-cutting fluid, an indispensable additive in metal-cutting process, has functions of lubricating, cooling, cleaning, anti-rust and etc. It has remarkable effects on increasing the durability of cutter and the efficiency of production, improving the product quality, and prolonging the service life of cutter, in turn prolongs the service life of machine and ensures the stability and reliability of working conditions of machine. Therefore, research on cutting fluid technology, as well as improvement of cutting fluid quality play important roles in the modern mechanical processing industry. However, many commercially available cutting fluids contain organic sulfur, chlorine, nitrite and etc that are harmful to the human body and environment, which have severely negative effects on their applications (Feng, Jufen et al, 1995, p. 40-43).

The toxicity of cutting fluid causes harm to the human body. Under the conditions of high speed cutting or high load cutting, the resulted high temperature accelerates the oil-based cutting fluid to release harmful gases and oil mist, the lower the ignition point and viscosity of cutting fluid are, the severer the oil mist is. As for the water-based cutting fluid, the resulted micro-droplets irritate the mucous membrane of the respiratory system, and cause infection (Zeng, Qingliang et al, 2006, p. 113-115).

The environment pollutions resulted from cutting fluids mainly include two aspects as follows: (1) The erratic volatilization, spatter and leakage of cutting fluid during cutting process lead to a drastic environmental deterioration, and severely affect the safety of production; (2) mineral oil-based cutting fluid has a poor biodegradability, and will remain in water and soil for a long time, which causes contamination to lakes, rivers, oceans and underground water. Phosphate, a conventional anti-rust agent, is proved to be responsible for the red tides of lakes and rivers (Li, Chunfeng et al, 2001, p. 15-17).

Ester oil, a substitute for mineral oil, has a biodegradation rate of 90%~100%; however, it is rather expensive. Therefore, the further study on the fully biodegradable cutting fluid of moderate price has become more and more important throughout the world (Asadauskas, S et al, 1996, p. 877-882). Synthetic cutting fluid has advantages of being cheap, fast heat dissipation, being cleanable, excellent visibility in processing, being easy to dilute, high stability and perfect anti-rust ability. In addition, it is free of nutrients that support growth of microorganisms, and prevents the environment from being polluted (Kong Jixia, 2004, p. 49-52). However, the studies on the preparation conditions of base oil for synthetic cutting fluid have been rarely reported. This paper introduces a low-cost method for preparation of environmentally friendly triethanolamine ricinoleate, a base oil that substitutes for mineral oil, investigates the conditions for preparing this base oil, and formulates an environmentally friendly water-based synthetic metal-cutting fluid which is applicable for processing various metals. The above-mentioned base oil has an excellent solubility in

water, and remarkably improves the lubricating ability, extreme pressure, anti-rust property and etc. of the cutting fluid.

1. Experiment

1.1 Materials

Castor acid (CP), from Tianjin Letai Chemical Industry Co., Ltd.; Soybean oil (food grade), from Tianjin Letai Chemical Industry Co., Ltd.; Castor oil (CP), triethanolamine (AR), concentrated sulfuric acid (AR), p-toluene sulphonic acid (AR), hydroquinone (AR), ferrous ammonium sulfate (AR), OP-10 (AR), dimethyl silicone oil (AR), sodium benzoate (AR), sodium gluconate (AR), benzotriazole (AR), and EDTA (AR), all from Tianjin Kermel Chemical Reagent Co., Ltd.

1.2 Preparation of base oil

A reddish brown triethanolamine ricinoleate of excellent water solubility is formulated at 90 ℃ for 150 min with castor acid and triethanolamine at the molar ratio of 1 to 3, p-toluene sulphonic acid as the catalyst, as well as ferrous ammonium sulfate as the polymerization inhibitor. The reaction is expressed by the following equation (1).

(1)
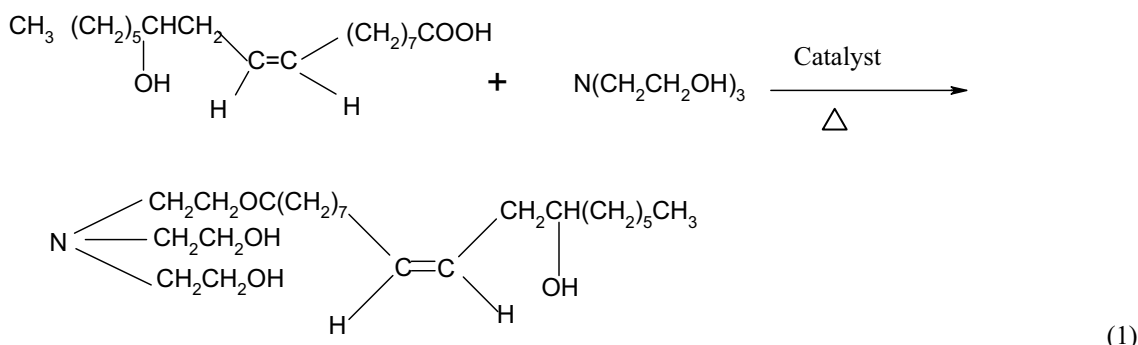
1.3 Formulation design of cutting fluid

The best designed formulation of cutting fluid has been obtained based on the orthogonal experiment of base oil, extreme pressure agent and other additives.

1.4 Measurement of performances of cutting fluid

Measure the performances of the obtained water-based synthetic metal-cutting fluid according to the national standard (GB6144–1985).

2. Results and discussions

2.1 Determination of the best reactants for base oil

Biodegradability of the base oil has a direct effect on that of the obtained cutting fluid. Therefore, the selection of base oil remarkably affects the effects of cutting fluid on the environment. The base oil of cutting fluid includes mineral oil, synthetic oil (synthetic ester and synthetic alkane) and vegetable oil. Mineral oil and synthetic alkane are not proper to be used as the base oil of the environmentally friendly cutting fluid because they are poor at biodegradability, and remain in water and soil for a long time to cause environment pollution; whereas vegetable oil and synthetic ester have good biodegradability. Therefore, in this study, we use castor acid, castor oil and soybean oil to react with triethanolamine respectively, and select a reactant of the best esterification effect to prepare the base oil. The results are shown in table 1.

From table 1, we can see that the product from triethanolamine and castor acid is much better than the other two groups as to the solubility and transparency, as a result, we select triethanolamine and castor acid as the best reactants for preparing the base oil.

2.2 Determination of molar ratio of reactants

Molar ratio of castor acid to triethanolamine has a direct effect on the reaction. Overhigh amount of castor oil leads to incomplete reaction, and has an adverse effect on the esterification; whereas overlow amount of castor oil leads to the waste of triethanolamime. Therefore, a proper molar ratio should be determined. By comparing the transparency, solubility and stability of the product, the paper investigates the effects of different molar ratio of castor acid to triethanolamine on the esterification under the same reaction conditions. Figure 1 exhibits the effects of molar ratio of castor acid to triethanolamine on the transparency of the obtained synthetic ester, and table 2 exhibits the effects of molar ratio of castor acid to triethanolamine on the solubility and stability of the obtained synthetic ester.

From figure 1 and table 2, we can see that the synthetic ester is good at the transparency, solubility and stability when the molar ratio of castor acid to triethanolamine is less than 1:3. In view of the production cost, the molar ratio of castor

acid to triethanolamine is determined to be 1:3.

2.3 Determination of the optimal reaction temperature

Reaction temperature has a certain effect on the performances of the product. Overheat leads to the deterioration of castor acid, whereas overlow temperature results in incomplete reaction. Table 3 exhibits the effect of temperature on the performances of the obtained product.

From table 3, we can see that the reaction is slow and incomplete, and the product is viscous and insoluble when the reaction temperature is lower than 80 ℃; whereas the color of the product is darker and the transparency of the product is lower when the reaction temperature is higher than 130 ℃. Therefore, the reaction temperature should be in the range of 90~120 ℃.

2.4 Determination of the optimal reaction period

Reaction period also has a certain effect on the performances of the product. Overshort reaction period leads to incomplete reaction; whereas, overlong reaction results in more byproducts. Table 4 investigates the effects of reaction period on the stability of the ester at reaction temperature of 90~120 ℃.

From table 4, we can see that the stability of the synthetic ester increases with the reaction going on at low reaction temperature (90~100 ℃); whereas, the stability decreases and large amount of byproducts appear when the reaction temperature is over 110 ℃. In view of the production cost, it is determined to carry out the reaction at 90 ℃ for 150 min.

2.5 Selection of catalyst

For further increase of reaction speed and production efficiency, we investigate the effect of different catalysts on the esterification at the optimal molar ratio, reaction period and reaction temperature (see table 5).

From table 5, we can see that the catalysis effect of p-toluene sulphonic acid is better than that of concentrated sulfuric acid. In addition, concentrated sulfuric acid leads to the increase of byproducts with the reaction going on at high temperature. Therefore, p-toluene sulphonic acid is selected as the catalyst in this study, and its amount is determined to be 0.5%.

2.6 Selection of polymerization inhibitor

Besides the esterification, intermolecular polymerization and intramolecular polymerization also occur. Polymerization inhibitor is used to prevent molecular polymerization. Table 6 reveals the comparison between two polymerization inhibitors.

From table 6, we can see that these two inhibitors have the same effects. However, the water solution of hydroquinone appears reddish when oxidized in air, and affects the visibility of cutting fluid, meanwhile, it sort of has toxicity. Therefore, we select ferrous ammonium sulfate as the polymerization inhibitor in this study.

2.7 Optimal formulation of cutting fluid

Table 7 exhibits the optimal formulation of cutting fluid.

2.8 Measurement of the product quality

Measure the performances of the obtained water-based synthetic metal-cutting fluid according to the national standard (GB6144–1985). Table 8 exhibits the measurement results.

2.9 Comparison with traditional cutting fluid

Generally, traditional cutting fluids contain organic sulfur, chlorine, nitrite and etc that are harmful to the human body and environment, which have severely negative effects on their applications. In addition, mineral oil or synthetic alkane based cutting fluids have poor biodegradability, which further limits the application of traditional cutting fluid. However, synthetic ester-based cutting fluids have advantages of good biodegradability, being cheap, fast heat dissipation, being cleanable, excellent visibility in processing, being easy to dilute, high stability and perfect anti-rust ability, therefore they have bright future in the market. The only fly in the ointment is that the poor lubricating ability of synthetic ester-based cutting fluids limits their broader applications. In this study, the base oil, triethanolamine ricinoleate, is a nonionic surfactant. As a result, it can lower the friction, and increase the lubricating ability of cutting fluid. In addition, sodium gluconate exhibits an excellent synergistic effect with sodium benzoate, even small amount of sodium gluconate can remarkably increase the anti-rust effect of sodium benzoate.

3. Conclusion

A base oil of excellent water solubility, triethanolamine ricinoleate, is formulated at 90 ℃ for 150 min with castor acid and triethanolamine at the molar ratio of 1 to 3, p-toluene sulphonic acid as the catalyst, and ferrous ammonium sulfate as the polymerization inhibitor. An environmentally friendly water-based synthetic metal-cutting fluid is in turn

formulated with this self-made base oil and other additives. The performances of this cutting fluid meet the requirements specified in the national standard GB 6144-1985. The test results indicate that this cutting fluid has good cooling, cleaning, anti-rust, anti-corrosive and lubricating properties, is totally free of mineral oil, animal oil, nitrite that is harmful to the human body, phosphate that causes water pollution and etc., and has stable and reliable quality, long service life, easily available raw materials and low production cost.

References

Asadauskas, S, Perez, J M & Duda, J L. (1996). Oxidative stability and antiwear properties of high oleic vegetable oils. *Lubrication Engineering*, 52, 877-882.

Feng, Jufen, Sun, Daoyan & Liao, Rongsu. (1995). A research on water-soluble cutting fluid. *Journal of Beijing Forestry University*, 17(3), 40-43.

Hou, Bin, Chen, Boshui & Fang Jianhua. (2002). Some ideas about environmentally friendly metal cutting fluids. *Lubrication Engineering*, 4, 37-39.

Kong, Jixia. (2004). Present situation and development of synthetic cutting fluid. *Gaoqiao Petrochemical Corporation*, 19, 49-52.

Li, Chunfeng, Luo Xinmin & Liu Ximei. (2001). Preliminary research of environmental protection cutting fluid. *Synthetic Lubricants*, 28(4), 15-17.

Zeng, Qingliang & Xu Yan. (2006). Study on application of environmentally friendly cutting fluid. *Machine Tool & Hydraulics*, 7, 113-115.

Table 1. The selection of base oil

Reactant	Triethanolamine + castor acid			Triethanolamine + castor oil			Triethanolamine + soybean oil		
Reaction temperature (℃)	120	140	160	120	140	160	120	140	160
Solubility*	++	+	+-	--	--	--	--	--	+-
Transparency**	100%	50%	20%	——	——	——	——	——	100%

* Solubility is classified into 5 grades, and expressed as ++, +, +-, - and – in order from fully soluble to insoluble.

** In 2% water solution, transparency is expressed with a percentage from 100% to 1% in order from transparent to milky, and 0 represents the transparency when the synthetic ester is insoluble.

Table 2. The effects of molar ratio on the solubility and stability of the obtained synthetic ester

Molar ratio of castor acid to triethanolamine	1:1	1:1.2	1:1.4	1:1.6	1:1.8	1:2	1:2.5	1:3	1:4
Solubility	--	--	-	+-	+	+	++	++	++
Stability	——	——	——	30 min	1 h	2 h	4 h	F+	F+

F+ represents that the obtained synthetic ester stays stable for a long time.

Table 3. The effects of reaction temperature on the performances of the obtained synthetic ester

Reaction temperature (℃)	80	90	100	110	120	130	140
Solubility	+	++	++	++	++	+	+
Transparency	100%	100%	100%	100%	100%	80%	50%

Table 4. The effects of reaction period on the stability of the obtained synthetic ester at different reaction temperature

Reaction temperature (℃)	Reaction period (min)							
	30	60	90	120	150	180	210	240
90	2 d	2 d	3 d	4 d	F+	F+	F+	F+
100	2 d	2 d	3 d	4 d	F+	F+	F+	F+
110	2 d	2 d	2 d	2 d	1 d	1 d	1 d	1 d
120	30 min	50 min	60 min	60 min	60 min	60 min	60 min	60 min

F+ represents that the obtained synthetic ester stays stable for a long time.

Table 5. The effects of different catalysts on the performances of the obtained synthetic ester

Catalyst	p-toluene sulphonic acid (0.5%)	p-toluene sulphonic acid (1.0%)	Concentrated sulfuric acid (0.5%)	Concentrated sulfuric acid (1.0%)
Solubility	++	++	+-	--
Transparency	100%	100%	30%	0

Table 6. The comparison between two polymerization inhibitors

Polymerization inhibitors	Solubility	Transparency	Stability
Hydroquinone	++	80%	F+
Ferrous ammonium sulfate	++	100%	F+

Table 7. The formulation of cutting fluid

Triethanolamine ricinoleate	20%
OP-10	1%
Extreme pressure agent	15%
Dimethyl silicone oil	1%
Sodium benzoate	0.5%
Sodium gluconate	0.5%
Benzotriazole	1%
EDTA	A little
Deionized water	Margin

Table 8. The measurement of performances of the obtained cutting fluid

| Measured performances		Quality index		Test method
Concentrated fluid	Appearance	Transparent solution		GB6144—85
	Storage stability	Qualified		GB6144—85
5% solution of ionized water	Transparency	Transparent		GB6144—85
	pH	8~9		GB6144—85
	Defoaming property	Qualified		GB6144—85
	Surface tension	0.031 dyn/cm		GB6144—85
	Anti-corrosion (55±2 ℃)	Grey cast iron	Grade A	GB6144—85
		Red copper	Grade A	GB6144—85
		LY12 Aluminum	Grade A	GB6144—85
	Anti-rust	Single layer	Grade A	GB6144—85
		Laminated layer	Grade A	GB6144—85
	Maximum non-seizure load (PB)	≤150 kg		GB6144—85
	Compatibility with the machine paint	Qualified		GB6144—85
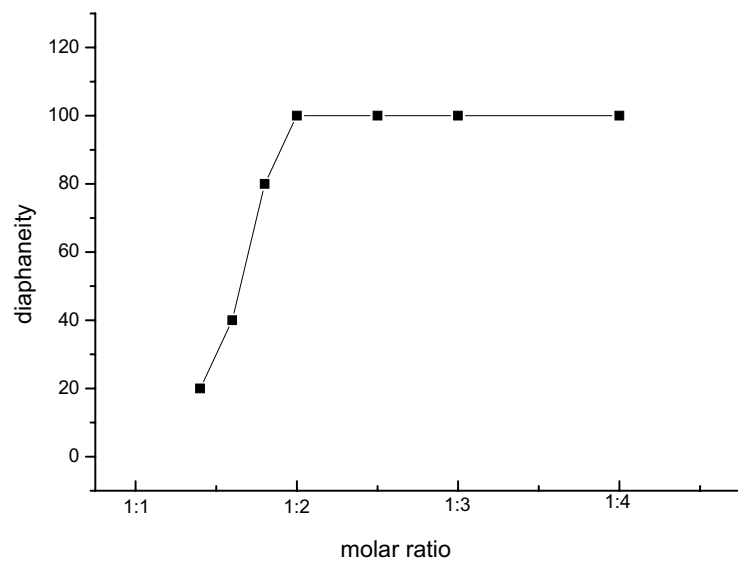
Figure 1. The effect of molar ratio of castor acid to triethanolamine on the transparency of the obtained synthetic ester

Zn/ZnO/TiO$_2$ and Al/Al$_2$O$_3$/TiO$_2$ Photocatalysts

for the Degradation of Cypermethrin

Rusmidah Ali, Wan Azelee Wan Abu Bakar & Lee Kin Teck

Department of Chemistry, Faculty of Science

Universiti Teknologi Malaysia

81310 UTM Skudai, Johor, Malaysia

Tel: 60-13-746-6213   E-mail: rusmidah@kimia.fs.utm.my

Abstract

The aim of the present study is to investigate the activity of semiconductor materials on the degradation of pesticides cypermethrin under UV-light (6 W, λ = 354 nm). Three types of photocatalysts were prepared namely Zn/ZnO, Zn/ZnO/TiO$_2$ and Al/Al$_2$O$_3$/TiO$_2$. Zn/ZnO film was prepared by anodic oxidation of zinc in NaOH with various concentrations (0.2, 0.3, 0.4, and 0.5 M) at 12 V for 20 minutes. The best concentration for NaOH is 0.5 M and the best applied voltage in the preparation of Zn/ZnO is 12 V. The Al/Al$_2$O$_3$ film was prepared by anodizing aluminium plate in H$_2$SO$_4$ at 12 V for 60 minutes. TiO$_2$ films were electrodeposited onto Zn/ZnO and Al/Al$_2$O$_3$ by electrolysis technique in (NH$_4$)$_2$[TiO(C$_2$O$_4$)] solution at 12 V for 20 minutes. Zn/ZnO/TiO$_2$/UV shows the highest photocatalytic degradation of cypermethrin compared to the other photocatalytic system. The effects of some operational parameters such as pH and oxidizing agent (H$_2$O$_2$) on the degradation efficiency of the semiconductor were also studied. The optimum pH for the photodegradation of cypermethrin using Zn/ZnO is pH 5. In the presence of H$_2$O$_2$ as the oxidizing agent, the overall reaction is significantly reduced due the scavenging effect of H$_2$O$_2$. The surface morphology of the catalyst was studied by FESEM analysis.

Keywords: Zinc oxide, Titanium dioxide, Anodic oxidation, Photodegradation, Cypermethrin

1. Introduction

The used of chemical in agricultural activity to increase the production is a common phenomenon. This activity, however, will generate residues that can be noxious to the environment. Cypermentrine is a common active chemical in household and outdoor insecticides, also used as pesticides for the bovine ticks control. The used of cypermentrine will produce hundreds of liters of residual solution, which could be indiscriminately discarded the water system and should be treated.

Photocatalytic degradation has been proven to be a promising method treating water contaminated with organic and inorganic pollutants, including pesticides [Devipriya and Yeshodharan, 2005]. The term photocatalysis is defined as a catalytic reaction involving light adsorption by a catalyst or a substrate.

TiO$_2$ is a promising material as a photocatalyst for the photodecomposition reactions and is widely used for water treatment processes. Recently, various preparation and fixation methods for TiO$_2$ had been reported   [Ishikawa and Matsumoto, 2002]. Several practical problems arising from the use of TiO$_2$ powder are obvious during or after photocatalytic processes. Thus, an alternative form of TiO$_2$ has been reported. TiO$_2$ thin film has been successfully used for the photocatalytic degradation of organic compounds [Andronic and Duta, 2007]. There are several of preparation methods to obtain TiO$_2$ thin films, including spray coating, spin coating, chemical vapour deposition, sol-gel and electrodeposition method. Electrodeposition is a low-cost electrochemical method in which TiO$_2$ photocatalyst is directly deposited on the metal oxide substrate [Ishikawa and Matsumoto, 2001].

Although TiO_2 is the most commonly used photocatalyst, ZnO is found to be a suitable alternative to TiO_2 since ZnO has the same band gap energy and similar photodegradation mechanism as TiO_2 (Equation 1 – 5) [Yamaguchi et al., 1997]. TiO_2 anatase band gap energy is 3.2 eV while ZnO band gap energy is 3.17 eV. Superoxide anion radicals ($\bullet O_2^-$) and hydroxyl radicals ($\bullet OH$) generated (Equation 2-3) in the aqueous medium are responsible in accelerating the oxidation of pollutants [Mills and Hunte, 1997 and Vidal et al., 1999].

$$Semiconductor + h\nu \longrightarrow e^- + h^+ \tag{1}$$

$$O_2 + e^- \longrightarrow \bullet O_2^- \tag{2}$$

$$H_2O + h^+ \longrightarrow \bullet OH + H^+ \tag{3}$$

$$OH^- + h^+ \longrightarrow \bullet OH \tag{4}$$

$$\bullet OH + H^+ \longrightarrow \bullet OH_2 \tag{5}$$
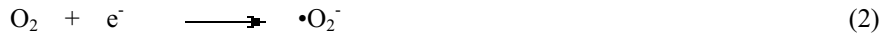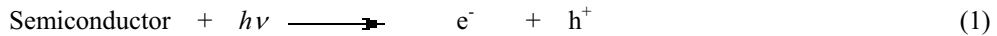
Under certain conditions, ZnO has been reported to be more effective than TiO_2. However, the photocorrosion of ZnO which frequently occurs when the photocatalyst is illuminated under UV-lights decreases its photocatalytic activity in the aqueous solutions [Yamaguchi et al., 1997].

The photocatalytic efficiency of the photocatalysts can be enhanced by coupling the ZnO with TiO_2 [Yang and Swisher, 1996]. The coupling of two semiconductors provides a novel approach to the enhancement of photocatalytic activity. Recent, studies had shown that binary oxides can provide a more efficient charge separation, increased lifetime of charge carriers and enhanced interfacial charge transfer to absorbed substrates [Wang et al., 2002]. Studies had been conducted on the photocatalytic activity using the binary semiconductor oxide system such as TiO_2/SnO_2, TiO_2/ZrO_2, TiO_2/MoO_3, TiO_2/CdS, TiO_2/Fe_2O_3, TiO_2/WO_3, CdS/ZnO, CdS/AgI, and ZnO/ZnS [Wang et al., 2002, Liao et al., 2004 and Liao et al., 2008].

Liao *et al.* (2004) studied the preparation and photocatalytic activity of the binary oxide photocatalyst ZnO/TiO_2 in the degradation of methyl orange dye. It was shown that the addition of ZnO enhanced the photocatalytic activity of TiO_2 significantly.

This paper covers the degradation reaction of cypermethrin using electrodeposition coated TiO_2 photocatalysts. The photocatalysts were characterized using X-Ray Diffraction (XRD) and Field Emission Scanning Electron Microscopy (FESEM) technique. The photodegradation of cypermethrin was conducted in the presence of UV-light and monitored by UV-Visible spectroscopy. Degradation process is the process of breaking organic molecules into smaller molecules which will further mineralize into minerals such as NO_3^-, PO_4^{3-}, CO_3^{2-}, depending on the elements present in the molecule.

2. Experimental

2.1 Anodic deposition of ZnO thin film on zinc sheet.

The ZnO thin film was prepared by modification of Yamaguchi's method [Yamaguchi et al.,1997]. A zinc sheet (50 x 60 x 0.38 mm) was used as the substrate for anodizing. The surface was scrubbed by sandpaper and etched by immersing in 0.1 M NaOH for 3 minutes and followed by washing in distilled water. The zinc plate was set as the anode while a graphite plate was set as the cathode and both plates were placed at a distance of 50 mm for one another in NaOH aqueous solution (0.2, 0.3, 0.4, 0.5 M). A DC voltage (12 V) was applied for 20 minutes using a constant voltage power supply of PL Regulated 303 DC. The plate obtained was referred as Zn/ZnO. The plate prepared using 0.2, 0.3, 0.4 and 0.5 M NaOH was denoted as Z02, Z03, Z04 and Z05 respectively.

A similar procedure was repeated using aluminium plate and replacing the NaOH with 3.0 M H_2SO_4. The alumite plate obtained was referred as Al/Al_2O_3.

2.2 The preparation of TiO_2 thin film on zinc oxide substrate by electrodeposition process.

TiO_2 was electrodeposited into the pores of Zn/ZnO ($Zn/ZnO/TiO_2$) by alternative electrolysis in a mixed aqueous solution containing $(NH_4)_2[TiO(C_2O_4)_4]$ (1×10^{-2} M) and $(COOH)_2$ (2.5×10^{-3} M) which was adjusted to pH 4 by titration with NH_4OH, under a DC voltage (12 V) for 20 minutes. The distance between the cathode (Zn/ZnO) and anode (graphite) was fixed at 50 mm. The plate obtained was referred as $Zn/ZnO/TiO_2$ (Z05T). The process adjusted was a modification of Ishikawa's method [Ishikawa and Matsumoto, 2001 and Ishikawa and Matsumoto, 2002].

A similar procedure was repeated using alumite plate, Al/Al_2O_3. The plate obtained was referred as $Al/Al_2O_3/TiO_2$ (A3T).

2.3 Photodegradation of cypermethrin using prepared photocatalysts.

The photocatalytic activity of the prepared Zn/ZnO, $Zn/ZnO/TiO_2$ and $Al/Al_2O_3/TiO_2$ catalysts were determined by the photodegradation of cypermethrin.

Cypermethrin with a concentration of 1.0×10^{-3} M (5 mL) was pipetted into a square pyrex reactor and 45 mL of distilled water was added to dilute the sample solution to 1.0×10^{-4} M. The solution was then stirred with magnetic stirrer for 10 minutes. The Zn/ZnO plate was then dipped into the sample. An Ultra Violet lamp (6 W, 354 nm) was used as the light source in this experiment.

For the first 90 minutes, the sample was allowed to be adsorbing on the surface of the catalyst support. Within this period, 3 mL of the sample was taken out using syringe at 0, 30, 60 and 90 minutes. Then, the sample was irradiated with UV lamp for the next 3 hours. Sample was taken out at 30, 60, 90, 120, 150 and 180 minutes and analyzed using Shimadzu 2510PC UV/Visible spectrophotometer. The percentage of degradation was calculated using Equation 6.

$$\% \text{ Degradation} = (A_o - A_t)/A_t \times 100 \tag{6}$$

where,

A_o = initial absorption

A_t = absorption at time, t.

3. Results and Discussion

3.1 Optimization of the NaOH Concentration for the Preparation of Zn/ZnO

The optimum NaOH concentration was determined from the photocatalytic activity of the prepared catalysts. A plot of the percentage degradation as a function of time is shown in Figure 1. The percentage degradation of cypermethrin is seen to increase upon irradiation of UV-light. Zn/ZnO prepared with the highest concentration of NaOH (Z05) gives 67.5% degradation indicating the highest percentage of cypermethrin degradation as shown in Figure 1. Thus, 0.5 M NaOH is considered the most suitable concentration in the preparation of Zn/ZnO photocatalyst.

3.2 Photolysis and Photocatalytic Degradation of Cypermethrin

The degradation of cypermethrin by photolysis and photocatalysis is shown in Figure 2. Cypermethrin in the aqueous solution was treated under UV-light alone and in the presence of Zn/ZnO as the photocatalyst. Photodegradation in the absence of Zn/ZnO gives lower degradation of cypermethrin (47.4%) within 270 min. In contrast, 67.5% cypermethrin is photodegraded within 270 min in the presence of Zn/ZnO. These experimental results demonstrate that the direct photolysis has improved by the presence of heterogeneous photocatalyst. The photocatalyzed degradation of organic matter in aqueous solution is initiated by the photoexcitation of the semiconductor, followed by the formation of high energy states of electron-hole pair on the surface of the catalyst which can further provide a powerful oxidative species such as the hydroxyl radical. This strong oxidizing ●OH radical can promote the mineralization of organic matter [Daneshvar et al., 2007].

3.3 The Effect of Initial pH value

Figure 3 shows the effect of initial pH value on the photocatalytic degradation of cypermethrin in the presence of Z05. In neutral or acidic aqueous solution, cypermethrin hydrolyzes slowly, with hydrolysis being more rapid at pH 9 [International Programme on Chemical Safety,1989]. However, the results show that the percentage of cypermethrin degradation at pH 2 (49.3%), due to photocorrosion is higher than pH 12 (23.9%). Cypermethrin is photodegraded the most at pH 5 (69.1%) which is the original initial pH of the sample solution. At a pH lower than 4, ZnO undergoes photocorrosion through self-oxidation and tends to dissolve in the acidic solution. Moreover, upon irradiation under UV light, there is a higher possibility for the formation of photocatalytically inert $Zn(OH)_2$ compound on the surface layers of the catalyst that will cause surface passivation which will deactivate the photocatalytic activity.

3.4 The Effect of Hydrogen Peroxide

The effect of H_2O_2 had been investigated in numerous studies and is observed to increase in the photodegradation rate of organic hazard pollutants. Even though H_2O_2 is a strong oxidant, it decreases the photodegradation rate of cypermethrin as shown in Figure 4. This is probably due to the scavenging effect of H_2O_2 which can reduced the production of •OH in the solution [Daneshvar et al., 2007]. It is proven that the presence of hydroxyl radical exceeding the optimum amount could lead to the recombination of the radicals forming water [International Programme on Chemical Safety,1989].

3.5 The Photocatalytic Activity of Zn/ZnO, Zn/ZnO/TiO$_2$ and Al/Al$_2$O$_3$/TiO$_2$

A comparative study was conducted to investigate the photocatalytic activity of Zn/ZnO (Z05), Zn/ZnO/TiO$_2$ (Z05T) and Al/Al$_2$O$_3$/TiO$_2$ (A3T) in the degradation of cypermethrin. The results are shown in Figure 5. Z05T gives the highest percentage of degradation compared to Z05 and A3T where 75.3% of cypermethrin is degraded under irradiation of UV-light. The binary catalyst, Zn/ZnO/TiO$_2$ has performed better on degrading cypermenthrin compared to single catalyst Zn/ZnO. According to the experimental results, it can be demonstrated that the binary oxide provides more active sites and thus enhances the photocatalytic activity, compared to ordinary oxide.

The photocatalytic activity can be explained through inter-particle electron transfer pathway (IPET) of the binary semiconductor [Serpone et al., 1995]. The higher photocatalytic activity of $Zn/ZnO/TiO_2$ can be related to the roles of electrons and holes of the catalyst which can possess different redox energy levels for their corresponding conduction and valence bands [Serpone et al., 1995 and Michaelis et al., 2006]. In $Zn/ZnO/TiO_2$, the electron transfer occurs from the conduction band of the photo-activated ZnO to the conduction band of photoactivated TiO_2 and conversely. The holes move in the opposite direction from the electron. This vectorial displacement of electrons and holes provides a more efficient charge separation and increases the charge carrier's lifetime. Thus the recombination of electron and holes in this catalyst can be greatly suppress and the efficiency of the interfacial charge transfer between the adsorbed substrate and catalyst can be enhanced [Liao et al., 2008 and Zhang et al., 2004].

A3T is even less effective on the photocatalytic of cypermenthrin which give only 60.4% degradation in the UV-induced degradation process compared to the other two catalysts. The experimental results indicate that TiO_2 works more effectively in the UV-induced degradation of these pesticides.

Aal *et al.* (2008) demonstrated that the noble binary oxide, TiO_2/ZnO is more effective in promoting the degradation of 2-chlorophenol compared to pure ZnO. Moreover, the addition of ZnO as a substrate could enhance the activity of TiO_2 significantly [Liao et al., 2004]. Chu (2007) had investigated on the photodegradation of 4-nitrophenol and chlordance using Zn/ZnO and $Zn/ZnO/TiO_2$ photocatalysts and reported that binary metal oxide is more efficient.

3.6 Characterization of Photocatalyst

Figure 6 illustrates the FESEM images for Z04, Z05 and Z05T. The surface morphology of Z04 film shows a clear roughness associated to the presence of cavities and protuberances. In contrast, a clear open porous structure is observed in Z05 film, thus exhibits a much larger specific surface area than Z04 film. Therefore, the highest result in UV-induced degradation of cypermethrin of Z05 can be explained by this observation. The morphological properties of anodic ZnO layer can be correlated with the concentration of NaOH electrolyte solution in the electrodeposition process. As can be seen from Figure 6 (c), Z05T give a much higher open porous structure compared to Z05 photocatalyst. The increased in porosity will increase the specific surface area.

3.7 Elemental Analysis: Electron Dispersive X-Ray Analysis (EDX)

Figure 7 shows the EDX spectrum of Z05 photocatalyst. From the spectrum, it is observed that only two elements, Zn and O are present in the Z05 film. All elements present in the Z05 film are tabulated in Table 1.

The composition of element present in $Zn/ZnO/TiO_2$ (denoted as Z05T) is also detected using EDX analysis. The EDX spectrum of Z05T is illustrated in Figure 8. As can be seen from the EDX spectrum, an additional element is present in the Z05T which is titanium (Ti) element. The composition percentage for all elements present in Z05T is tabulated in Table 2. The existence of carbon may possibly come from graphite which is used as the cathode in the catalyst preparation.

4. Conclusion

Zn/ZnO, $Zn/ZnO/TiO_2$ and $Al/Al_2O_3/TiO_2$ photocatalyst systems were successfully synthesized in this study. Zn/ZnO cannot be used either in the acidic or in the basic conditions. Higher efficiency of photocatalytic degradation of cypermethrin is achieved at pH 5. The presence of high concentration of H_2O_2 which act as scavenger consequently reduced the efficiency of the photocatalyts. $Zn/ZnO/TiO_2/UV$ shows the highest photocatalytic efficiency compared to other system in the degradation of cypermethrin.

References

Aal, A. A., Barakat, M.A. and Mohamed, R.M. (2008). Electrophoreted Zn–TiO$_2$–ZnO nanocomposite coating films for photocatalytic degradation of 2-chlorophenol. *Appl. Surf. Sci*. Article in press.

Andronic, L. and Duta, A. (2007). TiO$_2$ Thin Films for Dyes Photodegradation.*Thin Solid Films*. 515: 6294–6297.

Chu, C. L. (2007). The preparation of titanium dioxide deposited onto alumite and zinc oxide catalysts for chlordance and 4-nitrophenol photodegradation. Universiti Teknologi Malaysia. B. Sc. Thesis.

Daneshvar, N., Aber, S., Seyed, M.S., Dorraji, Khataee, A.R., and Rasoulifard, M.H. (2007). Photocatalytic Degradation of the Insecticide Diazinon In The Presence of Prepared Nanocrystalline ZnO Powders Under Irradiation of UV-C Light. *Sep. Pur. Technol*. 58: 91-98.

Devipriya, S. and Yeshodharan, S. (2005). Photocatalytic Degradation of Pesticide Contaminants in Water. *Sol. Energy Mater. Sol. Cells*. 86: 309-348.

International Programme on Chemical Safety. (1989). *Environmental Health Criteria 82: Cypermethrin*. Geneva: World Health Organization.

Ishikawa, Y. and Matsumoto, Y. (2001). Electrodeposition of TiO_2 photocatalyst into nano-pores of hard alumite. *Electrochim. Acta.* 46: 2819–2824.

Ishikawa, Y. and Matsumoto, Y. (2002). Electrodeposition of TiO_2 photocatalyst into porous alumite prepared in phosphoric acid. *Solid State Ionics* .151: 213– 218.

Liao, D.L., Badour, C.A. and Liao, B.Q. (2008). Preparation of nanosized TiO_2/ZnO composite catalyst and its photocatalytic activity for degradation of methyl orange. *J. Photochem. Photobiol., A: Chem.* 194: 11–19.

Liao, S., Huang, D., Yu, D., Su, Y. and Yuan, G. (2004). Preparation and Characterization of ZnO/TiO_2, SO_4^{2-}/ZnO/TiO_2 photocatalyst and Their Photocatalysis. *J. Photochem Photobiol., A: Chem.* 168: 7-13.

Michaelis E., Wohrle, D., Rathousky, J. and Wark, M. (2006). Electrodeposition of porous zinc oxide electrodes in the presence of sodium laurylsulphate. *Thin solid films*. 497: 163-169.

Mills, A. and Le Hunte, S. (1997). "An overview of semiconductor photocatalysis" *J. of Photochem. and Photobiol. A: Chemistry*, 108. 1-35.

Serpone, N.P., Maruthamuthu, P., Pelizezetti, E. and Hidaka, H. (1995). Exploiting the interparticle electron transfer process in the Photocatalyzed oxidation of phenol. 2-chlorophenol and pentachlorophenol: Chemical evidence for electron and hole transfer   between coupled semiconductors. *J. Photochem. Photobiol., A: Chem.* 85: 247-255.

Vidal, A., Dinya, Z., Mogyorodi Jr., F. and Mogyorodi, F. (1999). "Photocatalytic of thiocarbamate herbicide active ingredients in water." *Applied Catalyst B: Environ.*. 21. 259–267.

Wang, C., Zhao, J., Wang, X., Mai, B., Sheng G., Peng P. and Fu J. (2002). Preparation, characterization and photocatalytic activity of nano-sized ZnO/SnO_2 coupled photocatalysts. *Appl. Catal., B: Environ*. 39: 269–279.

Yamaguchi, Y., Yamazaki, M., Yoshihara, S. and Shirakashi, T. (1997). Photocatalytic ZnO Films Prepared by Anodizing. *J. Electroanal. Chem.* 442: 1-3

Yang, J. and Swisher, J.H. (1996). "The phase stabilization of $Zn_2Ti_3O_8$." *Material Characterization*. 37. 153-159.

Zhang M., An, TO., Hu, X., Wang, C., Sheng, G. and Fu, J. (2004). Preparation and photocatalytic properties of a nanometer ZnO-SnO_2 coupled Oxide. Appl. Catal., A: Gen. 260: 215-222.

Tables and Figures

Table 1. The weight percentage of elements analyzed by EDX for Z05 photocatalyst

Element	Weight (%)
O	20.87
Zn	79.13
Totals	**100.00**

Table 2. The weight percentage of elements analyzed by EDX for Z05T photocatalyst

Element	Weight (%)
C	2.99
O	34.68
Ti	15.75
Zn	46.58
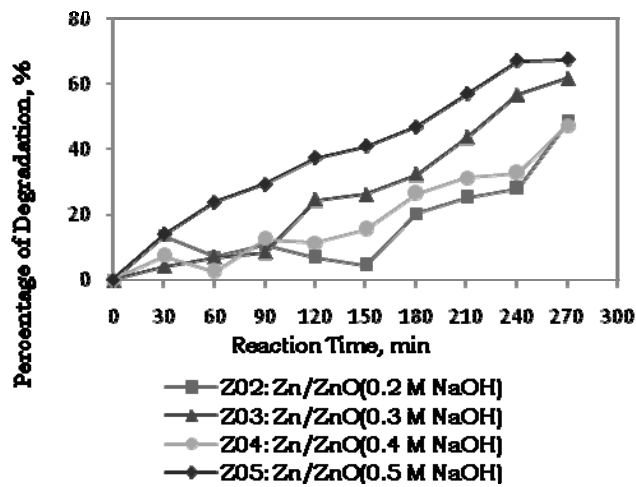
Figure 1. Percentage photodegradation of cypermethrin using Z02, Z03, Z04 and Z05 photocatalysts, UV (λ=254 nm), irradiated for 4 1/2 hours
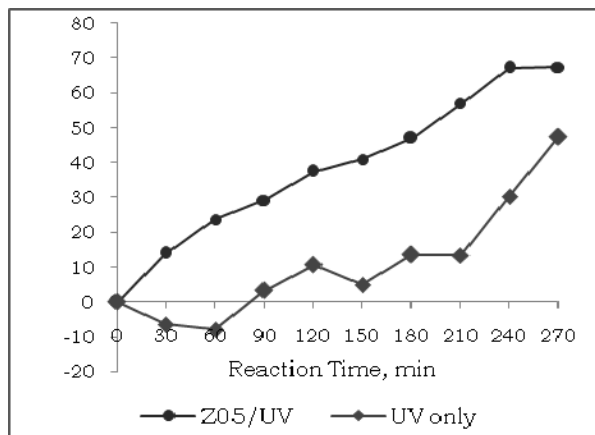
Figure 2. The degradation of cypermethrin by photolysis and photocatalysis under UV (λ=254 nm), irradiated for 4 1/2 hours.
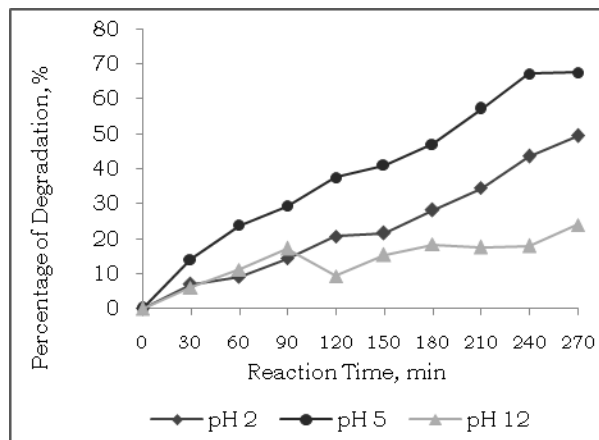
Figure 3. Effect of initial pH on the photocatalytic degradation of cypermethrin,
using Z05 catalyst, UV (λ=254 nm), irradiated for 4 1/2 hours
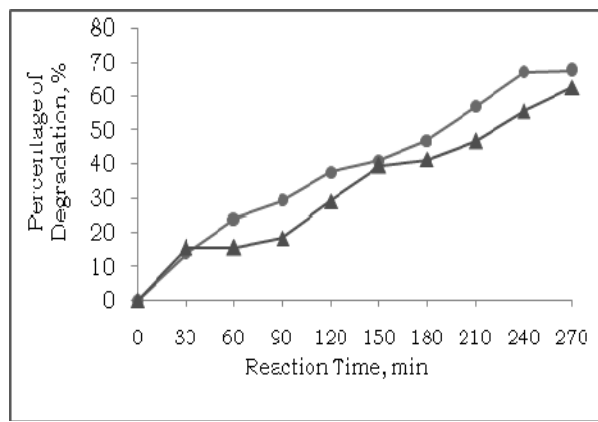
Figure 4. The effect of hydrogen peroxide on the photocatalytic degradation of cypermethrin,
using Z05 catalyst, UV (λ=254 nm), irradiated for 4 1/2 hours.
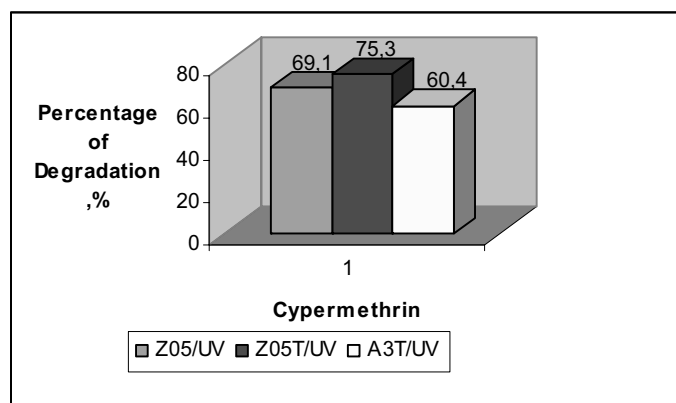
Figure 5. The percentage degradation of cypermethrin using Z05, Z05T and A3T catalysts,
UV (λ=254, nm), irradiated for 4 1/2 hour

(a)   (b)

(c)
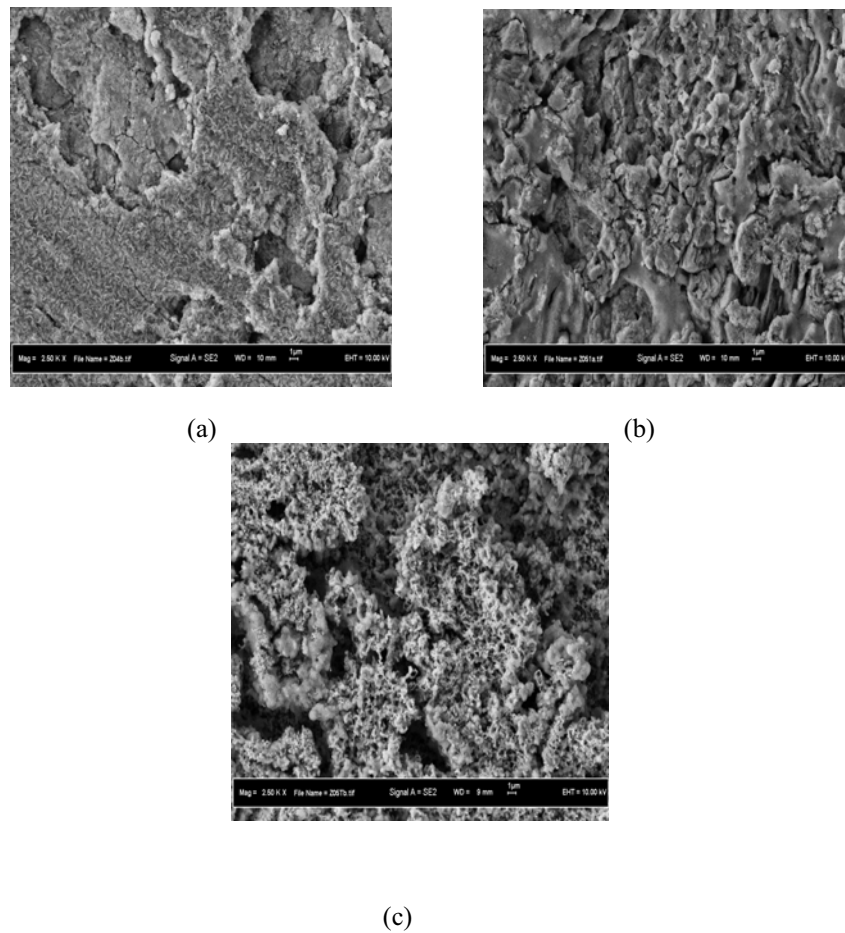
Figure 6. The FESEM images of (a) Z04, (b) Z05, (c) Z05T at 2.5K magnification, 1 cm = 1 μm
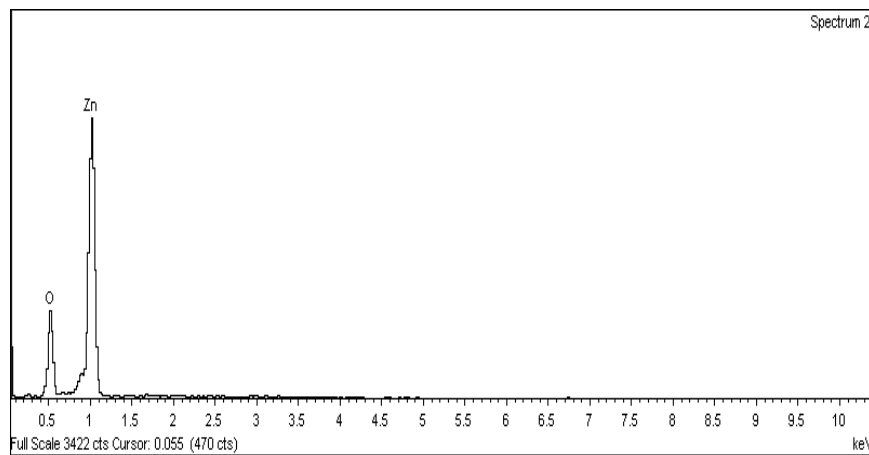

Figure 7. EDX spectrum of Z05 photocatalyst
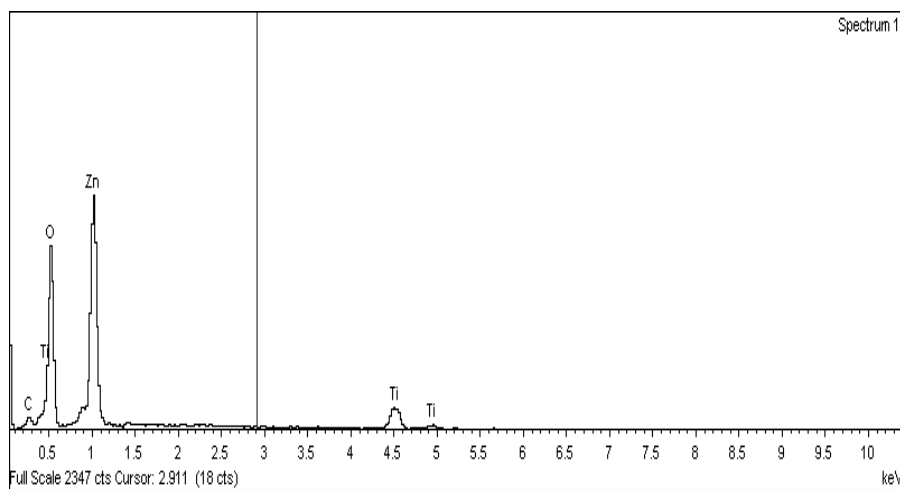
Figure 8. EDX spectrum of Z05T photocatalyst

Research on Evaluation of Technological Innovation Ability about Guangxi Non-Ferrous Metal Industry based on RBF Neural Network

Peng Liu, Jun Hong & Xin Wang

School of Electrical Engineering, Guangxi University

100 Da Xue Road, Nanning 530004, Guangxi, China

Lan Huang

Guangxi Electric Power Institute of Vocational Training

39 Keyuan Road, Nanning 530007, Guangxi, China

Abstract

This paper made an analysis about advantage and disadvantage of Guangxi non-ferrous metal industry. Based on the RBF neural network model, the paper then gave an evaluation of technological innovation ability about non-ferrous metal industry in Guangxi. And then, the paper proposed some suggestions how to better develop non-ferrous metal industry in Guangxi.

Keywords: Non-ferrous metal industry, Technological innovation ability, RBF neural network mode**l**

1. Introduction

Non-ferrous metals industry (short for NFMI) is one of Chinese pillar industries in national economy. In Guangxi, NFMI has played an important part in promoting economic growth and is been cultivated as one of hundred billion dollars industries. With the western development strategy and open development strategy of the northern Gulf Economic Zone in Guangxi, NFMI in Guangxi has entered a new period of rapid development.

Technological innovation is an inexhaustible motive force of industry development. Effective technological innovation about non-ferrous metal industries in Guangxi could improve resource utilization ratio and economical benefit. The improvement of technological innovation would be built on scientific evaluation.

Artificial neural network which could imitate human brain to process data and information is suited to analysis and processing of complex information. This paper tried to evaluate technological innovation ability with this theory.

2. The current situation of NFMI in Guangxi

2.1 The developing situation of NFMI in Guangxi

Guangxi has rich resources of non-ferrous metal. There are 115 kinds of minerals discovered, in which 89 kinds have been known reserves, including manganese, tin, bauxite, tungsten, antimony, zinc, indium and other 20 kinds of minerals. These resources have concentrated distribution and good quality. For example, bauxite is the only one in China which can be used to produce aluminum oxide by pure Bayer's method in Guangxi. The resources of tin, antimony, indium, rare earths in Guangxi are well-known all over the world except the resource of bauxite.

The production of non-ferrous metal industry in Guangxi has developed at the speed of 12.6% per year over the past 50 years, and the growth rate reached to 18.7% per year after reform and opening up in China. Now the non-ferrous metal industry in Guangxi can produce 450,000 tons of alumina, 200,000 tons of electrolytic aluminum, 170,000 tons of electrolytic zinc, 150,000 tons of zinc oxide, 100 tons of indium, 35,000 tons of tin and 50,000 tons of aluminum every year.

2.2 The current situation of technological innovation about NFMI in Guangxi

There are 246 non-ferrous metal enterprises and 39 large and medium non-ferrous metal enterprises in Guangxi. Guangxi government expands science and technology R&D input in order to change non-ferrous metal resources into local economic advantages. In 2007, expenditures of science and technological activities about non-ferrous metal

industry in Guangxi amounted to 296.94 million Yuan which increased 42.35 percent. There were 5857 engineering and technology people, increased 27.9%, and 665 R & D people, increased 8.13%. The number of patents was 28 compare with 21 in 2006, and industrial labor productivity was 320.5 thousand Yuan per person, increased of 122.2 thousand Yuan compared with 2006.

"The Decision of Three-year (2008-2010) Plan about Scientific Development in Guangxi" pointed out: We should give priority to the development of key competitive industries, extend industry chain, and enhance industrial concentration. We would pay main attention on the development of food-processing industry, non-ferrous metal industry, automobile industry, petroleum chemical industry, metallurgical industry, machining industry and power industry. The goal is that the sales income of every industry is more than 100 billion Yuan every year in near future." Currently, the Research Center of indium antimony tin has been established and a new industrial area which has 3333 hectares (500 acres) is being built by Huaxi Group. Guangxi also has a steel industry, a state quality inspection center of indium and a standard warehouse and electronic trading platform of indium in LiuZhou.

3. Artificial neural network evaluation models

3.1 The evaluation indexes

"The analysis report about ability of independent innovation of Chinese enterprises" which was proposed by Economic Situation Monitoring Center of National Bureau of Statistics in 2006, pointed out the evaluation indexes of technological innovation. This paper combined with these evaluation indexes and the general process of technological innovation, and then proposed new evaluation indexes including input of technological innovation, output of technological innovation and marketing of technological innovation.

The evaluation indexes of technological innovation ability about Non-ferrous metal industry are divided into three levels, which contain 10 sub-factors, as shown in Table 1.

3.2 The model

RBF (Radial Basis Function) model is a kind of artificial neural network, which can achieve quick calculation and zero error.

(1) Data standardization

In order to eliminate the different dimensionless of data and fix data in the same interval, we can accomplish data standardization of sample data and target data through formula $x = (x_j - x_{jmax})/(x_{jmax} - x_{jmin})$, where variable x means standardized data, variable x_j means the exact value of simple in column j, x_{jmax} means the maxima and x_{jmin} means minima.

(2) RBF network training

In the Matlab7.0 environment, we accomplish the network training of standardized data through procedure net = newrb(x, y).

(3) Network simulation

In the Matlab7.0 environment, we obtain the evaluation results y' through procedure y'= sim (net, x'), where x' means training data, net means the name of trained network. We can also analyze the results by outputting weights.

4. Evaluation and suggestions

4.1 The evaluation of technological innovation ability about Guangxi's NFMI

This paper collected sample data on non-ferrous metals industry to train the network (data source: "China Statistical Yearbook 1999-2007"), and then collected relevant statistics on non-ferrous metal industry in Guangxi in 2007 as target data (data source: "2008 Guangxi Statistical Yearbook"). We accomplished data standardization through formula $x = (x_j - x_{jmax})/(x_{jmax} - x_{jmin})$, as shown in Table 2, in which the target values of training samples were given by experts according to five levels.

In the Matlab7.0 environment, we firstly train RBF neural network through procedure net = newrb (x, t, 0.001, 0.1, 11, 1) (error: 10^{-3}, which is shown as Figure 1). Then we use the trained network net to test sample data through procedure y = sim (net, x1), where x1 means test sample data, evaluation results is given by y(y= 2.45). At last, we obtain the weights through procedure w1 = net. iw (1, 1) and w2 = net. lw (2, 1), as shown in Table 3. In Table 3, Wi means weight of each index, row CHN is the calculated result of weight value, and row GX is the conclusions of previous studies.

4.2 The analysis of evaluation results

As shown in Table 2, the evaluation result is given by y(y=2.45), which is less than the mean value of nation's NFMI (4.69). Therefore, technological innovation ability about non-ferrous metals industry in Guangxi is at a medium, lower than the standard of nation. Contrasting the weight of indexes from Table 3, we could know that there is some superiorities and inferiority of technological innovation ability about non-ferrous metals industry in Guangxi as

following.

(1) A. input of technological innovation funds

Inequality W1 (CHN)> W1 (GX) which is given by the weight value of A1, means non-ferrous metals industry has a lower input of research and development funds about non-ferrous metals industry in Guangxi. Approximately W2 (CHN) equals W2 (GX), which is given by the weight value of A2, means there are many non-ferrous metals enterprises in Guangxi. Inequality W3 (CHN)>>W3 (GX), which is given by the weight value of A3, means that the proportion of research and development personnel is too small to reach the national level.

(2) B. output of technological innovation

Inequality W4 (CHN)> W4 (GX) which is given by the weight value of B1, means new products have a low production and non-ferrous metals enterprises in GungXi could not get more economical Benefit from technological innovation. Inequality W5 (CHN)> W5 (GX) which is given the weight value of B2, means non-ferrous metals enterprises in GungXi do have less core technology. Inequality W6 (CHN)> W6 (GX) which is given by the weight value of B3, means the number of skilled workers is small in the industry. Approximately W7 (CHN) equals W7 (GX), which is given by the weight value of B4, means the level of technical staff is close to the national level. Inequality W8 (CHN)> W8 (GX) which is given by the weight value of B5, means equipments in the industry are out of date.

(3) C. marketing of technological innovation

Inequality W9 (CHN)>>W9 (GX), which is given by the weight value of C1, means the level of on-line marketing about GungXi's non-ferrous metals enterprises is the lowest in china. Inequality W10 (CHN)>W10 (GX), which is given by the weight value of C2, means marketing system of nonferrous metals industry in Guangxi is not perfect, there is a gap between production and marketing. Inequality W11 (CHN)>W11 (GX), which is given by the weight value of C3, means nonferrous metals industry in Guangxi has a market share of new product.

4.3 The suggestions

This paper proposes some suggestions base on above analysis.

(1) Increase input of research and development

Enough capital could provide a good environment for people to engage in scientific and technological innovation. Furthermore, increase input of research and development has great significance for sustainable development of non-ferrous metals industry in Guangxi.

(2) Improve the construction of technical innovation group

High quality researchers are an important part of technical innovation group and senior technicians are also a necessary part. Enterprise should strengthen the cooperation among Industries, Universities and Research in finance, credit, tax and so on. Enterprise also should make full use of national funding, establish special fund of Research and fully raise the motivation of university, enterprise and society.

(3) Invest the construction of information system of enterprise

Constructing information system is systematic engineering. In one hand, enterprise should find ways to raise capital. In the other hand, enterprise should combine technical innovation project and information construction.

(4) Strengthen data resources management

Building information resource data base of enterprise and using the function of Data mining could help the enterprise find its marketing position.

5. Conclusions

This paper, based on RBF neural network theory, made a quantitative analysis and comprehensive evaluation of technological innovation ability about non-ferrous metals industry in Guangxi with software Mat lab 7.0. Comparing with the weight of each index of national non-ferrous metals industry, we concluded that the technological innovation ability in Guangxi is at middle level of national non-ferrous metals industry. But there is some inferiority such as input of technological innovation, output of technological innovation and marketing of technological innovation. In order to improve the technological innovation ability about non-ferrous metals industry in Guangxi effectively, it is necessary to increase input and improve the ability of changing knowledge into products, but necessary to strengthen the information management of enterprise.

References

Bin Zhu. (2009). Research on the Fuzzy Comprehensive Evaluation Methods and its application in the differences of regional innovation capabilities of Fujian province Based on a BP Network. *techno-economic and management study,* 3, 38-40.

Hong Ren, Yuwei Liu and Lianjing Li. (2009). The Status quo, Problems and Countermeasures for the Scientific Development of Non ferrous Metal Industry in Guangxi. *Enterprise Science And Technology & Development*, 262, 13-14.

Jiaji Fu. (1998). *Technological Innovation.* Beijing: Tsinghua Press, (Chapter 1).

Table 1. The evaluation indexes of technological innovation ability about NFMI

the evaluation indexes of technological innovation ability		
A. input of technological innovation	B. output of technological innovation	C. marketing of technological innovation
A1. research and development funds A2. the proportion of enterprises in the industry A3. the proportion of research and development personnel	B1. output of new product B2. patent owned /number of patent applications B3. number of skilled workers / number of employed persons B4. the level of technical staff B5. the level of equipment	C1. the level of on-line marketing C2. adaptability of marketing system C3. market share of new product

Table 2. Standardized data

year	A1	A2	A3	B1	B2	B3	B4	B5	C1	C2	C3
1998	0.471	1.000	0.673	0.995	0.526	0.927	0.113	1.0	1.0	1.0	0.6
1999	0.800	0.792	1.000	0.984	0.161	0.907	0.135	0.5	1.0	1.0	0.85
2000	0.314	0.773	0.565	1.000	0.516	0.875	0.164	0.5	1.0	1.0	0.80
2001	1.000	1.000	0.510	0.969	0.000	0.796	0.192	0.5	1.0	1.0	0.80
2002	0.071	0.773	0.184	0.938	0.419	0.738	0.201	0.5	1.0	1.0	0.85
2003	0.128	0.792	0.000	0.909	0.494	0.660	0.161	0.5	0.5	0.5	0.9
2004	0.000	0.773	0.347	0.532	0.430	0.523	0.140	0.0	0.0	0.5	0.85
2005	0.400	0.792	0.021	0.659	0.526	0.126	0.048	0.0	0.0	0.0	0.6
2006	0.485	0.735	0.021	0.000	0.602	0.000	0.000	0.0	0.0	0.0	0.0
GX	0.928	0.000	0.347	0.932	1.000	1.000	1.000	1.0	0.0	0.5	1.0
target values	2.45,2.59,3.23,2.91,4.05,5,6.41,7.23,8.36						AVG=4.69				

Table 3. Weight values

|	W1	W2	W3	W4	W5	W6	W7	W8	W9	W10	W11
CHN	0.861	0.792	1.0	0.984	0.161	0.907	0.135	0.5	1.0	1.0	0.85
GX	0.373	0.700	0.2	0.715	0.041	0.531	0.129	0.28	0.5	0.6	0.68
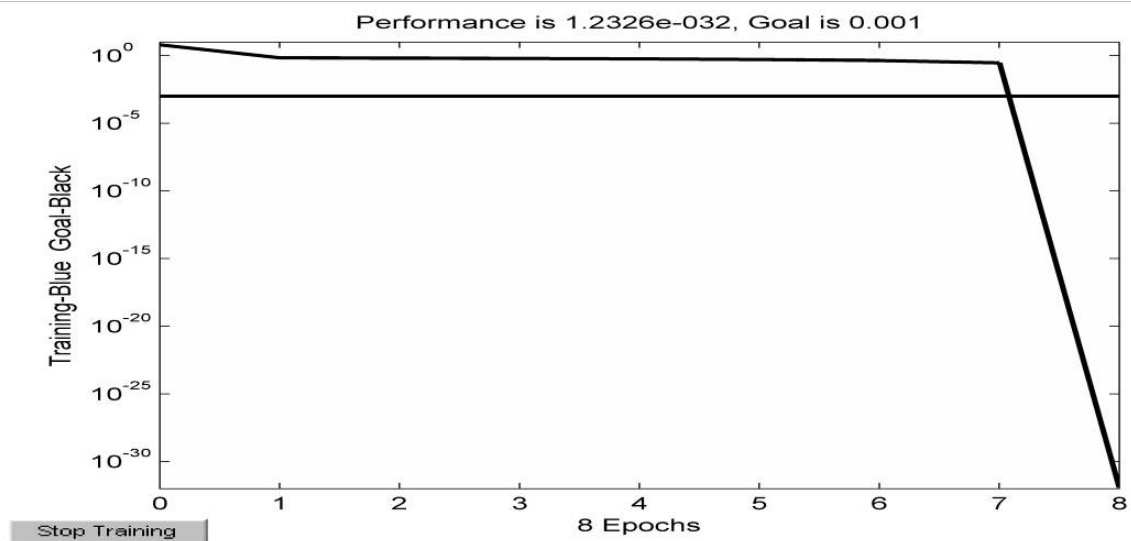
Figure 1. The error of training

Sine Carrier for Fundamental Fortification in Three Phase Z-Source PWM Inverters

U.Shajith Ali (Corresponding author)

Department of EEE, SSN College of Engineering

Kalavakkam, Chennai, India

Tel: 91–44 –2727–5064   E-mail: shajithali@ssn.edu.in

V.Kamaraj

Department of EEE, SSN College of Engineering

Kalavakkam, Chennai, India

Tel: 91–44 –2727–5064   E-mail: kamarajv@ssn.edu.in

Abstract

This paper deals with a novel natural sampled pulse width modulation strategy for three phase Z-source inverter through carrier modification. The proposed sine carrier method, which uses the conventional sinusoidal reference signal and a sine carrier, has a better harmonic spectrum and a higher fundamental component compared to the conventional triangular carrier based PWM. The sine carrier PWM enhances the fundamental output voltage while keeping the total harmonic distortion lower without involving changes in device switching loss. The detailed comparison of harmonic content and fundamental component of the sine carrier PWM output with the results obtained for the conventional PWM is also presented. Microcontroller is chosen for the hardware implementation of the switching strategy, mainly due to its high computation speed which can ensure the accuracy of the instants that gating signals are generated.

Keywords: Pulse width modulation, Sine carrier, Triangular carrier, Total harmonic distortion, Z-source inverter

1. Introduction

In a traditional voltage-source inverter, the two switches of the same phase leg can never be gated on at the same time because doing so would cause a short circuit(shoot through) to occur, which would destroy the inverter. In addition, the maximum output voltage obtainable can never exceed the dc bus voltage. An LC filter is also needed for providing a sinusoidal voltage, which causes additional power loss and complexity. These limitations can be overcome by the new Z-source inverter, shown in Figure.1.which uses an impedance network (Z network) to replace the traditional dc link. (F.Z. Peng, 2003)

The Z-source inverter advantageously utilizes the shoot through states to boost the dc-bus voltage by gating on both the upper and lower switches of a phase leg. Therefore, the Z-source inverter can buck and boost voltage to a desired output voltage that is greater than the available dc bus voltage. In addition, the reliability of the inverter is highly improved because shoot-through can no longer destroy the circuit. Thus it provides a low cost, reliable, and highly efficient single stage structure for buck and boost power conversion.

In the traditional PWM technique of the voltage source inverter, there are eight permissible switching states: six active and two zero states. During the two zero states, the upper three or the lower three switches are turned on simultaneously, thus shorting the output terminals of the inverter and producing zero voltage to the load. During one of the six active states, the dc voltage is impressed across the load, positively or negatively. In addition to the eight traditional switching states, the Z-source inverter has several shoot-through zero states, during which both the upper and lower switches of one or multiple same phase legs are turned on. It is obvious that during a shoot-through zero state, the output terminals of the inverter are shorted and the output voltage to the load is zero. Therefore, the shoot through states has the same effect (i.e., zero voltage) to the load as the traditional zero states; however, these shoot through states can boost the dc

voltage. The active states have to be kept unchanged to maintain the output voltage waveform, and the traditional zero states can be replaced partially or entirely by the shoot through zero states depending on how much voltage boost is needed.

All the traditional pulse width modulation (PWM) schemes can be used to control the Z-source inverter and their theoretical input-output relationships still hold. Several modified PWM control method for the Z-source inverter based on traditional control methods were presented in the literature. (Miaosen Shen , 2004;P.C.Loh et al, 2005). In the simple boost control method two straight lines are used to control the shoot through states. (F.Z.Peng, 2003; F.Z.Peng et al, 2005).This method has drawbacks of high voltage stress across devices. But the maximum boost control technique can achieve minimum voltage stress across devices and maximum boosted output voltage. However, it has the drawback of low frequency ripple associated with output frequency.

2. Proposed sine carrier PWM

The Z-source inverter intentionally utilizes the shoot-through zero states to boost dc voltage and produce and output voltage greater than the original dc voltage. But the shoot-through zero states does not affect the PWM control of the inverter, because it equivalently produce the same zero voltage to the load terminal. The available shoot-through period is limited by the zero-state period that is determined by the modulation index.

The voltage gain of the Z-source inverter can be expressed as (N.Mohan et al, 1995)

$$\frac{v_o}{V_{dc}/2} = M_a B \tag{1}$$

where v_o is the output peak phase voltage, V_{dc} is the input dc voltage, M_a is the modulation index, and B is the boost factor.

B is determined by

$$B = \frac{1}{1 - 2D_o} \tag{2}$$

where D_o is the shoot through duty ratio.

In the conventional simple boost control method, a triangular carrier was used to control the shoot-through duty ratio. In this case, the shoot-through time per switching cycle is constant, which means the boost factor is constant. In this conventional triangular carrier PWM the shoot through duty ratio is given as

$$D_o = 1 - M_a \tag{3}$$

In this conventional simple boost control method, to achieve the high output voltage, it is required to increase the shoot through duty ratio, which can only be achieved with the reduction of modulation index. But small modulation index results in greater voltage stress on the device, hence it restricts the obtainable gain because of the limitation of device voltage rating.

The proposed control strategy uses the conventional sinusoidal reference while the carrier wave is a modified one. The control scheme uses a high frequency sine carrier that helps to maximize the output voltage for a given modulation index.

For the proposed PWM, the shoot through duty ratio is determined by

$$D_o = \frac{(\pi - 2\sin^{-1} M_a)}{2\pi} \tag{4}$$

The boost factor B and the voltage gain can be calculated:

$$B = \frac{\pi}{\sin^{-1} M_a} \tag{5}$$

$$\frac{v_o}{V_{dc}/2} = M_a B = \frac{\pi M_a}{\sin^{-1} M_a} \tag{6}$$

For the same modulation index, the sine carrier PWM gives higher shoot through duty ratio as compared to that of triangular carrier PWM. In the conventional simple boost control method, the triangular carrier waveform is replaced by a sine waveform to generate gating pulses shown in Figure.2. It is worth while to note that in both the PWM methods

the number of pulses generated will be the same and hence constant switching loss is guaranteed. (S.Jeevananthan et al, 2007)

Figure.3. gives the variation of shoot through duty ratio for different modulation index with constant carrier frequency. The sine carrier gives higher shoot through duty ratio without any pulse dropping at given modulation index while makes the dependency a little non linear.

3. Simulation results

To show the effectiveness of the proposed modulator, simulation was performed for different modulation index values. The simulation was conducted with the three phase Z-source inverter with the following parameters: Z-source network: $L_1 = L_2 = 3.09$ mH, $C_1 = C_2 = 54.4$ µF, switching frequency is 10 kHz. The purpose of the system is to compare the performance of the Z-source inverter under the conventional triangular carrier PWM and the proposed sine carrier PWM. Figure.4. shows the simulated output waveforms and Figure.5. gives the harmonic spectrum of the output line voltage when triangular carrier PWM is used. The similar simulation results when sinusoidal carrier PWM used are shown in Figure.6. and Figure.7. The modulation index used in both the simulations is $M_a = 0.88$. The shoot-through zero state is populated evenly among the three phase legs, achieving an equivalent switching frequency of 60kHz viewed from the Z-network. Therefore, the required dc inductor L is minimized. From the above analysis, we have the following theoretical calculations:

For triangular carrier PWM

    $B = 1.316$

     $v_o = 141.8$V (line to line rms)

For sinusoidal carrier PWM

    $B = 2.92$

     $v_o = 314.7$V (line to line rms)

For the same modulation index the sine carrier PWM gives high boost factor and hence high peak output voltage. Also it gives higher fundamental output voltage. To increase the fundamental amplitude in the triangular PWM technique the only way is increasing M_a beyond 1.0, which is called as an overmodulation. Overmodulation causes the output voltage to contain many lower order harmonics and also it makes the fundamental component – modulation index non-linear. From the simulation analysis the proposed PWM gives less magnitude of lower order harmonics and hence lower values of total harmonic distortion (THD) in the output voltage. The THD and lower order harmonics magnitude are tabulated in Table.1. for the two PWM methods with a modulation index of 0.88.

4. Hardware implementation

The laboratory model for Z-source inverter as shown in Figure.8.was constructed. The same parameters as the simulation were used. The microcontroller PIC 18F4550 was used for firing pulse generation. The pulses obtained from the microcontroller were amplified using the driver chip IR2125. The gating pulse waveforms and the output line voltage waveform are given in Figure.9 and Figure.10.

5. Conclusion

The paper presents a novel sine carrier PWM scheme for controlling the output of the three phase Z-source inverter with improved fundamental component value at the given modulation index. Also this new method gives lower THD in the output voltage compared to the conventional triangular carrier PWM. In addition, this new method does not require any mode change and causes exactly same number of switching per cycle. Analytical, simulation, and experimental results have been presented. The Z-source inverter can buck-boost voltage, minimizes component count, increase efficiency and reduce cost.

References

F.Z. Peng. (2003). Z-source Inverter. *IEEE Transactions on Industry Applications*, 39(2),pp.504-510.

F.Z.Peng and Miaosen Shen, Zhaomingian. (2005). Maximum Boost Control of the Z-source Inverter, *IEEE Transactions on Power Electronics*, Vol.20,No.4,pp.833-838.

Miaosen Shen,Jin Wang, Alan Joseph, Fang Z Peng. (2004). Maximum Constant Boost Control of the Z-source inverter.*IEEE IAS*,pp.142-147.

N.Mohan, W.P.Robbin and T.Undeland. (1995). *Power Electronics: Converters, Applications and Design*. (Chapter 8)

P.C.Loh, D.M.Vilathagamuva, Y.S.Lai,G.T.Chua and Y.W.Li. (2005). Pulse width modulation of Z-source inverter. *IEEE Transaction on Power Electronics*,Vol.20,pp.1346-1355.

S.Jeevananthan, R.Nandakumar, and P.Dananjayan. (2007). Inverted sine carrier for fundamental fortification in PWM inverters and FPGA implementations. *Serbian Journal of Electrical Engineering*,Vol.4,No.2,pp.171-187.

Table 1. Comparison of THD, fundamental and lower order harmonics

Method	THD (%)	Fundamental Voltage V1 (V)	Third Harmonic V3 (%V1)	Fifth Harmonic V5 (%V1)	Seventh Harmonic V7 (%V1)	Ninth Harmonic V9 (%V1)	Eleventh Harmonic V11 (%V1)
Triangular Carrier PWM	4.14	199.6	0.08	2.89	2.86	0.02	0.38
Sine Carrier PWMS	2.53	300.1	0.05	1.96	1.45	0.0	0.18
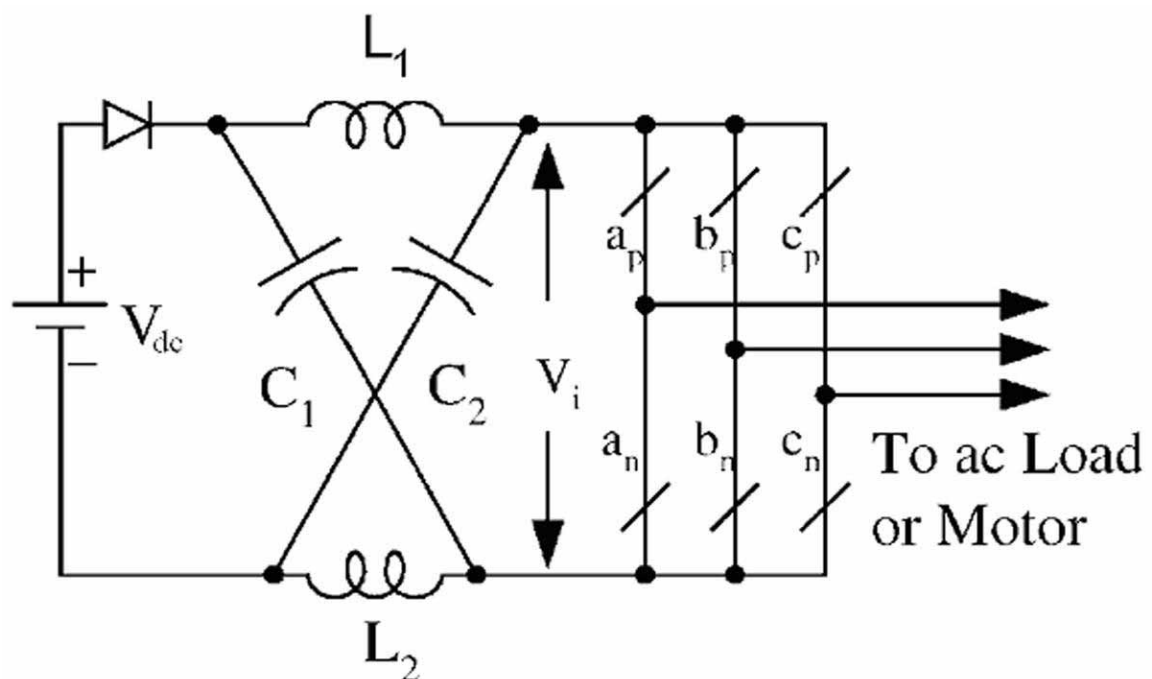
Figure 1. Z-source inverter
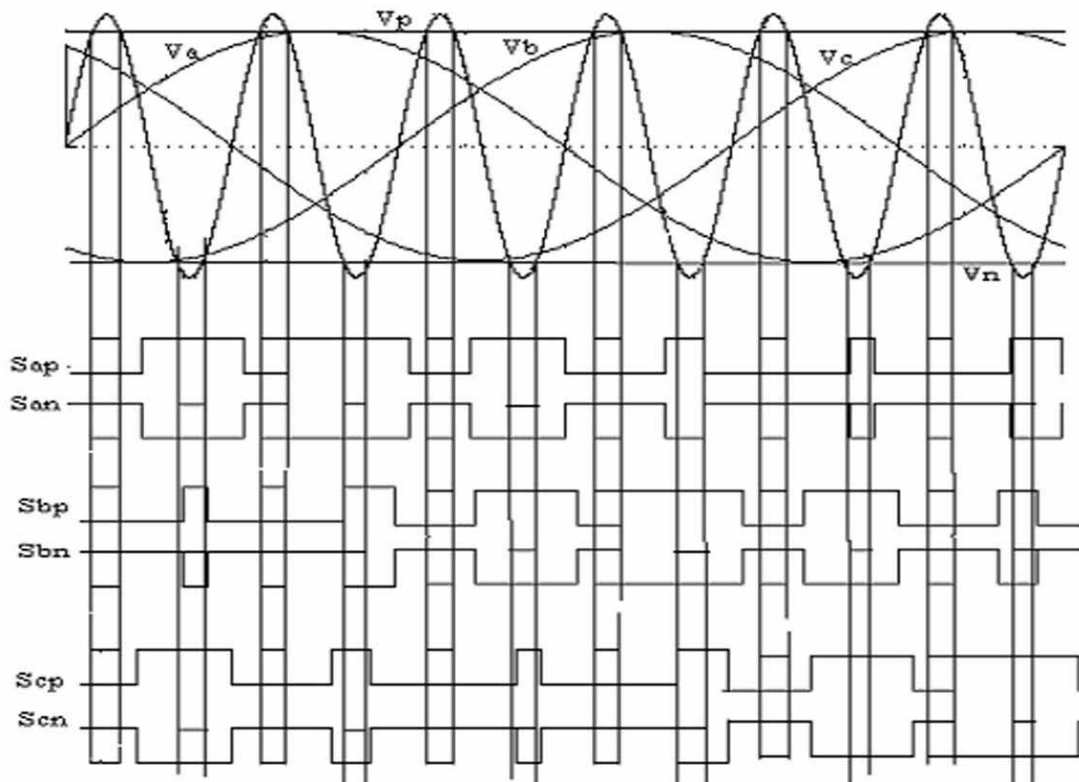
Figure 2. Proposed sine carrier PWM
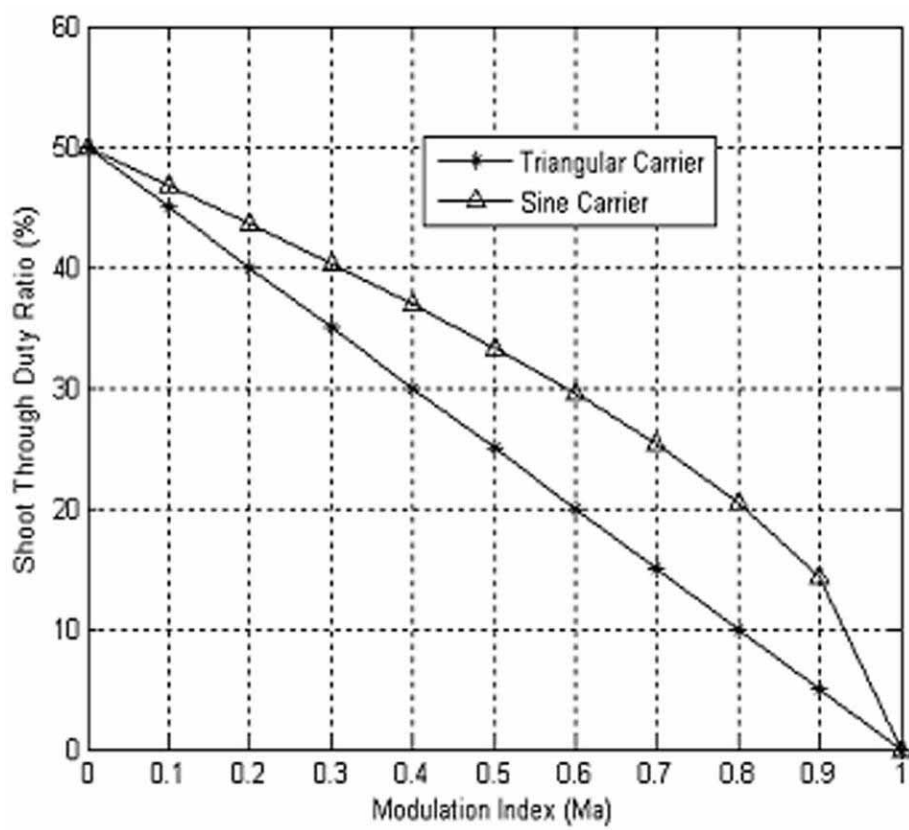
Figure 3. Modulation index vs shoot through duty ratio.
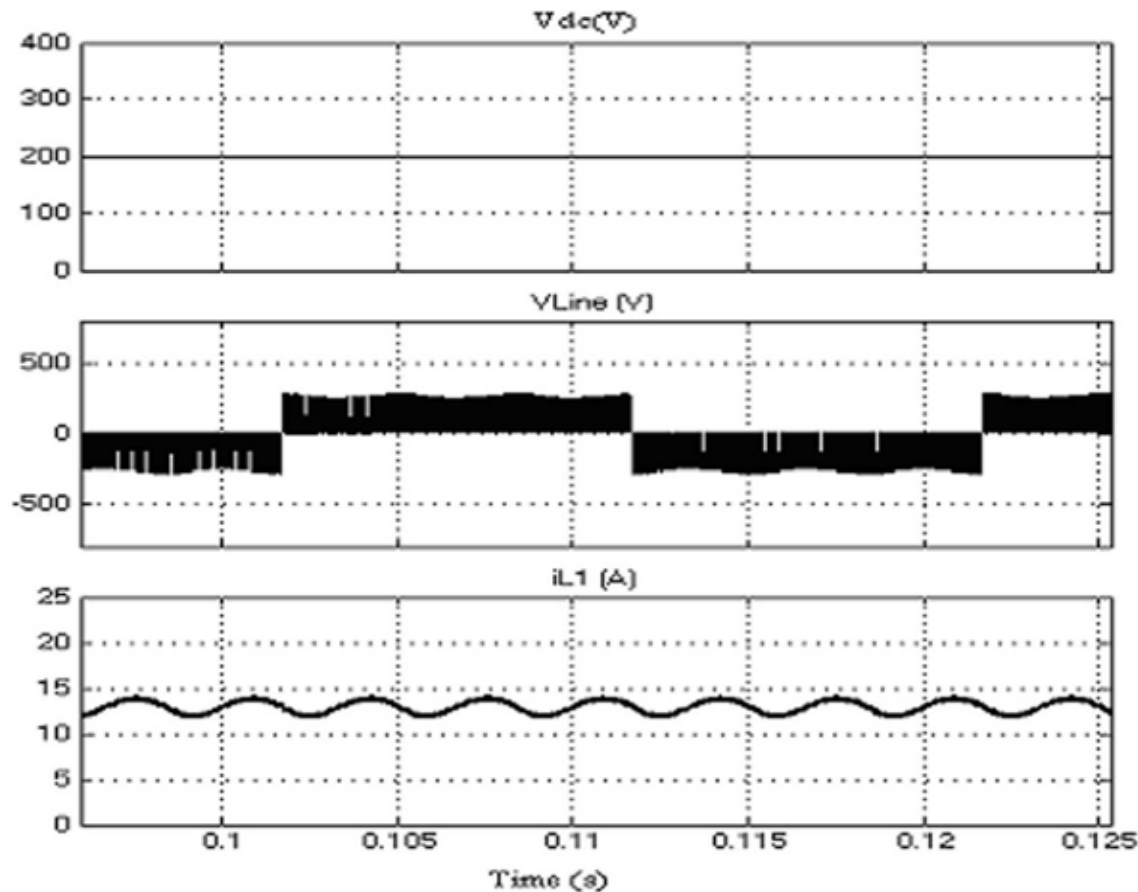
Figure 4. Simulation results with M_a = 0.88 using Triangular carrier PWM.
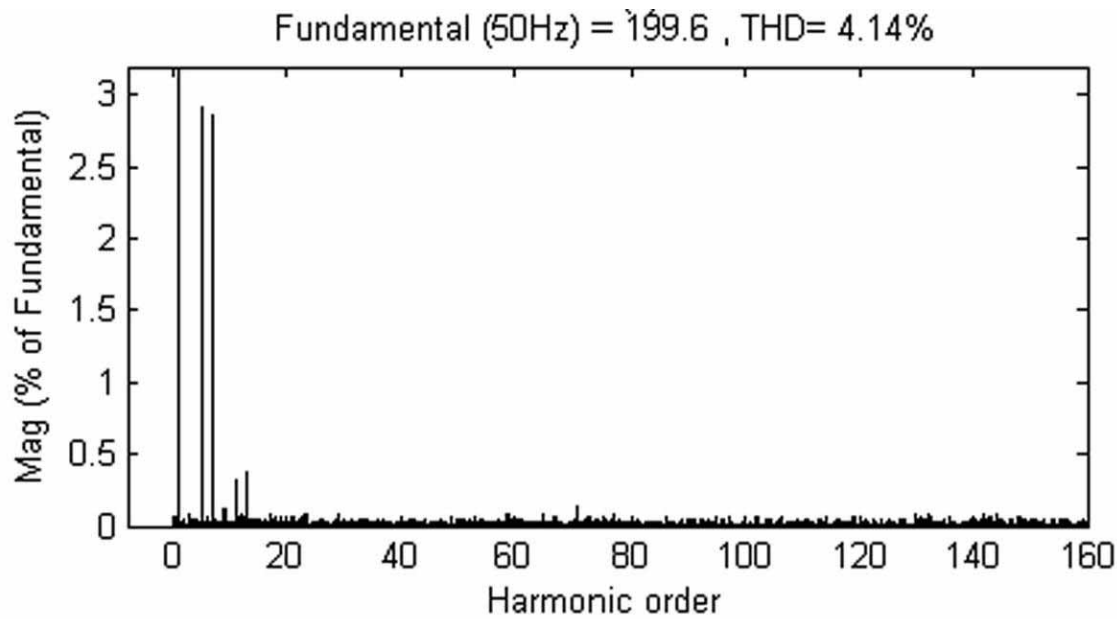
Figure 5. Simulated Harmonic Spectra of Z-source inverter with M_a = 0.88 using Triangular carrier PWM
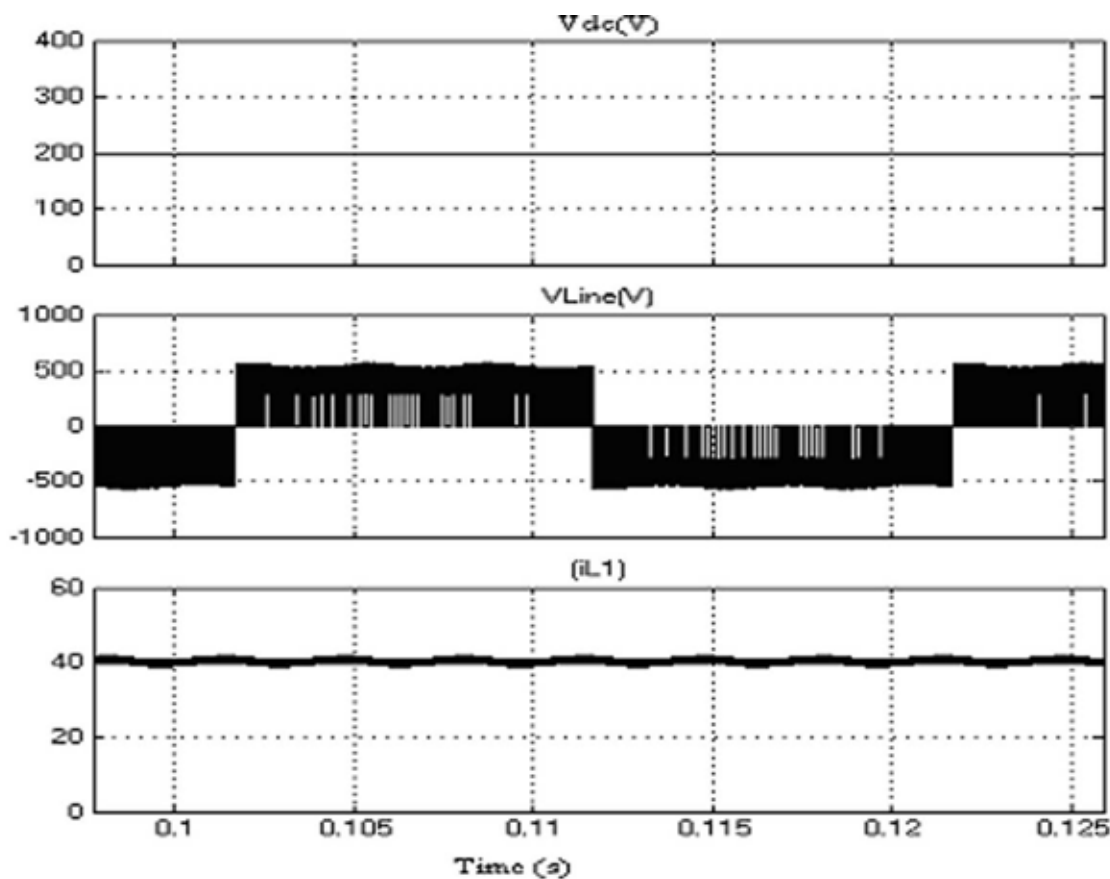
Figure 6. Simulation results with M_a = 0.88 using Sine carrier PWM
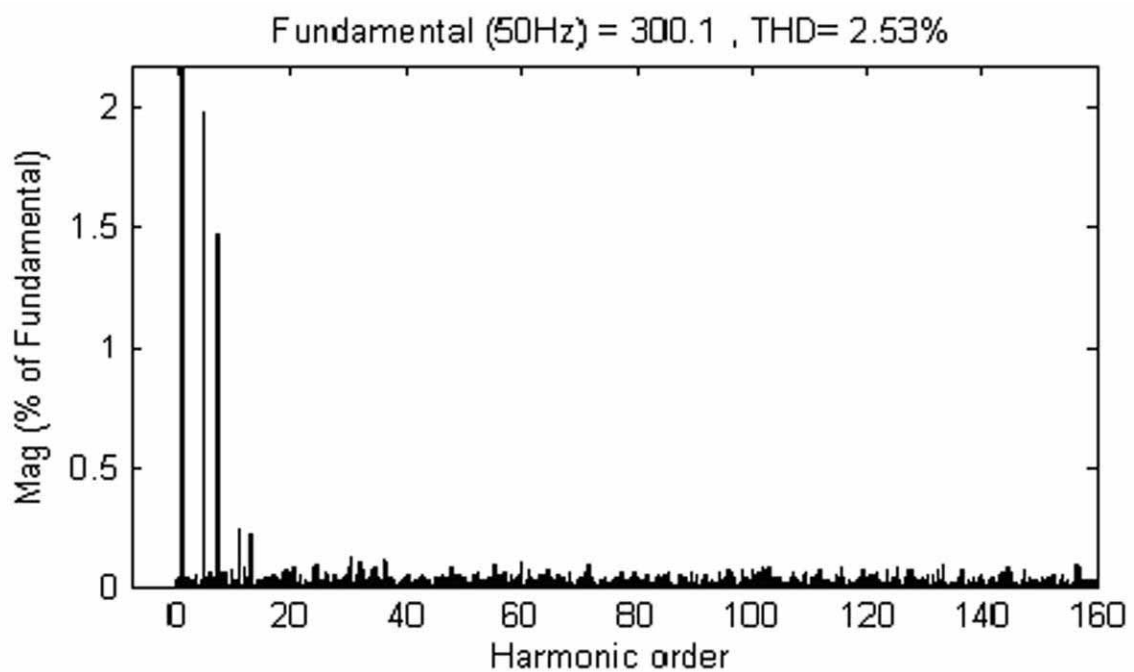

Figure 7. Simulated Harmonic Spectra of Z-source inverter with M_a = 0.88 using Sine carrier PWM
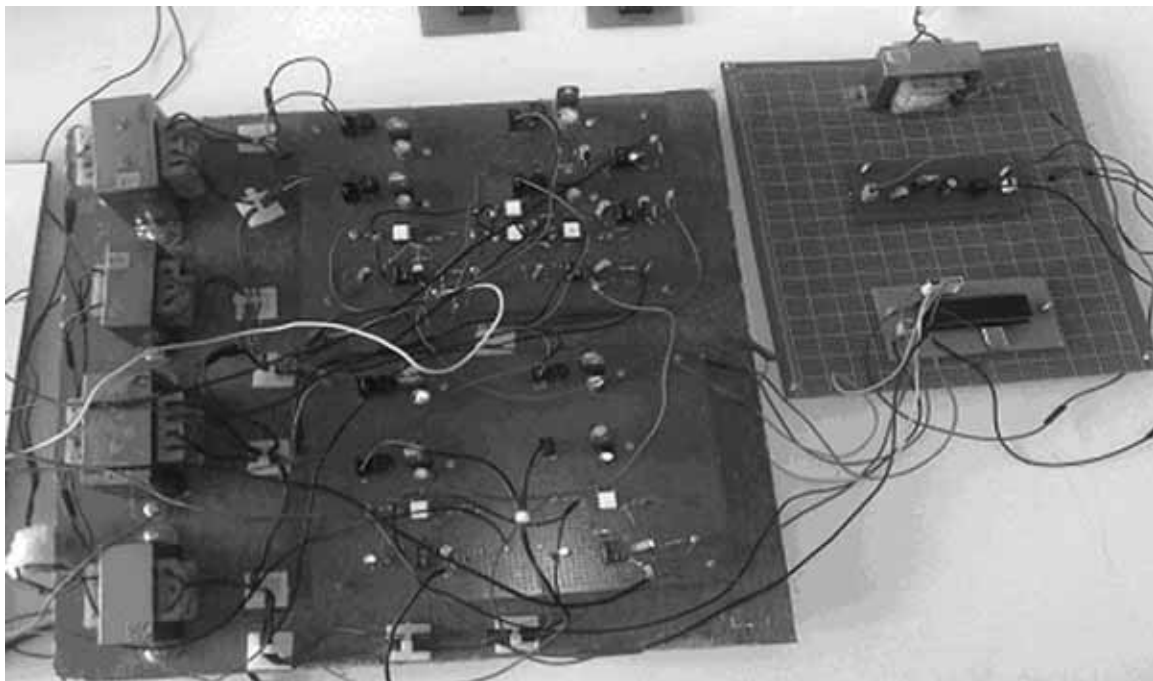
Figure 8. Hardware circuit
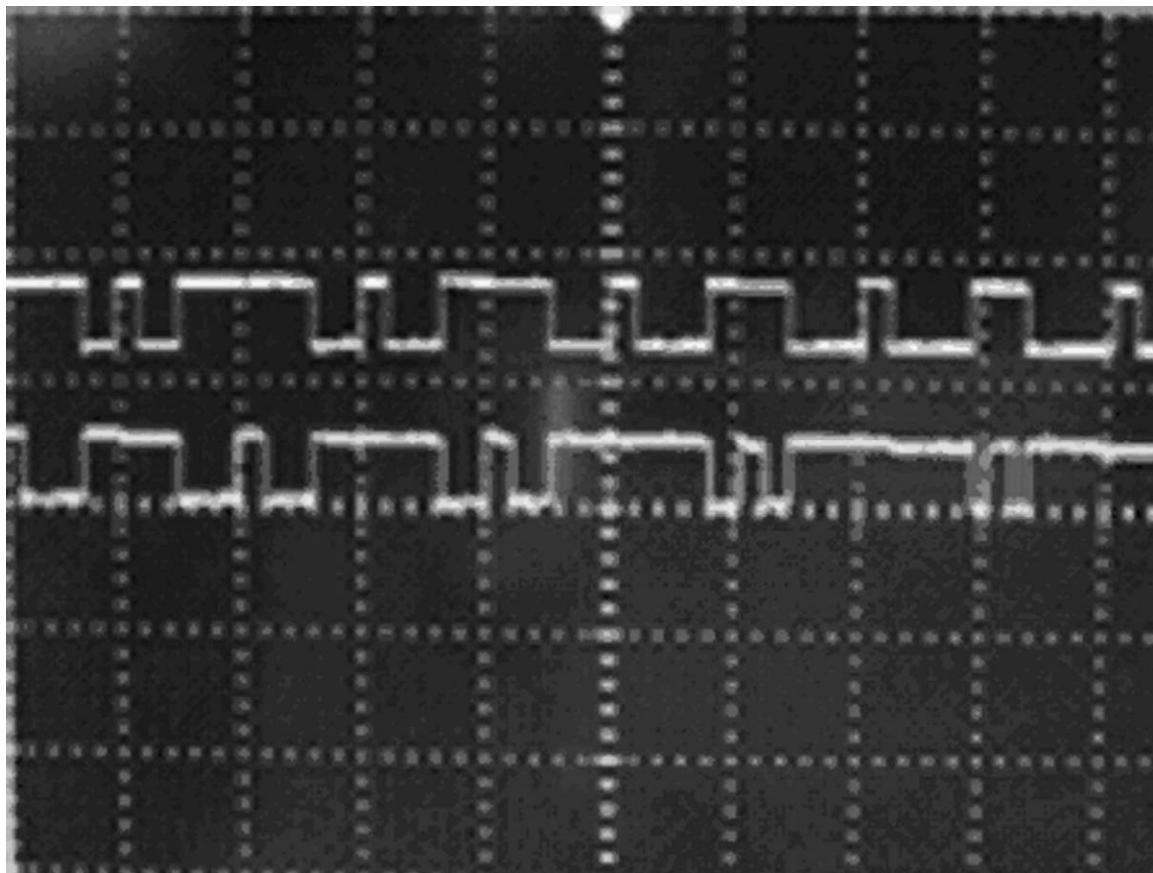
Figure 9. Firing pulses for switches S_{ap} and S_{an}
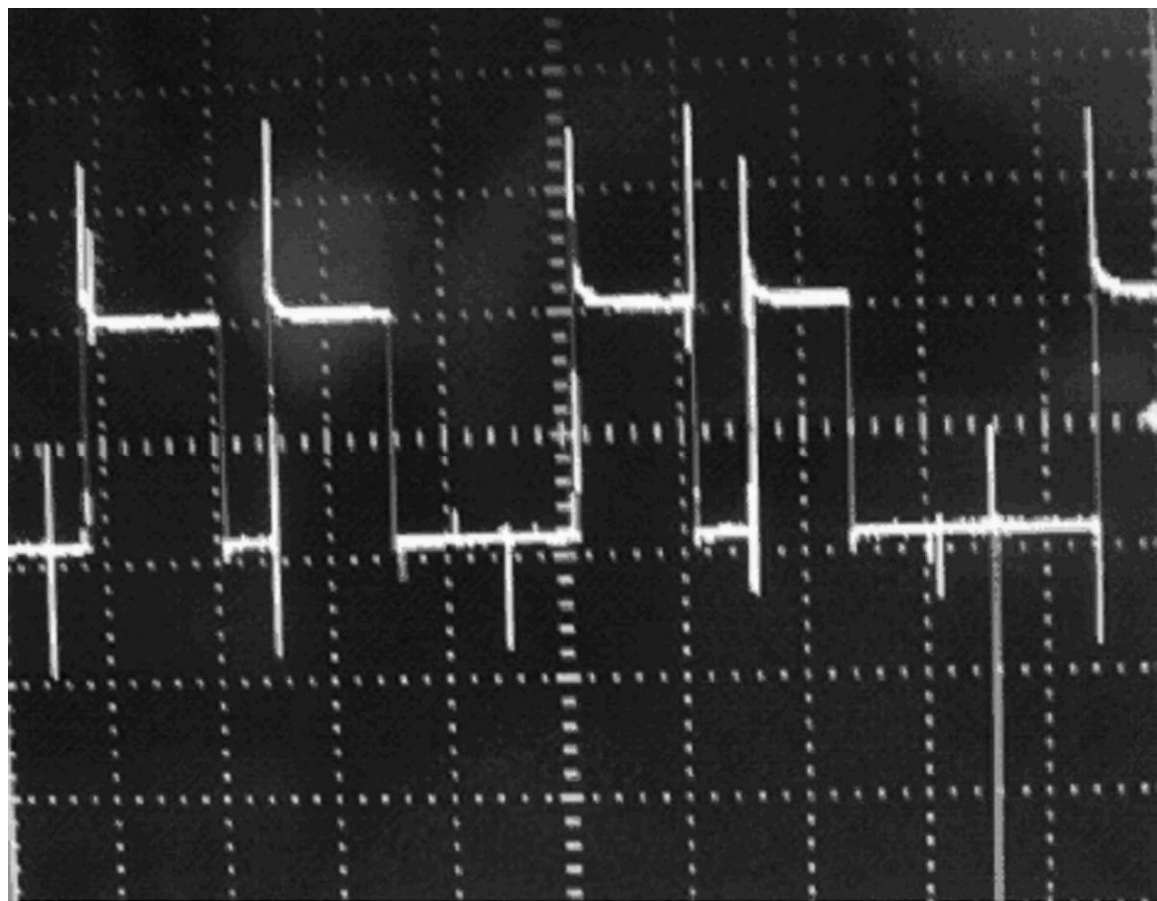
Figure 10. Output line voltage

Preparation of Hollow Fibre Composite Reverse Osmosis Membrane

Fengjuan Li

Key Lab of Hollow Fibre Membrane Materials & Membrane Processes

(Tianjin Polytechnic University) Ministry of Education

Tianjin 300160, China

E-mail: li_fengjuan@163.com

Wei Wang (Corresponding author)

Key Lab of Hollow Fibre Membrane Materials & Membrane Processes

(Tianjin Polytechnic University) Ministry of Education

Tianjin 300160, China

E-mail: wangwei7126@126.com

Qiang Ren

Oilfield Chemical Co .

CNOOC Energy Technology & Service Oilfield Technology Services Co.

Tianjin 300452, China

Abstract

A novel thin-film composite (TFC) reverse osmosis (RO) membrane was developed by the interfacial polymerization (IP) of trimesoyl chloride (TMC) and m-phenylene diamine (MPD) on the hollow fibre ultrafiltration polysulphone (PS) membrane. The performance of the TFC membrane was optimized by studying the preparation parameters, which included monomer TMC concentration, monomer MPD concentration and alcohol additive in aqueous solution. The reverse osmosis performance of the resulting membrane was evaluated through permeation experiment with 1000 ppm NaCl at 0.7 MPa. The results showed that the optimum concentration of MPD and TMC were 0.5wt% and 3g/L, respectively. To improve flux, alcohol was added to the aqueous phase, when certain concentration of alcohol was added to the aqueous solution, the flux of the prepared membrane increased from 5.0 to 9.1 L/(m^2·h) without loss in salt rejection. The properties and structures of skin layer of RO composite membranes were characterized by AFM. It was found that IP had occurred and the separation layer was formed, and the novel reverse osmosis membrane appears to comprise a thicker, smoother and less cross-linking film structure. Additionally, the TFC membrane exhibits good long-term stability.

Keywords: Reverse osmosis, Trimesoyl chloride, M-phenylene diamine, Hollow fibre, Acohol additive

1. Introduction

The concept of reverse osmosis (RO) treatment was started through the development of the asymmetric cellulose acetate membrane by Loeb and Sourirajan in the 1960s. The second breakthrough in this field was achieved by the development of thin-film-composite (TFC) membrane with high flux by the interfacial polymerization. In recent years, reverse osmosis desalination has been explored as a viable technology for desalination of brackish water for industrial and civil use (Kosutic, Dolar et al. 2007; Hrayshat 2008; Radjenovic, Petrovic et al. 2008). Reverse osmosis membranes are extensively used worldwide or the desalination, softening and purification of brackish, sea and other surface waters for potable, industrial and agricultural use. For the development of RO membranes, two different techniques have been used: the phase inversion method for asymmetric membranes, and the interfacial polymerization for thin-film-composite (TFC) membranes (Matsuura 2001). TFC membrane preparation technique is based on interfacial polymerization

(polycondensation) reaction between two monomers dissolved in water and hydrocarbon solvent, respectively (Roh, Kim et al. 2002; Freger 2003; Li, Zhang et al. 2007). Various benzenediamines and poly(aminostyrene) were interfacially reacted with various acryl chlorides to produce the thin skin layer. The obtained membrane showed typical trade-off behavior between the salt rejection and water permeability. Membrane prepared from trimesoyl chloride (TMC) and m-phenylene diamine (MPD) showed higher performance than usual membranes. Since water and the hydrocarbon solvent are immiscible, polymerization reaction takes place at the water/hydrocarbon interface. More specifically, the polymerization takes place at the organic phase side of the interface and not the aqueous phase side because of the highly non-favorable partition coefficient for the acid chloride which limits the availability of the acid chloride in the aqueous phase (Freger 2005). The thin film active layer ranging from 10 nm in thickness to several micrometers is quickly formed at the interface and strongly attached to the substrate (Freger and Srebnik 2003; Song, Sun et al. 2005).

A new concept for the preparation of thin-film-composite (TFC) reverse osmosis (RO)membrane by inter facial polymerization on porous polysulfone (PS) support using novel additives is reported. In order to improve the RO membrane performance, such as salt rejection and water flux, acohol was added to the aqueous phase. In this paper, the concentration of organic and aqueous phases was optimized since this parameter governs the amine monomer solubility and diffusivity in the reaction zone, which in fact affect the performance and morphology of the RO membrane (Ghosh, Jeong et al. 2008). We attempt to correlate MPD-TMC reaction to RO membrane separation performance (water flux, salt rejection) and interfacial characteristics (hydrophilicity, roughness). We also evaluate the addition of acohol to the aqueous MPD solution. These experiments allow us to satisfy our primary objective, that is, to elucidate the various interrelationships among reaction conditions and membrane properties. The properties and structures of skin layer of RO composite membranes were characterized by AFM. Finally, the impacts of operating pressure and the salt concentration on the properties of the RO membranes was discussed.

2. Experimental

2.1 Chemicals and regents

All chemicals used in this work are listed in Table 1. The chemicals, trimesoyl chloride (TMC), m-phenylenediamine (MPD), were used without further purification. Commercial UF polysulfone (PS) membranes of molecular weight cut-off (MWCO) 20,000 kD used as the support membrane were obtained from Tianjin Motimo membrane technology LTD. Monomer MPD (purity >99.5%) was purchased from Tianjin Guanfu Fine Chemical Research Institute, China, and key functional monomer TMC (purity >99.0%) was obtained from Beijin Odyssey chemical Co. Ltd. China. Sodium chloride were provided by Tianjin Kermel Chemical Reagent Co. Ltd. China. All the other regents were of analytical grade unless specified.

2.2 Membrane preparation

A layer of an aqueous solution was formed on a microporous polysulphone supporting film by making contact for 5~10 min of the solution with the supporting film and removing extra solution. The aqueous solution contained 0.5wt% MPD. Then, a composite membrane was obtained by making contact with an organic solution containing 0.5wt% TMC for 30s with the surface area of supporting film that was previously coated with the aqueous solution, and drying the film in a ventilation hood until heptane evaporated so that a skin layer was formed on the supporting film. The composite RO membrane was washed in deionized water and kept in glycerine overnight.

2.3 Membrane performance testing

Performance of the composite RO membranes was measured for all membrane samples using 1000 ppm NaCl at 0.7 MPa, 25℃, respectively. The water flux was determined by direct measurement of the permeate flow. The water flux is given by

$$F=S/(V\times t) \tag{1}$$

where F (L/m^2·h) is the water flux, S (m^2) the effective area of membrane, V(m^3) is the volume of permeate solution, t (h) the time.

The salt rejection rate was measured by the salt concentration in the permeate obtained through measurements of electrical conductance of the permeate and the feed using a conductance meter (DDS-11A, Shanghai Leici Instruments, China). The salt rejection of the membrane is defined as the following ratio

$$R(\%)=(1- C_p/ C_0)\times 100 \tag{2}$$

where R is the salt rejection, C_p (mg/L) the permeate concentration and C_0 (mg/L) the feed concentration.

The water flux and salt rejection of membranes were measured by collection the permeate for 30 min after stabilization for 30min. All membrane samples were prepared and tested in at least duplicated with a total of three membranes tests for RO performance, results of which have been averaged. Schematic drawing of the membrane equipment is illustrated

in Figure.1.

2.4 Membrane surface morphology

The surface morphologies of composite membranes and substrate were observed with AFM. To prepare samples for AFM, the membranes were dried in vacuum at room temperature. The membranes were taken out of water and air-dried and they were ready for AFM observation.

3. Results and discussion

3.1 The effect of MPD concentration

In this research, reaction conditions, especially the concentration of monomers and relative reaction time, were optimized to obtain the most suitable one for the formation of the active top layer of the composite membrane. The effects of the concentration of MPD in aqueous on the performance of composite membrane was investigated at 25℃, 0.3MPa, with 1000 ppm NaCl aqueous solution as test solution. The results were shown in Figure.2. Figure.2. shows that the permeate flux declined and the rejection increased as the concentration of MPD in aqueous phase enhanced. But the declination of flux slowed down and the rejection became constant as the concentration of MPD over 0.5wt%.

3.2 The effect of TMC concentration

The relationship between the permeation properties of the membrane and the acyl chloride content was also investigated, and the result was illustrated in Figure. 3. Increasing the amount of acyl chloride in the polymerization solution results in a rapid increase in NaCl separation, correspondingly, the water flux decreases approximately exponentially as the amount of cross-linking agent is increased. The variation of composite membrane performance with the concentration of TMC in organic phase exhibited the same trend, but leveled off as the concentration of TMC exceeded 3g/L, as shown in Fig. 3.

3.3 The effect of acohol additive

Acohol could be employed as an additive to control the roughness of the active layer, and then adjust the properties of the resulting composite RO membrane. Table 1 illustrates the performance of the resulting composite RO membranes to 1000 ppm NaCl solution. The permeate flux increased by 40% and the rejection wasn't decreased while the acohol was added into aqueous solution.

3.4 Effect of operation pressure

The effect of NaC1 concentration on RO rejection and flux are also considered. Experiments were carried out to study the effect of operating pressure, ranging between 0.4 MPa and 0.7 MPa. The effect of operating pressure on RO rejection and flux are also considered was reported in Figure. 4. It shows that the flux of the RO membrane increase with an increase of operating pressure; the relationship between the flux and the operating pressure is nearly linear. It also shows that the rejection increases with increase in operating pressure for all the membranes, because ion transport due to convection becomes significant compared to diffusion. A high diffusive transport of salts through the membrane compared to convective transport may be the reason increase the rejection (Vaidya, Simaria et al. 2001).

3.5 Effect of feed concentration on membrane performance

The effect of NaC1 concentration on RO rejection and flux are also considered. The feed concentration effect experiment was performed with the RO membrane by changing the NaCl concentration in the feed aqueous solution and the results of salt rejection and water flux to NaCl aqueous solution of different concentrations is shown in Figure.5. It shows that, as the feed NaCl concentration increases from 0.003 to 0.017 mol/L, the salt rejection of the membrane decreases slightly, while the flux of the membrane declines sharply because of the increase of osmotic pressure. It is also worth mentioning that the salt rejection of the membrane still remains more than 90% even the feed NaCl concentration is up to 0.01 mol/L.

3.6 Membrane morphologies

AFM images of the surface morphologies of RO membranes with a projection area of 10μm×10μm prepared from MPD and MPD-acohol were shown in Figure.6., in which the brightest point presented the highest point of the membrane and the dark regions presented the valleys. As shown in Fig.6., the order of the membrane roughness was MPD-acohol > MPD, and there was an obvious correlation of the water permeability with the surface roughness and surface area of the TFC membranes. It is obvious that the flux of the membrane increased in proportion to the increasing surface roughness and the enlarging surface area. The reason for this phenomenon might be that the rougher and larger surface area of the membranes made it possible to have contact with more water molecules in the given projected area, which attributed the higher flux.

4. Conclusions

A new concept for the preparation of TFC RO membrane by interfacial polymerization on hollow fibre ultrafiltration PS

support is presented. The properties of the developed composite RO membranes could be adjusted by changing the concentration of the casting solution of the active layer, the concentration of the crosslinking agent, the addition of acohol, etc. The optimal polymerization conditions for the TFC RO membrane are as follows: MPD=0.5wt%; TMC=3g/L; added little acohol to aqueous solution. The permeate flux and the rejection increases while the flux increases as the operating pressure is increased in NaCl aqueous solution. However, when increased the concentration of NaCl aqueous solution, the salt rejection of the membrane decreases slightly, while the flux of the membrane declines sharply. Finally we found that added acohol to aqueous solution could improve the surface properties and of the TFC RO membrance, and increased the permeate flux considerably.

References

Freger, V. (2003). "Nanoscale heterogeneity of polyamide membranes formed by interfacial polymerization." Langmuir 19(11): 4791-4797.

Freger, V. (2005). "Kinetics of film formation by interfacial polycondensation." Langmuir 21(5): 1884-1894.

Freger, V. and S. Srebnik (2003). "Mathematical model of charge and density distributions in interfacial polymerization of thin films." Journal of Applied Polymer Science 88(5): 1162-1169.

Ghosh, A. K., B.-H. Jeong, et al. (2008). "Impacts of reaction and curing conditions on polyamide composite reverse osmosis membrane properties." Journal of Membrane Science 311(1-2): 34-45.

Hrayshat, E. S. (2008). "Brackish water desalination by a stand alone reverse osmosis desalination unit powered by photovoltaic solar energy." Renewable Energy 33(8): 1784-1790.

Kosutic, K., D. Dolar, et al. (2007). "Removal of antibiotics from a model wastewater by RO/NF membranes." Separation and Purification Technology 53(3): 244-249.

Li, L., S. Zhang, et al. (2007). "Polyamide thin film composite membranes prepared from 3,4',5-biphenyl triacyl chloride, 3,3',5,5'-biphenyl tetraacyl chloride and m-phenylenediamine." Journal of Membrane Science 289(1-2): 258-267.

Matsuura, T. (2001). "Progress in membrane science and technology for seawater desalination - a review." Desalination 134(1-3): 47-54.

Radjenovic, J., M. Petrovic, et al. (2008). "Rejection of pharmaceuticals in nanofiltration and reverse osmosis membrane drinking water treatment." Water Research 42(14): 3601-3610.

Roh, I. J., J. J. Kim, et al. (2002). "Mechanical properties and reverse osmosis performance of interfacially polymerized polyamide thin films." Journal of Membrane Science 197(1-2): 199-210.

Song, Y. J., P. Sun, et al. (2005). "Mechanisms of structure and performance controlled thin film composite membrane formation via interfacial polymerization process." Journal of Membrane Science 251(1-2): 67-79.

Vaidya, S. Y., A. V. Simaria, et al. (2001). "Reverse osmosis transport models evaluation: A new approach." Indian Journal of Chemical Technology 8(5): 335-343.

Table 1. The effect of acohol additive to the RO membrane salt rejection and water flux

	$F(L/m^2 \cdot h)$	$R(\%)$
MPD	5.0	93.9
Acohol additive	9.1	97.8
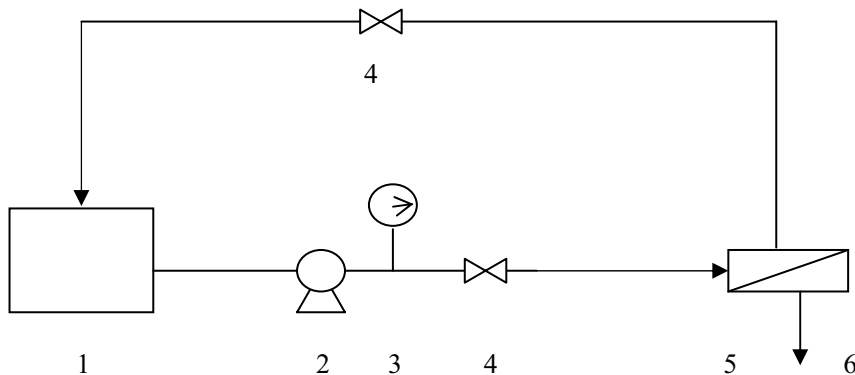
1 feed tank 2 diaphragm pump 3 pressure gauge 4 valve 5 RO membrane 6 permeate water

Figure 1. Schematic drawing of the membrane equipment
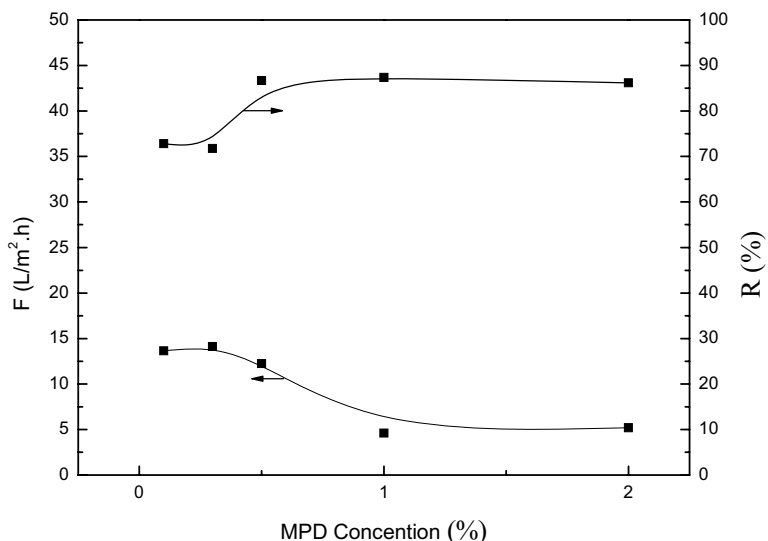


Figure 2. Effect of MPD concentration on salt rejection and water flux of the resulting membrane
testing at 0.7 MPa, 25℃, with 1000 ppm NaCl aqueous solution (TMC=3g/L)
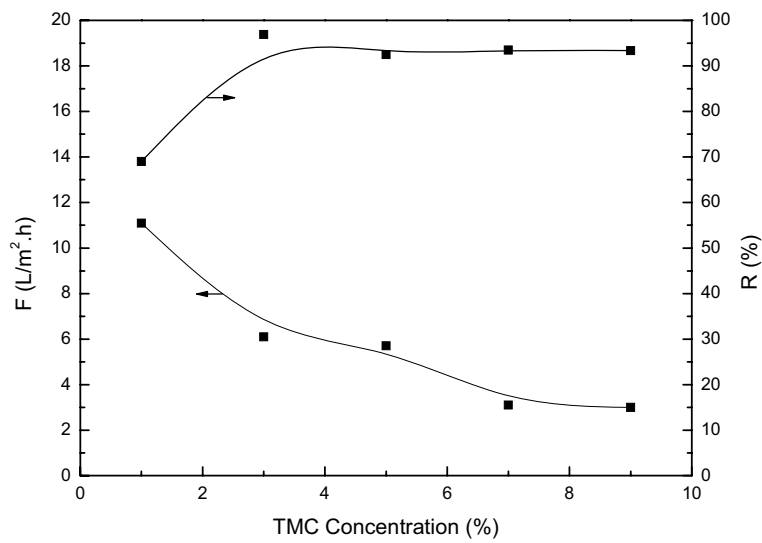
Figure 3. Effect on TMC concentration on salt rejection and water flux of the resulting membrane testing at 0.7MPa, 25℃, with 1000 ppm NaCl aqueous solution (MPD=0.5wt%)
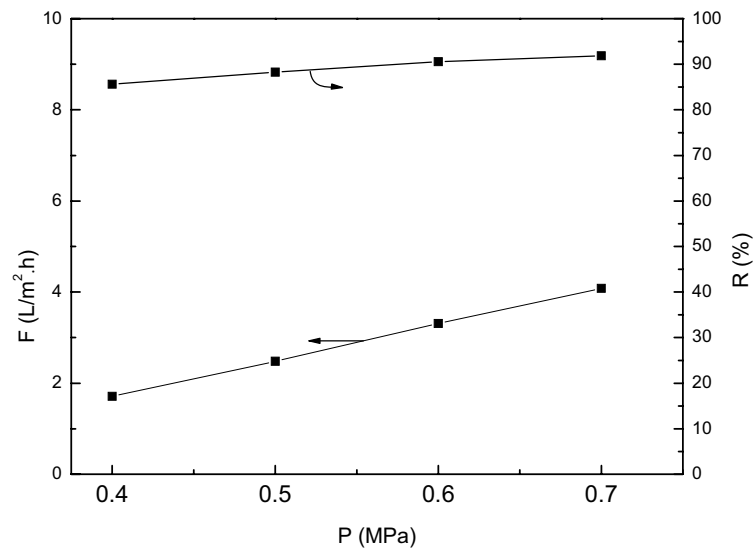

Figure 4. Effect of operation pressure on RO rejection and flux testing with NaCl aqueous solution at 0.7MPa, 25℃
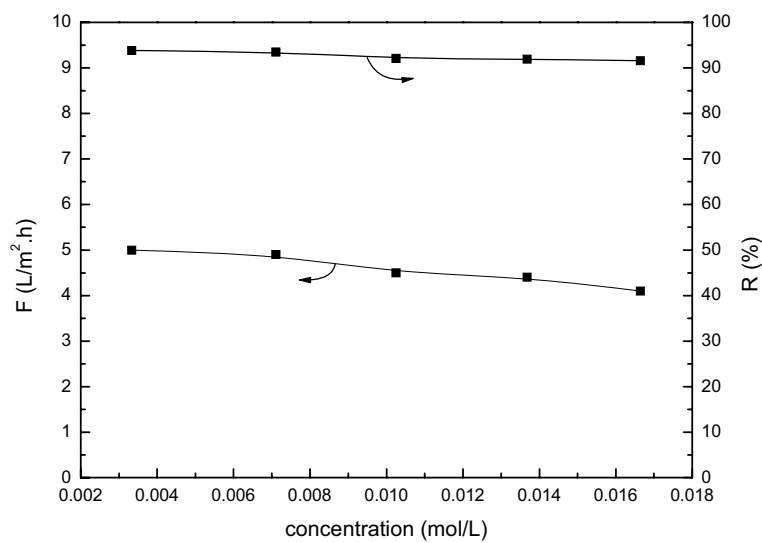
Figure 5. Effect of feed concentration on salt rejection and water flux testing with NaCl aqueous solution at 0.7MPa, 25℃
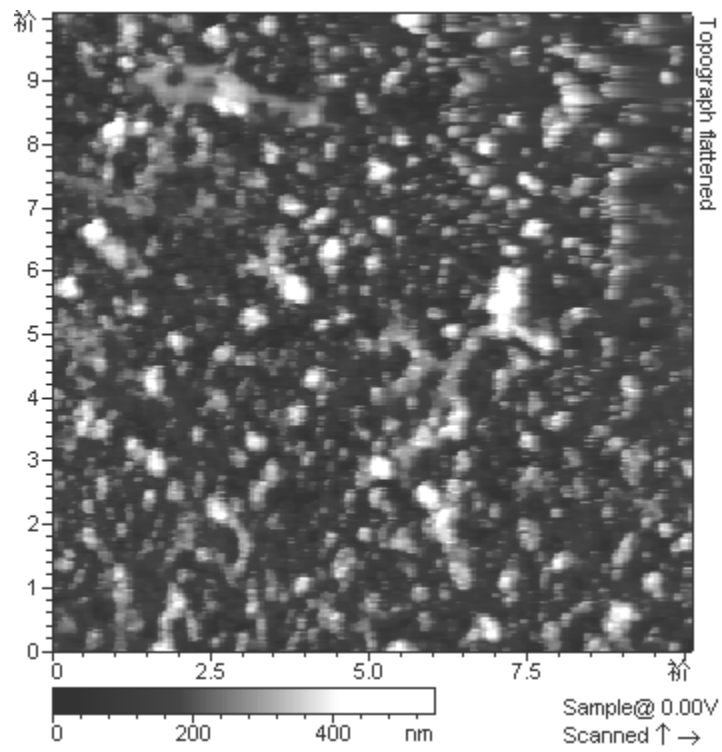

(a)
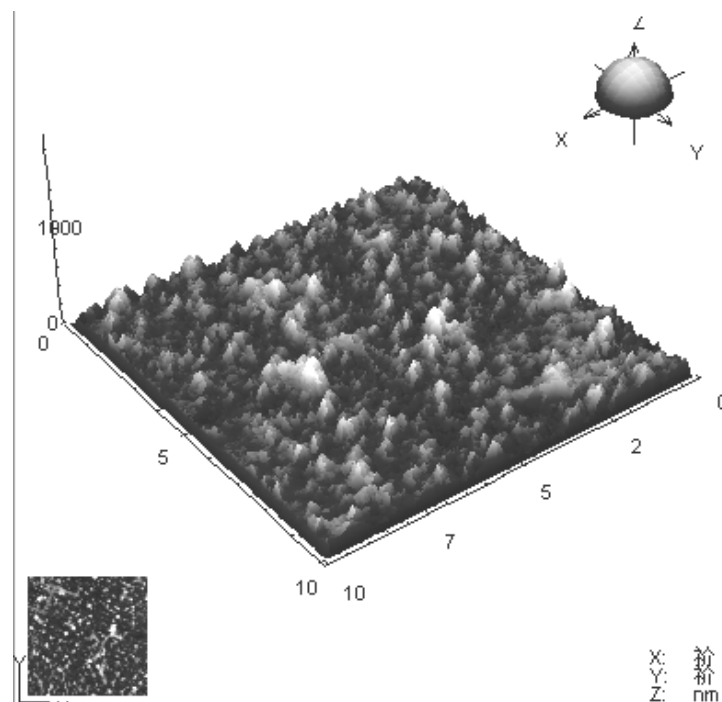
(b)
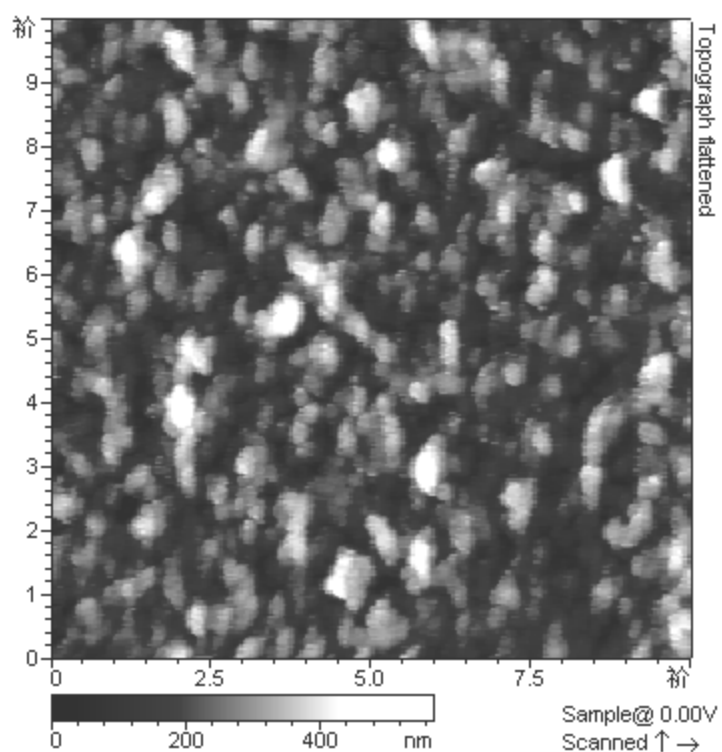
(c)
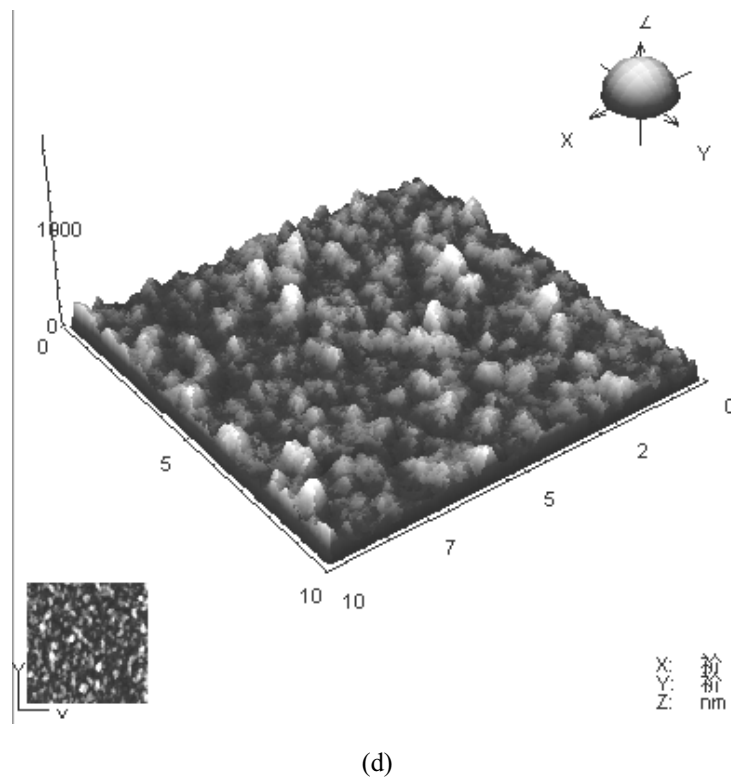
(d)

Figure 6. AFM images: (a) (b) the images of membranes prepared from MPD; (c) (d) the images of membranes prepared from MPD with acohol additive

Hopf Birurcation of Lorenz-like System about Parameter h

Gaoxiang Yang

Department of Mathematics, Ankang University

NO. 92 Yu Cai Road, Hanbin Region, Ankang City 725000, P. R. China

Email:gaoxiang7661@126.com

Abstract

The article mainly researched the Hopf bifurcation of Lorenz-like system about the coefficient of the quadratic term. When the quadratic term h changes, the solution to the Lorenz-like system will become the local periodic solution. Further the stability of this periodic solution and the bifurcation direction of this periodic solution were discussed, and found when the quadratic term h comes through a threshold h_0, the direction of hopf bifurcation and stability were given, and the result as follows. If $\alpha'(0) > 0$, when $\mu_2 > 0$, the direction of bifurcation is $h > h_0$, when $\mu_2 < 0$, the direction of bifurcation is $h < h_0$; (b) if $\alpha'(0) < 0$, we have the contrary result. That is when $\mu_2 > 0$, the direction of bifurcation is $h < h_0$; when $\mu_2 < 0$, the direction of bifurcation is $h > h_0$. If $\beta_2 < 0$, the bifurcation solution is asymptotically stable; if $\beta_2 > 0$, the bifurcation solution is not asymptotically stable. Finally employing the matlab compute the numerical periodic solution, the results fit the theory well.

Keywords: Lorenz-like system, stability, Hopf bifurcation

1. Introduction

Nonlinear science plays an important role in science research including biology, chemistry, fluid dynamics, optics and so on, but bifurcation theory is an important part in nonlinear science and many progresses have been made in the past many years. Bifurcation takes very significant role in the nonlinear system because bifurcation of the nonlinear system can lead to the chaotic behavior and induced the much more difficulty behaviors. So the research of bifurcation is the main means to understand nonlinear system well. The Lorenz-like system is very important like the Lorenz system which was found by the Lorenz in 1963 and many dynamical behaviors of this system have been discussed in the recent years. Such as the bifurcation behavior about the one order term, chaos and so on. This article mainly study the Hopf bifurcation (Lü JH, Zhou TS, Chen G..2002, Li TC, Chen G. 2004, Lü JH, Chen G. 2002, Changpin Li, Guanrong Chen. 2003)of the Lorenz-like system (Liu chongxin, Liu Ling,Liu tao, Li Peng, 2006), with precise numerical simulation. Firstly, this paper introduces some known results, and also introduces some relevant preparation including the elementary concepts. Secondly, this paper mainly employed the very important method of central manifold theory and theory of normal form to conduct a detailed discussion of Hopf bifurcation of the Lorenz-like system. Finally the precise numerical simulation was introduced to verify the theory analysis under the help of matlab. And the results of numerical simulation fit the theoretical analysis well.

2. Main results

Lorenz-like system is a 3-D automatics system, it satisfies the following equation,

$$
\begin{cases}
\dot{x} = a(y - x) \\
\dot{y} = bx - lxz \\
\dot{z} = -cz + hx^2 + ky^2
\end{cases}
\tag{1}
$$

Thereom 1 System (1) has three equilibriums if only if $ac(b^2 + l^2(h+k)^2) \neq 0$, and

$$bcl(h+k) > 0, S_0 = (0,0,0), S_+ = (\sqrt{\frac{bc}{l(h+k)}}, \sqrt{\frac{bc}{l(h+k)}}, \frac{b}{l}), S_- = (-\sqrt{\frac{bc}{l(h+k)}}, -\sqrt{\frac{bc}{l(h+k)}}, \frac{b}{l}).$$

Next, we consider the stability of equilibrium S_+ and S_-, under the condition $ac(b^2 + l^2(h+k)^2) \neq 0$ and $bcl(h+k) > 0$. As system (1) has the symmetry properties, S_+ and S_- have the same stability. For the equilibrium S_+, we can transform system (1) into the following form by $x = X + \sqrt{\frac{bc}{l(h+k)}}, y = Y + \sqrt{\frac{bc}{l(h+k)}}, z = Z + \frac{b}{l}$,

$$\begin{cases} \dot{X} = a(Y-X) \\ \dot{Y} = -l\sqrt{\frac{bc}{l(h+k)}}Z - lXZ \\ \dot{Z} = 2h\sqrt{\frac{bc}{l(h+k)}}X + 2k\sqrt{\frac{bc}{l(h+k)}}Y - cZ + hX^2 + kY^2 \end{cases} \tag{2}$$

So we consider the stability of system (2) at the equilibrium $(0,0,0)$. The linearization part of (2) is $A_+ = \begin{pmatrix} -a & a & 0 \\ 0 & 0 & -lx_0 \\ 2hx_0 & 2kx_0 & -c \end{pmatrix}$, where $x_0 = \sqrt{\frac{bc}{l(h+k)}}$. So the characteristic polynomial of A_+ is,

$$\lambda^3 + (a+c)\lambda^2 + (ac + 2kbc/(h+k))\lambda + 2abc = 0 \tag{3}$$

Thereom 2 If $ac(b^2 + l^2(h+k)^2) \neq 0$, $bcl(h+k) > 0$, $a+c > 0$, $abc > 0$

$2b - a - c \neq 0$, and $h_0 = \dfrac{k(a^2 + 2bc + ac)}{a(2b-a-c)}$, equation (3) has a pair of conjugate pure imaginary root $\pm i\sqrt{\dfrac{2abc}{a+c}}$ and a negative root $-(a+c)$.

Proof: if $h_0 = \dfrac{k(a^2 + 2bc + ac)}{a(2b-a-c)}$, $(a+c)(ac + 2kbc/(h+k)) = 2abc$, the characteristic equation (3) can be changed into $(\lambda^2 + \dfrac{2abc}{a+c})(\lambda + a + c) = 0$. So we can get roots of equation (3), $\lambda_{1,2} = \pm i\sqrt{\dfrac{2abc}{a+c}}$, $\lambda_3 = -(a+c)$.

By differentiating (3) with respect to h, it is found that

$$\lambda'(h) = -\frac{2kbc\lambda(h)}{(3\lambda^2 + 2(a+c)\lambda + ac + 2kbc/(h+k))(h+k)^2} \tag{4}$$

When $h = h_0 = \dfrac{k(a^2 + 2bc + ac)}{a(2b-a-c)}$, we can obtain $\text{Re}(\lambda'(h_0)) = -\dfrac{kbc(a+c)}{(h_0+k)^2((a+c)^2+d^2)}$,

$\omega'(0) = \text{Im}(\lambda'(h_0)) = \dfrac{kbcd}{(h_0+k)^2((a+c)^2+d^2)}$. Combing Theorem 2 and the definition of Hopf bifurcation(Li Jin-bing, Feng Bei-ye. 1995), we have the following result.

Thereom 3 The system(1)exist a hopf bifurcation at the equilibrium S_+ when the parameter h come though h_0. That h_0 is the value of the bifurcation.

Next we consider the direction of bifurcation and the stability of bifurcating solution. when $h = h_0$, the eigenvalue of $A_+(h_0)$ were $\lambda_1 = di$, $\lambda_2 = -di$, $\lambda_3 = -(a+c)$ and the corresponding eigenvectors were

$\alpha_1 + i\alpha_2$, $\lambda_3 = \alpha_3$ respectively, where $\alpha_1 = \begin{pmatrix} 1 & 1 & \dfrac{d^2}{alx_0} \end{pmatrix}^T$,

$$\alpha_2 = \begin{pmatrix} 0 & \dfrac{d}{a} & -\dfrac{d}{lx_0} \end{pmatrix}^T, \quad \alpha_3 = \begin{pmatrix} -\dfrac{alx_0}{c(a+c)} & \dfrac{lx_0}{a+c} & 1 \end{pmatrix}^T. \quad \text{Let} \quad P_0 = \begin{pmatrix} 1 & 0 & -\dfrac{alx_0}{c(a+c)} \\ 1 & -\dfrac{d}{a} & \dfrac{lx_0}{a+c} \\ \dfrac{d^2}{alx_0} & \dfrac{d}{lx_0} & 1 \end{pmatrix}, \quad m = -\det(P_0) = d\,\frac{(a+c)^2 + d^2}{ac(a+c)},$$

then $P_0^{-} = \dfrac{1}{m}\begin{pmatrix} \dfrac{d}{a}+\dfrac{d}{a+c} & \dfrac{ad}{c(a+c)} & \dfrac{dlx_0}{c(a+c)} \\ 1-\dfrac{d^2}{a(a+c)} & -1-\dfrac{d^2}{c(a+c)} & \dfrac{lx_0}{c} \\ -\dfrac{a^2d+d^3}{a^2lx_0} & \dfrac{d}{lx_0} & \dfrac{d}{a} \end{pmatrix}$. Using linear transformation $\begin{pmatrix} X \\ Y \\ Z \end{pmatrix} = P_0 \begin{pmatrix} u_1 \\ u_2 \\ u_3 \end{pmatrix}$, system(3)changed into the following

form:

$$\begin{pmatrix} \dot{u}_1 \\ \dot{u}_2 \\ \dot{u}_3 \end{pmatrix} = \begin{pmatrix} 0 & -d & 0 \\ d & 0 & 0 \\ 0 & 0 & -a-c \end{pmatrix} \begin{pmatrix} u_1 \\ u_2 \\ u_3 \end{pmatrix} + \begin{pmatrix} P \\ Q \\ R \end{pmatrix} \tag{5}$$

Where $P = \dfrac{1}{m}\left(\dfrac{ad}{c(a+c)}f_2 + \dfrac{dlx_0}{c(a+c)}f_3\right) = \dfrac{a^2}{((a+c)^2+d^2)}f_2 + \dfrac{alx_0}{((a+c)^2+d^2)}f_3$

$Q = \dfrac{1}{m}\left[-(1+\dfrac{d^2}{c(a+c)})f_2 + \dfrac{lx_0}{c}f_3\right]; \quad R = \dfrac{d}{mlx_0}f_2 + \dfrac{d}{ma}f_3; \quad f_2 = -l(u_1 - \dfrac{alx_0}{c(a+c)}u_3)(\dfrac{d^2}{alx_0}u_1 + \dfrac{d}{lx_0}u_2 + u_3)$

$$f_3 = h(u_1 - \dfrac{alx_0}{c(a+c)}u_3)^2 + k(u_1 - \dfrac{d}{a}u_2 + \dfrac{lx_0}{a+c}u_3)^2 \tag{6}$$

Compute the following terms(when $h = h_0$, $(u_1, u_2, u_3) = (0,0,0)$) $\tag{7}$

$$g_{11} = \dfrac{1}{4}\left[\dfrac{\partial^2 P}{\partial u_1^2} + \dfrac{\partial^2 P}{\partial u_2^2} + i(\dfrac{\partial^2 Q}{\partial u_1^2} + \dfrac{\partial^2 Q}{\partial u_2^2})\right] \tag{8}$$

$$g_{02} = \dfrac{1}{4}\left[\dfrac{\partial^2 P}{\partial u_1^2} - \dfrac{\partial^2 P}{\partial u_2^2} - 2\dfrac{\partial^2 Q}{\partial u_1 \partial u_2} + i(\dfrac{\partial^2 Q}{\partial u_1^2} - \dfrac{\partial^2 Q}{\partial u_2^2} + 2\dfrac{\partial^2 P}{\partial u_1 \partial u_2})\right] \tag{9}$$

$$g_{20} = \dfrac{1}{4}\left[\dfrac{\partial^2 P}{\partial u_1^2} - \dfrac{\partial^2 P}{\partial u_2^2} + 2\dfrac{\partial^2 Q}{\partial u_1 \partial u_2} + i(\dfrac{\partial^2 Q}{\partial u_1^2} - \dfrac{\partial^2 Q}{\partial u_2^2} - 2\dfrac{\partial^2 P}{\partial u_1 \partial u_2})\right] \tag{10}$$

$$G_{21} = \dfrac{1}{8}\left[\dfrac{\partial^3 P}{\partial u_1^3} + \dfrac{\partial^3 P}{\partial u_1 \partial^2 u_2} + \dfrac{\partial^3 Q}{\partial u_1^2 \partial u_2} + \dfrac{\partial^3 Q}{\partial u_2^3} + i(\dfrac{\partial^3 Q}{\partial u_1^3} + \dfrac{\partial^3 Q}{\partial u_1 \partial^2 u_2} - \dfrac{\partial^3 P}{\partial u_1^2 \partial u_2} - \dfrac{\partial^3 P}{\partial u_2^3})\right] \tag{11}$$

As $n = 3 > 2$, we need to computer the following terms,

$$h_{11} = \dfrac{1}{4}\left[\dfrac{\partial^2 R}{\partial u_1^2} + \dfrac{\partial^2 R}{\partial u_2^2}\right] = \dfrac{dkbc}{ma^2(a+c)} \quad h_{20} = \dfrac{1}{4}\left[\dfrac{\partial^2 R}{\partial u_1^2} - \dfrac{\partial^2 R}{\partial u_2^2} - 2i\dfrac{\partial^2 R}{\partial u_1 \partial u_2}\right] \tag{12}$$

And from the $\lambda_3 \omega_{11} = -h_{11}$; $(\lambda_3 - 2di)\omega_{20} = -h_{20}$, we get $\omega_{11} = \dfrac{dkbc}{ma^2(a+c)^2}$,

$$\omega_{20} = \frac{1}{(a+c)^2 + d^2}\left[\frac{dkb(2c^2 - a^2 - 2bc + ac)}{ma^2(2b-a-c)} + \frac{4dkb(a^2 - c^2 + 2bc)}{ma(a+c)(2b-a-c)}\right.$$
$$\left. +i\left(\frac{2kb(a^2 - c^2 + 2bc)}{ma(2b-a-c)} - \frac{4kcb^2(2c^2 - a^2 - 2bc + ac)}{ma(2b-a-c)(a+c)^2}\right)\right] \tag{13}$$

then $G_{101} = \frac{1}{2}\left[\frac{\partial^2 P}{\partial u_1 \partial u_2} - \frac{\partial^2 Q}{\partial u_2 \partial u_3} + i\left(\frac{\partial^2 Q}{\partial u_1 \partial u_3} + \frac{\partial^2 P}{\partial u_2 \partial u_3}\right)\right]$, $G_{110} = \frac{1}{2}\left[\frac{\partial^2 P}{\partial u_1 \partial u_2} + \frac{\partial^2 Q}{\partial u_2 \partial u_3} + i\left(\frac{\partial^2 Q}{\partial u_1 \partial u_3} - \frac{\partial^2 P}{\partial u_2 \partial u_3}\right)\right]$ (14)

so combining (5)-(14),we can get the value of $g_{21} = G_{21} + (2G_{110}\omega_{11} + G_{101}\omega_{20})$, and further we can get the value

of $C_1(0) = \frac{i}{2d}[g_{20}g_{11} - 2|g_{11}|^2 - \frac{1}{3}|g_{02}|^2] + \frac{g_{21}}{2}$ .Finally according to the following

expression $\mu_2 = -\frac{\mathrm{Re}\,C_1(0)}{\alpha'(0)}$; $\beta_2 = 2\,\mathrm{Re}\,C_1(0)$

$\tau_2 = -\frac{\mathrm{Im}\,C_1(0) + \mu_2\omega'(0)}{d}$, we have the following result.

Thereom 4 (a) if $\alpha'(0) > 0$, when $\mu_2 > 0$, the direction of bifurcation is $h > h_0$,

when $\mu_2 < 0$, the direction of bifurcation is $h < h_0$;(b)if $\alpha'(0) < 0$,we have the contrary result. if $\beta_2 < 0$, the bifurcation solution is asymptotically stable, if $\beta_2 > 0$, the bifurcation solution is not asymtotically stable.

3. Numerical stimulation

We have numerical analysis with $a = 10, b = 40, c = 2.5, l = 1, k = 2$ .we can get the bifurcation value is

$h_0 = \frac{26}{27}$ .Then we use Matlab to computer the solution figure as follows near the h_0 [see.Fig1]. Further, we get value

of $\mu_2 = 0.0237, \tau_2 = 0.0137$,

$\beta_2 = 0.0426$, $\alpha'(0) = -0.9004 < 0$. So the direction of bifurcation is $h > h_0$, and this solution is unstable. $g_{11} = 0.1306 + 1.2178i$, $g_{02} = -0.5184 - 0.1721i$; $g_{20} = -0.3960 + 1.4458i$,

$\omega_{11} = 0.0056$; $\omega_{20} = 0.0100 + 0.0146i$. Finally we can get the period,

T=0.4967+0.2871(h-0.9630)+O((h-0.9630)^2) , and the periodic solution has the following expression,

$$\begin{pmatrix} x \\ y \\ z \end{pmatrix} = \begin{pmatrix} 5.8095 \\ 5.8095 \\ 40 \end{pmatrix} + \begin{pmatrix} 1 & 0 & -1.8590 \\ 1 & -1.2649 & 0.4648 \\ 2.7541 & 2.1773 & 1 \end{pmatrix} \begin{pmatrix} u_1 \\ u_2 \\ u_3 \end{pmatrix}$$

Where $u_1 = \mathrm{Re}(W), u_2 = \mathrm{Im}(W), u_3 = 0.0056|W|^2 + \mathrm{Re}((0.0100 + 0.0146i)W^2)$

$W = 6.4957\sqrt{h - 0.9630}e^{2i(t+\varphi)\pi/T} + 0.5560(h - 0.9630)$.

$\times[(0.1721 - 0.5184i)e^{-4i(t+\varphi)\pi/T} + (4.3374 + 1.1880i)e^{4i(t+\varphi)\pi/T} - 7.3065 + 0.7838i]$

Using the matlab to give the following figure (see Fig 2).

References

Liu, chongxin, Liu Ling, Liu tao, Li Peng. (2006). A new butterfly-shaped attractor of Lorenz-like system chaos, soliton & Fractals, 28, 1196-1203.

Lü JH, Zhou TS, Chen G. (2002). Local Bifurcations of the Chen System. Int J Bifurcation Chaos, 12, 2257-2270.

Li TC, Chen G. (2004). On stability and bifurcation of chen's system. Chaos, Soliton & Fractals, 19, 1269-1282.

Lü JH, Chen G. (2002). Dynamical analysis of a new chaotic attractor. Int J Bifurcation Chaos,12, 1001-1015.

Changpin, Li, Guanrong, Chen. (2003). A note on Hopf bifurcation in chen's system. Int J Bifurcation Chaos, 6, 1609-1615.

LI, Jinbing, Feng, Beiye. (1995). *Stability, bifurcation and chaos*, Yunan science and technology pulishing house.
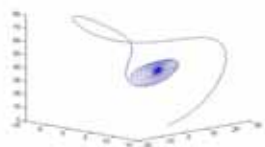

Figure1. bifurcaiton direction of bifurcating solution
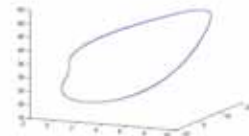
Figure 2. the bifurcating periodic solution

Analysis of Covariance in Researching on Influence of the Dormitory Academic Atmosphere on Achievement

Hefang Fan, Shunhou Fan, Chuiling Bai & Junli Liu

College of Science, Tianjin Polytechnic University, Tianjin 300160, China

E-mail: fanhefang2006@163.com

Abstract

The construction of the academic atmosphere is directly related to the quality of talents. The approaches of variance analysis and the covariance analysis method of mathematical statistics method are applied in this paper. And the relations of achievement and the academic atmosphere is quantitatively analyzed in terms of the data, which provides a basis of decision-making for university to enhance the academic atmosphere construction.

Keywords: The academic atmosphere, Achievement, Variance analysis, Covariance analysis

1. Introduction

The learning atmosphere is important for the students' grown - up .The academic atmosphere on the quality of talents can be reflected by student achievement. Dormitory is an important place where college students study and live. The construction of the dormitory style is an important facet of the construction of study style in university. We can often see a phenomenon that the student achievements in the same dormitory are all high or lower. So does the dormitory style have significant effect on student achievement? If have, what laws are the emergence and development of effect.

This paper takes 99 students of18 dormitories of 05 grade telecom special of tianjin polytechnic university as an example, taking student achievement in three academic years as the research object,

The data is provided by teaching section and it is veritable and exact.

Tianjin polytechnic university implements credit hour as academic assessment system. Credit hour of each student can be calculated according to the formula

$$y = \frac{\sum_{i=1}^{k} s_i c_i}{\sum_{i=1}^{k} s_i}$$

s_i represents the its curriculum credit ,c_i represents result of final examination of exon I curriculum. y is credit hour . s_i comes from teaching plan, c_i comes from teaching section .We can calculate credit hour of the first semester, the second term ,the second academic year and the third academic year.

2. Establishment of mathematical model

The analysis of various table 1 can indicate that the dormitory factor has no significant influence on college entrance examination achievement, that is to say ,the arrangement of dormitory is random.

In order to study the relations of scholastic achievement and the style of dormitory study, the style of dormitory that can be looked as a factor of influence on students' achievement denote A,m dormitory can be looked as m levels. dependent variable is the student credit hour .Where the credit hour of exon i dormitory exon j student denote by y_{ij} .Because not only the dormitory style study but also foundation differential have influence on credit hour ,covariance analysis model can be introduced. We denote college entrance examination achievement (based scores)of exon j student in exon i dormitory by z_{ij} as

covariate .let α_i to be effect of exon dormitory , μ is   the total effect of m dormitory, r is regression coefficient of covariance, the number student of exon dormitory is n_i ,covariance analysis model can be established as follows

$$\left[\begin{array}{l} y_{ij} = \mu + a_i + rz_{ij} + \varepsilon_{ij} \\ \sum_{i=1}^{m} n_i a_i = 0 \\ \varepsilon_{ij} \ \square\ N(0,\sigma^2), i=1,2,......m; j=1,2......n_i \end{array}\right.$$

we have now illustrated model parameters estimation and hypothesis testing of parameters.the detailed derivation he detailed derivation has been studied previously (Li,fang.Analysis of covariance in appraising teaching quality*)*,the result is

$$\left[\begin{array}{l} \hat{\mu} = \bar{y} - \hat{r}\bar{z} \\ \hat{\alpha}_i = (\bar{y}_{i.} - \bar{y}) - \hat{r}(\bar{z}_{i.} - \bar{z}) \ . \\ \hat{r} = \dfrac{L_{yzw}}{L_{zzw}} \end{array}\right.$$

where $\quad L_{yzw} = \sum_{i=1}^{m} \sum_{j=1}^{n_i} (y_{ij} - \bar{y}_{i.})(z_{ij} - \bar{z}_i), \quad L_{zzw} = \sum_{i=1}^{m} \sum_{j=1}^{n_i} (z_{ij} - \bar{z}_{i.})^2$

$\bar{y} = \dfrac{1}{n}\sum_{i=1}^{m}\sum_{j=1}^{n_i} y_{ij}, \quad \bar{z} = \dfrac{1}{n}\sum_{i=1}^{m}\sum_{j=1}^{n_i} z_{ij}, \quad \bar{y}_{i.} = \dfrac{1}{n_i}\sum_{j=1}^{n_i} y_{ij}, \quad \bar{z}_i = \dfrac{1}{n_i}\sum_{j=1}^{n_i} z_{ij},$

Whether m levels of factor A has significant differences can transform into problems of hypothesis testing of parameters

$H_0 : a_1 = a_2 = ... = a_r = 0$ against all alternative hypotheses.

the test statistic is

$$F = \frac{SSA / f_A}{SSE / f_E} = \frac{\left[(L_{yyT} - \dfrac{L_{yzT}^{\ 2}}{L_{zzT}}) - (L_{yyw} - \dfrac{L_{yzw}^{\ 2}}{L_{zzw}}) \right] / (m-1)}{(L_{yyw} - \dfrac{L_{yzw}^{\ 2}}{L_{zzw}}) / (n-m-2)}$$

When hypothesis H_0 is true

$$F \ \square\ F(m-1, n-m-2)$$

The rejection region under significant level α is

$$w = \{F > F_a(m-1, n-m-2)\}$$

to test significant of covariance ,that is to say ,to test hypothesis

$$H_{0r} : r = 0 \leftrightarrow H_{1r} : r \neq 0$$

the test statistic is

$$F = \frac{SS_r / f_r}{SSE / f_E} = \frac{\dfrac{L_{yzw}{}^2}{L_{zzw}}}{(L_{yyw} - \dfrac{L_{yzw}{}^2}{L_{ZZW}})/(n-m-2)}$$

When hypothesis H_{0r} is true

$$F \sim F(1, n-m-2)$$

he rejection region under significant level α is

$$w = \{F > F_a(1, n-m-2)\}$$

When we use higher mathematic 1s as dependent variable, an analysis of covariance table can be listed

The analysis of various table 2 could indicate that the achievement of higher mathematic 1 is no significant in different dormitory .College entrance examination achievement has significant influence on the achievement of higher mathematic 1.

When we use higher mathematic 2s as dependent variable, an analysis of covariance table can be listed.

The above analysis of various table 3could indicate that the achievement of higher mathematic 2 is significant in different dormitory .College entrance examination achievement has significant influence on the achievement of higher mathematic 2.

When we use credit hour of the first semester as dependent variable, an analysis of covariance table can be listed

The above analysis of various table 4 could indicate that credit hour of the first semester is no significant in different dormitory .College entrance examination achievement has significant influence on credit hour of the first semester

When we use credit hour of the second semester as dependent variable, an analysis of covariance table can be listed

The analysis of various table 5 could indicate that credit hour of the second semester is significant in different dormitory .college entrance examination achievement has significant influence on credit hour of the second semester

When we use credit hour of the second academic year as dependent variable, an analysis of covariance table can be listed

The analysis of various table 6 could indicate that credit hour of the second academic year is significant in different dormitory .college entrance examination achievement has significant influence on credit hour of the second academic year

When we use credit hour of the third academic year as dependent variable, an analysis of covariance table can be listed.

The analysis of various table 7 could indicate that credit hour of the third academic year is significant in different dormitory. College entrance examination achievement has significant influence on credit hour of the third academic

3. Result

From what has been discussion above, we can see that arrangement of dormitory is random when they entered college .dormitory factor has no significant influence on both single curriculum and credit hour at the first semester, the dormitory factor begin to have significant influence on both single curriculum and credit hour at the second semester. We can see that the situation has further developed in the second academic year and in the third academic from the value of p. Many reasons can be account for this phenomenon as follows .Students are not acquaint with each other at the first semester, with the passage of time, the students among the same dormitory influence on each other .The students in the same dormitory are often have the same fancies .We can seen that the dormitory style study have significant influence on student achievement. The construction of the dormitory style should manage as an important key of the construction of study style in university.

References

DeGracie, j. s. and Fuller, W. A. (1972). Estimation if the slope and analysis of covariance when the concomitant variable is measured with error. 67(1972), 930-937.

Li, fang. (2008). Analysis of covariance in appraising teaching quality. *Tianjin polytechnic university journal*. 2008, 27(2): 86-87.

Wang, Lingling. P*ractical statistical methods.*

Table 1.

Source	Type III Sum of Squares	df	mean Square	F	p
Corrected model	616.623(a)	17	36.272	.637	.853
Intercept	451657.232	1	451657.232	7926.193	.000
dormitory	616.623	17	36.272	.637	.853
Error	4615.613	81	56.983		
Total	461269.090	99			
Corrected Total	5232.235	98			

a R Squared = .118 (Adjusted R Squared = -.067)

Table 2.

Source	Type III Sum of Squares	df	mean Square	F	p
Corrected model	5914.370(a)	18	328.576	2.452	.003
Intercept	1032.105	1	1032.105	7.703	.007
dormitory	2984.856	17	175.580	1.310	.208
Based scores	2099.600	1	2099.600	15.670	.000
Error	10719.267	80	133.991		
Total	619886.000	99			
Corrected Total	16633.636	98			

a R Squared = .356 (Adjusted R Squared = .211)

Table 3.

Source	Type III Sum of Squares	df	mean Square	F	p
Corrected Model	11688.339(a)	18	649.352	2.579	.002
Intercept	122.921	1	122.921	.488	.487
dormitory	8375.332	17	492.667	1.957	.024
Based scores	2395.974	1	2395.974	9.517	.003
Error	20139.843	80	251.748		
Total	391114.000	99			
Corrected Total	31828.182	98			

a R Squared = .367 (Adjusted R Squared = .225)

Table 4.

Source	Type III Sum of Squares	df	mean Square	F	p
Corrected Model	2425.284(a)	18	134.738	3.934	.000
Intercept	2199.758	1	2199.758	64.232	.000
dormitory	1350.597	17	79.447	2.320	.006
Based scores	805.770	1	805.770	23.528	.000
Error	2739.780	80	34.247		
Total	571130.434	99			
Corrected Total	5165.064	98			

a R Squared = .470 (Adjusted R Squared = .350)

Table 5.

Source	Type III Sum of Squares	df	mean Square	F	p
Corrected model	9315.774(a)	18	517.543	3.883	.000
Intercept	386.532	1	386.532	2.900	.092
dormitory	5957.939	17	350.467	2.629	.002
Based scores	2112.926	1	2112.926	15.853	.000
Error	10662.626	80	133.283		
Total	448987.304	99			
Corrected Total	19978.400	98			

a R Squared = .466 (Adjusted R Squared = .346)

Table 6.

Source	Type III Sum of Squares	df	mean Square	F	p
Corrected Model	8062.818(a)	18	447.934	3.476	.000
Intercept	1146.524	1	1146.524	8.898	.004
dormitory	6608.093	17	388.711	3.017	.000
Based scores	1112.547	1	1112.547	8.634	.004
Error	10308.639	80	128.858		
Total	470840.262	99			
Corrected Total	18371.457	98			

a R Squared = .439 (Adjusted R Squared = .313)

Table 7.

Source	Type III Sum of Squares	df	Mean Square	F	p
Corrected model	11062.575(a)	18	614.587	3.233	.000
Intercept	479.880	1	479.880	2.524	.116
dormitory	9047.644	17	532.214	2.800	.001
Based scores	1704.355	1	1704.355	8.965	.004
Error	15208.775	80	190.110		
Total	424020.782	99			
Corrected Total	26271.350	98			

a R Squared = .421 (Adjusted R Squared = .291)

Call for Manuscripts

Modern Applied Science is a peer-reviewed journal, published by Canadian Center of Science and Education. The journal publishes research papers in the fields of chemistry, environmental sciences, management and economics, physics, mathematics and statistics, geology, engineering, computer and information sciences, and biology. The journal is published in both printed and online versions. The online version is free access and download.

We are seeking submissions for forthcoming issues. The paper should be written in professional English. The length of 3000-8000 words is preferred. All manuscripts should be prepared in MS-Word format, and submitted online, or sent to: mas@ccsenet.org

Paper Selection and Publication Process

a). Upon receipt of paper submission, the Editor sends an E-mail of confirmation to the corresponding author within 1-3 working days. If you fail to receive this confirmation, your submission/e-mail may be missed. Please contact the Editor in time for that.

b). Peer review. We use single-blind system for peer-review; the reviewers' identities remain anonymous to authors. The paper will be peer-reviewed by three experts; one is an editorial staff and the other two are external reviewers. The review process may take 2-3 weeks.

c). Notification of the result of review by E-mail.

d). The authors revise paper and pay publication fee.

e). After publication, the corresponding author will receive two copies of printed journals, free of charge.

f). E-journal in PDF is available on the journal's webpage, free of charge for download.

Requirements and Copyrights

Submission of an article implies that the work described has not been published previously (except in the form of an abstract or as part of a published lecture or academic thesis), that it is not under consideration for publication elsewhere, that its publication is approved by all authors and tacitly or explicitly by the responsible authorities where the work was carried out, and that, if accepted, it will not be published elsewhere in the same form, in English or in any other languages, without the written consent of the Publisher. The Editors reserve the right to edit or otherwise alter all contributions, but authors will receive proofs for approval before publication.

Copyrights for articles published in CCSE journals are retained by the authors, with first publication rights granted to the journal. The journal/publisher is not responsible for subsequent uses of the work. It is the author's responsibility to bring an infringement action if so desired by the author.

More Information

E-mail: mas@ccsenet.org

Website: www.ccsenet.org/mas

Paper Submission Guide: www.ccsenet.org/submission

Recruitment for Reviewers: www.ccsenet.org/reviewer.html

Modern Applied Science